

Surface passivation effects on metaloxide nanocomposites

Thesis Submitted to
UNIVERSITY OF CALICUT
in partial fulfillment of the requirements
for the award of the degree of

DOCTOR OF PHILOSOPHY
In
PHYSICS

Under the Faculty of Science

By

SHIJINA K

Supervisor:
Prof. (Dr) GEORGE VARGHESE
(Director, KSCSTE, Trivandrum)

DEPARTMENT OF PHYSICS
UNIVERSITY OF CALICUT
MALAPPURAM
KERALA 673635- INDIA

APRIL 2016

DEPARTMENT OF PHYSICS
UNIVERSITY OF CALICUT

Dr. GEORGE VARGHESE
Professor (Rtd)
Dept. of Physics, University of Calicut, Kerala.

17th October 2016

Certificate

Certified that the adjudicators are not suggested any corrections in the thesis
“Surface passivation effects on metaloxide nanocomposites” for the award of PhD
degree.



Dr. GEORGE VARGHESE
(Supervising Guide)
Ph: +91-9447227571, E-mail: gv@uoc.ac.in

DEPARTMENT OF PHYSICS
UNIVERSITY OF CALICUT

Dr. GEORGE VARGHESE
(Director, KSCSTE, Trivandrum)
Professor (Rtd)
Dept. of Physics, University of Calicut, Kerala.

28th April 2016

Certificate

Certified that Mrs. Shijina K has done her research studies under my supervision at the Department of Physics, University of Calicut on the problem "SURFACE PASSIVATION EFFECTS ON METALOXIDE NANOCOMPOSITES". She has successfully completed the studies and the present thesis is a genuine report on the summary of her work and the major findings resulted out of it. It is also certified that the thesis or a part of it has not been used elsewhere for the award of any degree.



Dr. GEORGE VARGHESE
(Supervising Guide)

Ph: +91-9447227571 E-mail: gv@uoc.ac.in

DEPARTMENT OF PHYSICS
UNIVERSITY OF CALICUT

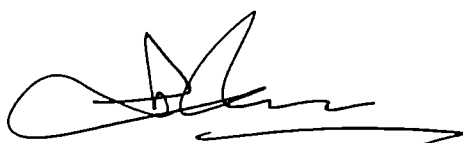
Dr. GEORGE VARGHESE
(Director, KSCSTE, Trivandrum)
Professor (Rtd)
Dept. of Physics, University of Calicut

28th April 2016

Certificate

Certified that the following articles, originated as the outcome of this research work, are published in the peer-reviewed international journals.

1. Shijina K, George Varghese, Megha U, J. Luminescence 175 (2016) 207.
2. K. Shijina, George Varghese, U. Megha, Mater. Sci. Engineer. B 199 (2015) 125.
3. Shijina K, George Varghese, Megha U, Mater. Sci. Semiconductor processing 34 (2015) 21.
4. Shijina K, Megha U, George Varghese, J. Luminescence 145 (2014) 219.
5. Shijina K, Megha U, George Varghese, SOP. Trans. Nanotechnology 1 (2014).



Dr. GEORGE VARGHESE
(Supervising Guide)

Declaration

Certified that the work presented in this thesis entitled “SURFACE PASSIVATION EFFECTS ON METALOXIDE NANOCOMPOSITES” is based on the original research work done by me under the supervision and guidance of Dr. GEORGE VARGHESE, Director, KSCSTE (Professor (Rtd.), Department of Physics, University of Calicut) and has not been included in any other thesis submitted previously for the award of any degree.

Calicut University
28th April 2016


Shijina K

Acknowledgement

I would like to express my overwhelming gratitude to my research guide, Dr. George Varghese, for his expertise shown in guiding my work and the willingness to share his knowledge and experience. He has given immense freedom for me in developing ideas and he is always willing to hear and acknowledge sincere efforts. His profound practical skills, immense knowledge and critical but valuable remarks led me to do a good research. I especially thank him for his prompt reading and careful critique of my thesis. Throughout my life I will benefit from the experience and knowledge I gained working with Dr. George Varghese. I express my sincere thanks to Dr. M. M. Musthafa, Head, Department of Physics and the former Head of the Department, Dr. Antony Joseph for permitting me to use the research facilities in the Department.

I would like to thank my doctoral committee members and all the other teachers in Department of Physics. I gratefully acknowledge the help and inspiration from Dr. N.K. Renuka, Department of Chemistry, who has inspired me in both academic and personal development. I express my sincere thanks to Prof. Santhakumari (retired Professor & Head from MES College, Valanchery) and Prof. Muhammad Musthafa K (retired Professor from EMEA College Kondotty) for their support during my PhD thesis correction. I am thankful to all the office and library staff of the Department of Physics for all the help and cooperation. I thank University of Calicut and University Grants Commission (UGC) for financially supporting me during this endeavour.

My time at Calicut University was made enjoyable in large part due to the many friends who have become a part of my life. It is my pleasure to acknowledge the advice and love received from my senior researchers. I feel wordless to appreciate the selfless support, love, care and ever encouraging words of my husband. I would like to thank all of my colleagues at the department of Physics especially Megha, Dhanya, Hajara and Salma and all other friends in CU campus for their great support during my Ph.D period. I record my deep and utmost gratitude to my Achan and Amma for their love and care during the entire period of my research work. I would like to thank my brothers for the love and care. Finally I thank all my well wishers and friends who have supported me in this venture. Above all, I thank God Almighty.

Shijina K.

Preface

Nanocomposite materials have emerged as a suitable alternatives to overcome the limitations of microcomposites, include the preparation challenges related to control the elemental composition. The use of inorganic nanoparticles instead of micrometer particles can provide high performance, novel materials for many industrial applications. As the dimensions of the materials reach in the nanometer level, interactions of phase interfaces become largely improved and this is the important thing to aggrandize the materials properties. Surface area to volume ratio of the reinforcement materials employed in the preparation of nanocomposites are decisive to understanding their structure-property relationships.

When the dimension of the nanocomposite comes into low dimension, it will exhibit excellent electronic, optical and thermal properties due to their large surface areas and possible quantum confinement effects. It is obvious that low nanostructures with well controlled dimensions and crystallography explored a new class of intriguing system for applications. The thermal stability of low dimensional nanostructure is of critical importance in nanoscale electronic and photonic devices. It is well documented that the melting point of a solid material will be greatly reduced when it is processed as nanostructures. Understanding the mechanical properties of nanostructures is essential for the atomic scale manipulation and modification of the materials. These materials behave qualitatively different when the dimensions are reduced from micro to nanoscale. Magnetic properties of low dimensional particles show a variety of unusual magnetic behaviour compared to bulk materials, mostly due to surface-interface effects, including symmetry breaking, electronic environment/charge transfer and magnetic interactions. As the critical dimension of an individual device becomes smaller and smaller, the electron-transport properties of their components becomes an important issue to study.

This research work mainly focused on the synthesis of one dimensional (1D) mesoporous nanocomposite like ZnNiO, Al:ZnNiO, Pd:ZnNiO, Cu:ZnNiO, Dy:ZnNiO and Ce:ZnNiO) through a soft template method and characterized them for using sophisticated techniques such as X-Ray Diffractometer(XRD), Field Emission Scanning Electron Microscopy (FESEM), Energy Dispersive Spectra(EDS), Surface

area analyzer, Diffuse reflectance spectra, Fluorescence spectra and Vibrating sample spectrometer (VSM). The aim of this thesis was to contribute to a deeper understanding of the surface modification effects on adsorption, magnetic and optical properties of ZnNiO, Al: ZnNiO, Cu: ZnNiO, Pd: ZnNiO, Dy: ZnNiO and Ce: ZnNiO nanocomposites for various applications.

In the introduction chapter, I discussed about the importance and review of mesoporous nanocomposites with one dimensional morphology. Second chapter comprises various synthesizing strategies for preparing mesoporous materials and the role of surfactant. The principle and mechanism of various sophisticated methods like X-ray diffractometer, Field Emission Scanning Electron Microscopy, Energy Dispersive Spectra, Diffuse Reflectance Spectra, Fluorescence Spectra and Vibrating Sample Magnetometer are discussed.

The results in the third chapter of the thesis were devoted to the study of crystal structure, morphology and composition of ZnNiO and polymer capped ZnNiO and their composites. Surface passivation effects on crystal structure of (ZnNiO Al:ZnNiO, Cu:ZnNiO, Pd:ZnNiO, Dy:ZnNiO and Ce:ZnNiO) nanocomposites reveal that this passivation by polyvinyl pyrrolidone does not damage the hexagonal structure of ZnNiO. Grain size calculated from X-ray diffraction studies showed that, size decreases when ZnNiO was capped with PVP and adjunction of other metals in ZnNiO lattice. Scanning Electron Microscopy (SEM) images of all the capped nanocomposites were confirmed the possibility of one dimensional growth of nanoparticles. The polymer, poly vinyl pyrrolidone can passivate the facets of ZnO and thereby adjust the growth velocity. Elemental composition spectra (EDS) of the nanocomposites confirmed the presence of constituent elements in appropriate proportions.

Fourth chapter describes the capping effects on BET surface area, pore size, external area and pore volume of the nanocomposites. These results gave us information that bandgap engineering would be possible through nanoporosity. Peculiar characteristics of large surface area and high porosity of mesoporous polymer capped ZnNiO and other five polymer capped nanocomposites may have great potential applications in electronics, catalysts and optoelectronic devices. The specific surface areas of the uncapped and capped samples were determined by

using a micrometrics ASAP 2020 surface area porosity analyzer. The calculated surface area of the capped samples are very high compared to uncapped samples and the N_2 adsorption isotherm hysteresis loop of the capped samples are matched to type IV H_3 hysteresis loop of mesoporosity. The pore size distribution of the samples were calculated from the data of the desorption branch of the isotherm using Barret-Joyner-Halenda (BJH) method. Microporosity of the samples is calculated from t-plot method. This result reveals that all the capped samples contain abundant mesoporous structured particles.

Effects of surface passivation on magnetic properties of nanocomposites are described in fifth chapter of the thesis. Observations show that ferromagnetism observed in semiconductors not only depends on the localized moments in magnetic ions but also due to the defect generated magnetic moments. Some researchers proposed that room temperature ferromagnetism can be associated with holes in the d shell arising due to the charge transfer from the Zn atom at the surface to the capping molecule. Room temperature ferromagnetism in all the PVP capped samples with high coercivity and magnetisation were observed. Uncapped ZnNiO showed paramagnetic behaviour with low retentivity.

Fifth chapter also included antibacterial activities of uncapped and capped metaloxide nanocomposites. Uncapped and capped metaloxide nanocomposites were explored as an antibacterial agent due to their non toxicity. In the research work, these composites were tested against *Pseudomonas aeruginosa* bacteria (Gram negative) using the disc diffusion method to determine their ability as an antibacterial agent. The zone inhibition formed around each disc confirmed that Dy:ZnNiO & Pd:ZnNiO have the maximum activity among various capped metaloxides and uncapped ZnNiO has maximum activity than capped ZnNiO due to oxygen vacancies.

In the sixth chapter, surface passivation effects on diffuse reflectance spectra, fluorescence spectra and fluorescence life time and defect band energy formed inside the optical bandgap of the nanocomposites were investigated. This simple modification method through polymer capping provides a chance for improving fluorescence emission with high life time. Surface passivation helps us to reach the main goal of the research work. Polyvinyl pyrrolidone capping improved

fluorescence ultraviolet emission with suppressed visible emission. Fluorescence lifetime of the capped samples is increased when compared to uncapped ZnNiO nanocomposites. Bandgap calculated from diffuse reflectance spectra showed that bandgap is reduced in case of capped samples compared to pure ZnO and increased compared to uncapped ZnNiO. This increase in bandgap may be due to the quantum confinement effect in small size of the capped samples.

Seventh chapter comprises summary of all the properties and concluded that these capped nanocomposites (ZnNiO, Al:ZnNiO, Cu:ZnNiO, Pd:ZnNiO, Dy:ZnNiO and Ce:ZnNiO) are good materials for various applications especially in UV/Blue emitters and in transformer core applications. Due to its mesoporosity and non-toxicity it is focussing on the applications on drug delivery systems. This one dimensional, mesoporous, ferromagnetic and enhanced UV emitting properties of the nanocomposites confirmed that surface passivation by polyvinyl pyrrolidone in metaloxide nanocomposites is a good procedure for increasing almost all the important physical properties of the material.

Contents

1. Chapter 1: One dimensional mesoporous nanocomposites.....	1
1.1 Introduction.....	1
1.1.1 Ceramic matrix nanocomposites.....	2
1.1.2 Metal matrix nanocomposites.....	2
1.1.3 Polymer matrix nanocomposites	2
1.1.4 Zero dimensional(0D).....	3
1.1.5 One dimensional (1D).....	4
1.1.6 Two dimensional (2D).....	5
1.1.7 Density of states.....	5
1.2 Properties of nanomaterials.....	7
1.2.1 Thermal stability.....	7
1.2.2 Mechanical properties.....	7
1.2.3 Magnetic properties.....	8
1.2.4 Electron transport properties.....	8
1.2.5 Phonon transport properties.....	9
1.3 Porous materials.....	9
1.3.1 Microporous materials.....	10
1.3.2 Macroporous materials.....	10
1.3.3 Mesoporous materials.....	10
1.4 Applications of mesoporous materials.....	11
1.4.1 Cancer diagnosis and therapy.....	11
1.4.2 Optical sensors.....	11
1.4.3 Electrochemical sensors.....	12
1.5 ZnO nanostructures.....	12
1.5.1 Luminescence mechanism.....	12
1.5.1.1 Low temperature photoluminescence (LTPL).....	12
1.5.1.2 Room temperature photoluminescence (RTPL).....	13
1.5.1.3 Time resolved photoluminescence (TRPL).....	13
1.5.2 Electronic properties.....	14
• Native defects in ZnO.....	14
• Defect concentrations and formation energies.....	14
• Defect transition levels.....	15

• Migration barriers and diffusion activation energies.....	15
• Oxygen vacancies and zinc vacancies.....	16
• Zinc interstitials.....	16
• Zinc antisites, oxygen interstitials, oxygen antisites.....	16
1.6 Applications of ZnO nanostructures.....	16
1.6.1 Sensors.....	17
1.6.2 Photovoltaic cells.....	17
1.7 Motivation of the Research work.....	18
References.....	20
2. Chapter 2: Synthesizing strategies and characterization tools	24
2.1 Introduction.....	24
2.2 Mesoporous synthesizing strategies	25
2.2.1 Soft template method.....	25
2.2.2 Hard template method.....	26
2.3 Roll of capping agents.....	26
2.3.1 Exploitation of polyvinyl pyrrolidone (PVP-30K).....	27
2.4 Zinc Nickel Oxide (ZnNiO).....	27
2.4.1 Synthesis of ZnNiO based mesoporous nanocomposites.....	28
2.5 Characterisation techniques.....	29
2.5.1 X-ray diffractometer.....	29
2.5.2 FESEM Analysis.....	30
2.5.3 EDS Analysis.....	30
2.5.4 Vibrating Sample Magnetometer (VSM).....	30
2.5.5 Diffused reflectance spectroscopy (DRS).....	31
2.5.6 Fluorescence spectroscopy (FL).....	32
2.5.7 Surface area analyzer (Adsorption measurements).....	33
• Physisorption	33
• Chemisorption.....	34
• BET model.....	34
• Procedure.....	35
References.....	37

3. Chapter 3: Capping effects on structure and morphology.....	39
3.1 Introduction.....	39
3.2 Structural Analysis.....	40
3.2.1 XRD patterns of ZnNiO and ZnNiO/PVP nanocomposites.....	40
3.2.2 XRD patterns of Al:ZnNiO, Pd:ZnNiO & Cu:ZnNiO nanocomposites.....	42
3.2.3 XRD patterns of Dy:ZnNiO and Ce:ZnNiO nanocomposites.....	43
3.3 Calculation of nearest neighbour distances.....	44
3.4 FESEM analysis and EDS spectra.....	46
3.5 Conclusion.....	52
References.....	53
4. Chapter 4: Surface passivation effects on adsorption properties	54
4.1 Introduction.....	54
4.2 BET Isotherm.....	55
4.3 Specific surface area determination.....	60
4.4 Determination of total pore volume and average pore radius.....	62
4.5 Pore size distribution (PSD).....	63
4.5.1 t-plot.....	63
4.6 Conclusion.....	68
References.....	69
5. Chapter 5: Capping effects on magnetic properties.....	70
5.1 Introduction.....	70
5.2 Results and Discussion.....	71
5.3 Antibacterial studies.....	76
• Preparation of bacterial cultures.....	76
• Antibacterial activities nanocomposites against <i>Pseudomonas</i> bacteria.....	77
5.4 Conclusion.....	79
References.....	81
6. Chapter 6: Effects of capping agents on optical properties.....	83
6.1 Introduction.....	83
6.2 Diffuse reflectance spectra (DRS).....	84

6.2.1	Particle size determination.....	87
6.2.2	Bandgap determination.....	87
6.2.3	Urbach energy determination.....	90
6.3	Fluorescence spectra.....	94
6.3.1	Fluorescence lifetime.....	100
6.4	Correlation between particle size and bandgap energy.....	102
	• Brus equation.....	104
6.5	Conclusion.....	106
	References.....	108
7.	Conclusions and Future work.....	110
7.1	Conclusions.....	110
7.2	Future work.....	113

❖ **Publications**

Chapter 1

One dimensional mesoporous nanocomposites

1.1 Introduction

In the field of nanotechnology, composite materials became quite popular and pragmatic with a tremendous lust. Composites are materials with two or more constituent materials, which exhibit positive characteristics of both the components. Of late nanocomposites have been making a large splash in the media and throughout several industries. In the last few years, there has been a lot of interest to tailor the structure and composition of materials on nanometer scale. Therefore a systematic review on the preparation, properties and applications of nanocomposites are extremely important.

Nanocomposites are composites in which at least one of the dimensions of the phase should be in the nanometer range (1-100 nm). These materials have emerged as suitable alternatives to overcome the limitations of microcomposites, including the preparation challenges related to the control of elemental composition. The use of inorganic nanoparticles instead of micrometer particles can provide high performance, novel materials for many industrial applications. As the dimensions of

the materials reach the nanometer level, interactions of phase interfaces become largely improved and this is important in aggrandizing the material properties. Surface area volume ratio of the reinforcement materials employed in the preparation of nanocomposites are decisive in understanding their structure-property relationships. Further, the discovery of carbon nanotubes (CNTs) in 1991, added a new and fascinating dimension to the area of nanocomposites due to their admirable mechanical, thermal and electrical properties. The possibility of transforming CNTs into composite products paved way for the applications of CNT-containing materials.

Nowadays, nanocomposites offer environmentally benign technology and business opportunities for all sectors of industry. According to their matrix materials, nanocomposites are classified into three different categories.

1. Ceramic matrix nanocomposites
2. Metal matrix nanocomposites
3. Polymer matrix nanocomposites

1.1.1 Ceramic matrix nanocomposites

Ceramic matrix nanocomposites consist of ceramic fibres embedded in a ceramic matrix, thus forming a ceramic fibre reinforced ceramic materials. Consequently, incorporation of highly strengthened nanofibres into ceramic matrices has allowed the preparation of nanocomposites with excellent properties.

1.1.2 Metal matrix nanocomposites

Metal matrix nanocomposites consist of a ductile metal or alloy matrix in which some nanosized reinforcement material is implanted in the alloy matrix. These nanocomposite combine metal and ceramic properties and shows an extraordinary potential applications in many areas, such as aerospace and automotive industries.

1.1.3 Polymer matrix nanocomposites

Polymer matrix nanocomposites consist of nanosized inorganic fillers embedded in the polymer matrix. In materials research, the development of polymer nanocomposites is rapidly emerging as a multidisciplinary research activity whose

results could broaden the applications of polymers to the great benefit of many industries. Catalytic, electronic, optic and magnetic properties of the inorganic nanoparticles overlap to show a dramatic increase in the properties.

The integration of inorganic nanoparticles into the polymer matrix allows enhanced and thus advanced new functions by the combination of excellent properties of nanoparticles such as superparamagnetism, size dependent bandgap, electron-phonon transport etc., with processibility and thin film forming capability polymer. Polymers are already widely used in optoelectronic industry. The most prominent difference of such nanocomposites compared with their traditional counterparts is the small size of the filler particles which could bring added specific effects.

Depending on the dimension, nanocomposites are classified into,

1. Zero dimensional (0D)
2. One dimensional (1D)
3. Two dimensional (2D)



Figure 1.1: Schematic diagram of nanostructures (0D, 1D, 2D and 3D)

1.1.4 Zero dimensional (0D)

Zero dimensional materials are also known as quantum dots. Quantum dots are semiconductor nanoparticle, whose excitons are confined in all three spatial dimensions. It is essentially a tiny zero-dimensional semiconductor crystal with size in the order of nanometers. Generally, bandgap energy is increased while decreasing the size of the particle. If the energy difference between the highest valence band and the lowest conduction band, more energy is needed to excite the dot and the

crystal returns to its ground state. The main advantage of quantum dots is the ability to tune the size of the dots for many applications. For instance, size of the quantum dot is quite large compared to the small dots the spectrum shift towards red wavelength side and exhibit less pronounced quantum properties. The electrons in a quantum dot represent a zero-dimensional electron gas (0DEG). Here, total energy of the electron is the sum of allowed energies associated with the motion of these carriers along all three directions (say x, y, z directions). The total energy of the electron is given by

$$E_{Total} = \frac{\hbar^2}{2m} \left[\frac{n_x \pi}{L_x} \right]^2 + \frac{\hbar^2}{2m} \left[\frac{n_y \pi}{L_y} \right]^2 + \frac{\hbar^2}{2m} \left[\frac{n_z \pi}{L_z} \right]^2 \quad (1.1)$$

Where n_y, n_z are integers and L_x, L_y and L_z are confined sizes of the materials along x, y and z directions.

1.1.5 One dimensional (1D)

1D structure usually called quantum wires, although other systems such as rods, belts, and tubes are also fall within this category. Quantum wires represent two-dimensional confinement of electrons and holes. Such confinement permits free-electron behaviour in only one direction along the length of the wire. For this reason, the system of quantum wires describes a one-dimensional electron gas (1DEG), when electrons are present in the conduction band. The category of one-dimensional nanostructures consists of a wide variety of morphologies. These include whiskers, nanowires, nanorods, fibers, nanotubules, nanocables and nanotubes. Here, total energy of the electron is the sum of allowed energies associated with the motion of these carriers along two directions and the kinetic energy due to free motion of carriers in the other direction.

Here, total energy of the electron is

$$E_{Total} = \frac{\hbar^2}{2m} \left[\frac{n_y \pi}{L_y} \right]^2 + \frac{\hbar^2}{2m} \left[\frac{n_z \pi}{L_z} \right]^2 + \frac{\hbar^2 k_x^2}{2m} \quad (1.2)$$

Where n_y, n_z are integers and L_y, L_z are confined sizes of the materials along y and z directions.

1.1.6 Two dimensional (2D)

In a 2D structure, particles are confined to a thin sheet of thickness L_z along the z axis by infinite potential barriers that create a quantum well. A particle cannot escape from the quantum well $0 \leq z \leq L_z$ and loses no energy on colliding with its walls $z=0$ and $z=L_z$. In real systems, this confinement is due to electrostatic potentials, the presence of interfaces between different materials, the presence of surfaces, or a combination of these agents. Motion of the particle in the other two directions (i.e., in the xy plane) inside the quantum well is free. It is generally accepted that quantum confinement of electrons by the potential wells of nanometer-sized structures provides one of the most powerful and versatile means to control the electrical, optical, magnetic, and thermoelectric properties of solid state functional materials. Total energy of the electron is the sum of allowed energies associated with the motion of these carriers along one direction (say z direction) and the kinetic energy due to free motion of carriers in other two directions (say x and y directions)

$$E_{Total} = \frac{\hbar^2}{2m} \left(\frac{n_z \pi}{L_z} \right)^2 + \frac{\hbar^2}{2m} (k_x^2 + k_y^2) \quad (1.3)$$

1.1.7 Density of States

The density of states is defined as the number of energy states present in a unit energy interval per unit volume. Due to the quantization of energy levels, the relationship between the density of states and energy values is also dramatically modified as shown in figure 1.2. The density of states of bulk semiconductor is given by

$$g(E)_{3D} dE = \frac{1}{2\pi^2} \left(\frac{2m}{\hbar^2} \right)^{\frac{3}{2}} E^{\frac{1}{2}} dE \quad (1.4)$$

Density of states is proportional to $E^{\frac{1}{2}}$ for a bulk material and in a 2D material; there is only one restricted energy level. With this restriction in k-space, density of states in 2D is given by

$$g(E)_{2D} dE = \left(\frac{2m}{\hbar^2}\right)^{\frac{1}{2}} \left(\frac{2m}{\hbar^2}\right)^{-\frac{1}{2}} \frac{m}{\pi\hbar^2} dE \quad (1.5)$$

It is significant that, the 2D density of states does not depend on energy. Immediately as the top of the energy gap is reached, there is a significant number of available states. In 1D, two of the k-component are fixed, therefore the density of states per unit volume at energy E is given by

$$g(E)_{1D} dE = \frac{1}{\pi} \left(\frac{m}{\hbar^2}\right)^{\frac{1}{2}} E^{-\frac{1}{2}} dE \quad (1.6)$$

Density of states for 1D material is proportional to $E^{-\frac{1}{2}}$. In zero dimensional structures, the values of k are quantized in all directions. All the available states exist only at discrete energies described and can be represented by a delta function.

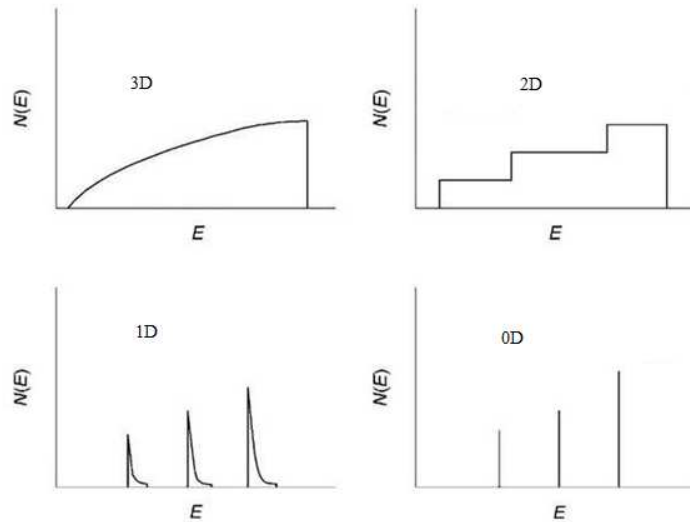


Fig 1.2: Schematic diagram of 3D, 2D, 1D, 0D density of states

1.2 Properties of nanomaterials

Compared with three dimensional materials, low dimensional nanoscale materials exhibit excellent electronic, optical and thermal properties due to their large surface areas and possible quantum confinement effects. It is obvious that low nanostructures with well controlled dimensions, and crystallography explored a new class of intriguing system for applications.

1.2.1 Thermal stability

The thermal stability of low dimensional nanostructure is of critical importance in nanoscale electronic and photonic devices. It is well documented that the melting point of a solid material will be greatly reduced when it is processed as nanostructures [6]. The remarkable reduction in melting point associated with a nanowire has several important implications. The annealing temperature is necessary for the synthesis of defect-free nanowires. Reduction in melting point enables one to cut, interconnect, and weld nanowires at relatively mild temperature. This capability of the material may provide a new tool to integrate these 1D nanostructures into functional device and circuitry. The thickness of nanowire is reduced to a smaller and smaller length scale, their stabilities may become extremely sensitive to environmental changes such as temperature and residual stress variation.

1.2.2 Mechanical properties

Understanding the mechanical properties of nanostructures is essential for the atomic scale manipulation and modification of the materials. These materials behave qualitatively different when the dimensions are reduced from micro to nanoscale. According to Hall-petch effect, hardness and yield stress of a polycrystalline material typically increases with decreasing grain size on the micrometer scale [7-8]. When the crystal planes in individual grains are sheared, piling up of dislocations at the grain boundaries occurs. As the grains are downsized, the area of their boundaries increases and thereby makes the material tougher by blocking dislocations. On the nanometre scale, an opposite behaviour was discovered by Schiotz and co-workers in computational simulations. Samples of nanocrystalline copper and palladium became softer with decreasing the grain size [9]. This

abnormal behaviour was believed to mainly arise from sliding motions at grain boundaries. As a result, the strength of a polycrystalline material first increases and then decreases with decreasing grain size and there exists a characteristic length for each solid material to achieve the toughest material. As for the single crystalline 1D nanostructure, they are supposed to be significantly stronger than their counterparts that have larger dimensions. This property can be attributed to a reduction in the number of defects per unit length.

1.2.3 Magnetic properties

Magnetic nanoparticles show a variety of unusual magnetic behaviour compared to bulk materials, mostly due to surface/interface effects, including symmetry breaking, electronic environment/charge transfer, and magnetic interactions. Soft magnetic nanocrystalline alloys have high coercivity and low remanence magnetization. Two important factors to improve the remanent magnetization are the nanocrystalline grain size and the degree of coherence across interphase boundaries. Soft magnetic materials can be used for data storage applications that are dependent on the microstructure and geometry of the material. Magnetic films are used in a variety of applications, including recording media and heads, magneto-optical storage, and sensors. The behaviour of the magnetic domains and single domain particles, magneto resistance, and magnetic anisotropy of the films are influenced by factors that include the grain size and orientation, the presence of the non-magnetic phases at grain boundaries, non-magnetic interlayers and magnetostriction. Nanoscale two-phase mixtures of hard and soft magnetic phases can exhibit values of remanent magnetization, M_r , significantly greater than the isotropic value of $0.5M_s$. This “remanence enhancement” is associated with exchange coupling between the hard and soft phases, which forces the magnetization vector of the soft phase to be rotated to that of the hard phase.

1.2.4 Electron transport properties

Miniaturization in electronics through improvements in top-down fabrication techniques approaching the point, where fundamental issues are expected to limit the dramatic increases in computing speed. As a result, CNTs and nanowires have recently been explored as building blocks to fabricate nanoscale electronic devices

through bottom-up approach. It is believed that, the bottom up approach to nanoelectronics has the potential to go beyond the limits of traditional top-down techniques. As the critical dimension of an individual device becomes smaller and smaller, the electron-transport properties of their components becomes an important issue to study. Studies from a number of groups indicated that some metal nanowires might undergo a transition to become semiconducting as their diameters are reduced below certain values [10]. The external conduction sub-band and valence sub-band of this system moved in opposite directions to open up a bandgap. Gold represents a metal whose transport properties have been extensively studied in the form of nanowires as thin as a single, linear chain of atoms [11]. Because these wires are extremely short in length, their conductance has been shown to be in the ballistic regime with the transverse momentum of electrons becoming discrete.

1.2.5 Phonon transport properties

In contrast to the extensive studies on electron transport in low dimensional nanostructures, investigation of phonon transport was not reported until very recently. Thermal conductivity of the material will be reduced due to scattering by boundaries when the dimension of a nanostructure is reduced to the range of phonon mean free path. Theoretical studies suggested that, diameter of a silicon nanowire becomes smaller than 20 nm, as a result of phonon confinement. The phonon dispersion relation might be modified such that the phonon group velocities would be significantly less than the bulk value [12-13]. Molecular dynamics simulation also showed that thermal conductivities of Si nanowires could be smaller than that of bulk silicon [14]. The reduced thermal conductivity is desirable in applications such as thermoelectric cooling and power generation, but it is not preferable for other applications such as electronics and photonics.

1.3 Porous materials

Porous material is a continuous and solid network material filled through voids. Porous solids are of scientific and technological interest because of their ability to interact with atoms, ions and molecules not only at their surfaces but throughout the

material. Depending on the pore size it is classified into three types (i) microporous (< 2 nm), (ii) mesoporous (2- 50 nm) and (iii) macroporous (> 50 nm) materials.

1.3.1 Microporous materials

Microporous material is a material containing pores width diameters less than 2 nm. Over the past decades crystalline microporous materials have continued to find new applications in their traditional areas of use such as catalysis and ion exchange. eg: zeolites

1.3.2 Macroporous materials

Materials with pore size greater than 50 nm are referred to as macroporous materials. They are generally prepared by coagulation, internal gelatination etc. Example of macroporous materials are rubber, paint etc.

1.3.2 Mesoporous materials

Mesoporous materials are defined as the materials with pore sizes between 2 and 50 nm [15]. Mesoporous structures are a wide class of materials including silica [16], metal oxides [17-24], metal hydroxides [25], carbon structures [26], hybrid materials [27], organic structures [28-29] and others [30]. The detailed classifications of the mesoporous materials are presented in Fig: 1.3.

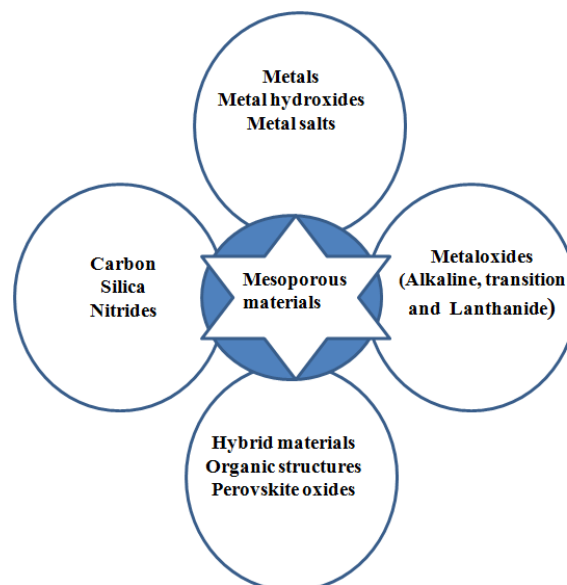


Figure 1.3: Chemical classifications of mesoporous materials

Mesoporous materials are highly attractive for a variety of applications in catalysis, electronics, photocatalytic hydrogen production, solar cells and battery components. Depending on the chemical nature, these structures might possess fluorescent, magnetic and optical properties. Nowadays extensive research has been carried out in biomedical applications due to their unique properties such as tunable pore size, chemical stability and possibility of surface modification [31].

1.4 Applications of mesoporous materials

Mesoporous materials have wide applications in cancer diagnosis and therapy, Electrochemical sensors, Fluorescence imaging, Optical sensors, Theranostics, Tissue engineering and also in magnetic resonance imaging.

1.4.1 Cancer diagnosis and therapy

Mesoporous materials are one of the most attractive tools for the anticancer treatment. These materials are used as anticancer drug vehicles, may enhance the cytotoxicity of chemotherapeutic agent [32] and can target to malignant tissues [33]. Moreover these mesoporous supports may prevent the premature drug release and its decomposition before it reaches the target site [34]. Intriguingly the unique physicochemical properties of mesoporous materials of the possibility to merge different theranostic functions into a single nanodevice for combined therapy and diagnosis [35].

1.4.2 Optical sensors

Optical sensing of target analyses includes the system based on naked eye or fluorescence detection relying on the colour change or quenching of fluorescence emission [36]. UV/Vis diffuse reflectance spectroscopy is used for the detection of calorimetric signal. Most of the optical sensor's composed of mesoporous materials for the detections of metal ion.

1.4.3 Electrochemical sensors

Electrochemical sensors are reliable, direct and reproducible analyses. These sensors are mainly used for organic compound detection. The application of electronically conductive ordered mesoporous carbon as the electrode component facilitates the charge transfer for electrochemical sensing application.

1.5 Zinc Oxide (ZnO) nanostructures

ZnO is a widely studied metaloxide nanomaterial, which has exhibited mesoporosity while forming composites with other metals. ZnO has received much attention over the past few years due to the excellent properties such as high transparency, photoluminescence, piezoelectricity, wide bandgap semiconductor, room temperature ferromagnetism and sensing effects. ZnO is a direct bandgap material with large exciton binding energy (60 meV). Intense research by many researchers has focused on novel nanostructures with different shapes. The different morphologies are due to the relative growth rates of the crystal facets during the synthesis. This makes it interesting material based on exciton recombination at room temperature or even higher. The structure, morphology and properties of ZnO based compounds are interesting subjects for research.

1.5.1 Luminescence mechanism

The quality of nanostructures as well as the ultraviolet and visible emission in the UV-Visible region was examined through low temperature photoluminescence, Room temperature photoluminescence and time resolved photoluminescence mechanisms.

1.5.1.1 Low temperature photoluminescence (LTPL)

Low temperature photoluminescence (LTPL) is a useful tool to examine the quality of nanostructures, after considering the fact that room temperature photoluminescence (RTPL) spectra may exhibit only ultraviolet emission even in the presence of considerable defect density in ZnO nanostructures [37-38]. Observation of a free exciton emission in LTPL spectra was used as a criterion of determining high optical quality of ZnO nanostructures [39-40]. Also, biexcitons are sometimes

observed in the low temperature PL spectra from ZnO nanostructures, which can be considered as another indication of the sample quality [41].

1.5.1.2 Room temperature photoluminescence (RTPL)

Generally room temperature photoluminescence spectra of ZnO shows emission bands in ultraviolet region and visible region but there are one or more emission bands in the visible region [42]. It should be noted that, most of the room temperature photoluminescence studies of ZnO focuses on the origin of defect related visible emission [43-44]. Position of near band edge emission at room temperature can vary significantly due to variations in relative contributions of free exciton emission, which is different for different growth techniques. Green emission in the visible region is the most commonly observed and the most controversial emission in ZnO [45]. Many different hypotheses have been reported to explain the green emission, but there is still no consensus. It should also be noted that the peak position of “green” emission is different from other reports [46]. Common observation for green emission is that, it appears to be related to the surface. Generally surface contains a large number of defects.

In addition to the origin of visible emission bands, the ratio of UV-to-visible emission is used as an indication of sample quality. The ratio of UV-to-visible emission in ZnO nanorods can be altered by embedding the nanorods in a polymer, and the magnitude of the observed increase in the UV-to-visible emission ratio depended on the type of polymer used [47]. The reduction in the visible defect emission was attributed to the reduction of surface traps due to charge transfer at ZnO/polymer interface. Finally, in addition to surface passivation by different materials, the ratio of UV-to-green emission can also be changed [48].

1.5.1.3 Time resolved photoluminescence (TRPL)

Time resolved photoluminescence spectra of various nanostructured ZnO by different methods can be investigated. Time resolved photoluminescence spectra of the hydrothermally synthesized ZnO nanorods shows short spontaneous emission times [49]. In size-dependent TRPL spectra of ZnO nanorods, found that the decay time increases as the rod size increases, which was attributed to the decrease in radiative rate of exciton–polaritons [50]. ZnO nanostructures typically exhibit higher

non-radiative defect density and shorter photoluminescence lifetimes compared to single crystals and high quality thin films.

1.5.2 Electronic properties

There has been a debate concerning the origin of its n-type conductivity in ZnO. Experimentally and theoretically, researchers studied self-compensation phenomenon and the nature of native donors. For both experiments and theory, contradictory results have been reported. It has been predicted that due to the low formation energies, point defects are expected in ZnO [51]. Theoretical studies have predicted that acceptor type defects in ZnO have high formation energy, while the native donors have either high formation energy [52]. Oxygen interstitial represents another candidate for acceptor defect in ZnO [53].

Native defects in ZnO

Native or intrinsic defects are imperfections in the crystal lattice, include missing of atoms at regular lattice positions (vacancies), extra atoms occupying in the interstices of the lattice (interstitials) and a Zn atom occupying an O lattice site or vice versa (antisites). Native defects are strongly influence the optical properties of the semiconductor, it affects minority carrier lifetime, luminescence efficiency, diffusion mechanisms connected to growth and device degradation [54-56]. But behaviour of point defects in ZnO is essential to its successful applications in semiconductor devices. Native defects are related to the compensation of the predominant acceptor or donor doping material.

Defect concentrations and formation energies

Under thermodynamic equilibrium and neglecting defect-defect interaction, concentration of the intrinsic defect in a solid material is determined from the formation energy E^f through the relation [57].

$$c = N_{sites} \exp\left(\frac{-E^f}{k_B T}\right) \quad (1.31)$$

Where N_{sites} is the number of sites per unit volume the defects can be incorporated on. k_B is the Boltzmann constant and T be the temperature. The above equation

shows that defects with high formation energies will occur in low concentrations. The formation energy of a defect and its concentration can be computed from first principles without resorting to experimental data.

Defect transition levels

Defect introduces an energy level in the bandgap of the semiconductors when defects are electrically active. Which involve transitions from different charge states of the defect [58-60]. These transition levels are directly derived from the calculated from the calculated formation energies. The transition level $\varepsilon\left(\frac{q}{q'}\right)$ is defined as the Fermi level position for which the formation energies of charge state q and q' are equal.

$$\varepsilon\left(\frac{q}{q'}\right) = \left[E^f(D^q; E_F = 0) - E^f(D^{q'}; E_F = 0) \right] / (q' - q) \quad (1.32)$$

Where $E^f(D^q; E_F = 0)$ is the formation energy of the defect D in the charge state q fermi level is at the valence band maximum $E_F = 0$

Migration barriers and diffusion activation energies

In addition to knowing their formation energies and defect transition levels it is important to know how native point defects migrate in the lattice. Migration of point defects greatly contributes to their incorporation during growth. Information about migration of point defects in ZnO is limited. Activation energy for impurity diffusion is the sum of the formation energy of the defect that mediates the diffusion process and migration barrier [61].

$$Q = E^f + E_b \quad (1.33)$$

E_b is the migration energy barrier, given by the energy difference between the equilibrium configurations at the saddle point along the migration path. The defect formation energy (E^f) strongly depends on the experimental conditions such as the position of Fermi level and the chemical potential of Zn and O (in the case of ZnO).

Oxygen vacancies and zinc vacancies

The oxygen vacancy is the most mentioned defect in the ZnO nanoparticle. This oxygen vacancy is responsible for the source of unintentional n-type conductivity and visible emission. Oxygen vacancy has the lowest formation energy. Using a simple model within the molecular orbital theory, we understood about the electronic structure of Zn in ZnO. The removal of Zn atom from the ZnO lattice results four O dangling bonds and six electrons. These four O dangling bonds combined into doubly occupied symmetric a_1 state in the valence band and three degenerate states in the bandgap, which is close to the valence band maximum. Zinc vacancies have very high formation energies in p-type ZnO lattice.

Zinc interstitials

A zinc interstitial atom (Zn_i) occupies the tetrahedral site or the octahedral site in the wurtzite structure of ZnO. At the octahedral site, this interstitial atom has one zinc atom and one O atom as nearest neighbour but in octahedral site it has three Zn and three O nearest neighbour atoms. Based on size consideration Zn interstitial is more stable at octahedral site.

Zinc antisites, oxygen interstitials and oxygen antisites

The other native point defects such as zinc antisites, oxygen interstitials and oxygen antisites have higher formation energies. The ZnO antisite is a double donor in n-type but its higher formation energy indicates that it is a source of n-type conductivity. The oxygen interstitial (O_i) occupy octahedral or tetrahedral interstitial site or form split interstitials. Oxygen antisite (O_{zn}) is an acceptor defect with very high formation energy.

1.6 Applications of ZnO nanostructures

ZnO is an attractive material for applications in electronics, photonics, acoustics, sensing and magnetic devices. Its high exciton binding energy (60 meV) gives a high edge over other semiconductors. Among the applications of ZnO, their importances in acoustic wave devices are due to large electromechanical coupling.

ZnO nanowires/nanorods are used in biosensors and gas sensors and solar cells, since it is relatively easy to produce which have good charge carrier transport properties and high crystalline quality. ZnO has been successfully used in thin film piezoelectric devices such as bulk acoustic wave and SAW resonators, filters, sensors and micro electromechanical systems (MEMS) due to its high electromechanical coupling coefficients. Among these, SAW filter is the most commonly used application, which has been an important component in mass consumer items such as TV filters and wireless communication systems.

1.6.1 Sensors

ZnO nanorod/nanowire FET sensors may create opportunities for highly sensitive and selective real time detection of various gases. The principle of gas sensor operation depends on the nature of gas molecules. There is an interest in the development of light weight gas sensors with parts per million range sensitivity and extended operation at low power levels. Previous reports on ZnO nanostructures demonstrates that ZnO with large surface area have potential for detecting NO₂, NH₃, CO, H₂, C₂H₅OH. ZnO nanorod is the promising candidate for detecting extremely low concentrations of H₂S. ZnO nanostructures have been explored as a biosensor for detecting biological molecules. One dimensional ZnO nanostructures are used as biosensor in the embryonic stage [62]. The advantages of ZnO biosensor are stability in air, nontoxicity, chemical stability and electrochemical activity. Sensing properties of ZnO nanostructures is governed by the oxygen vacancies o the surface.

1.6.2 Photovoltaic cells

Zinc oxide (ZnO) is an especially important material for applications in low cost photovoltaics such as dye-sensitized solar cells [DSSC] and hybrid polymer-inorganic nanostructured solar cells. Commonly titanium oxide (TiO₂) is used as a dye sensitized solar cell material but high electron mobility of ZnO itself made a candidate instead of TiO₂ in DSSCs [63-64]. DSSCs with various ZnO morphology and different fabrication methods have been reported. DSSC based on hydrothermally synthesized ZnO nanorods have been reported. ZnO nanowires

shows improved electron transport compared to ZnO nanoparticles. One dimensional nanostructure has improved electron transport properties compared to nanoparticle films, but they have lower dye loading capacity due to lower surface area. There is a possible method to resolve this problem, is to mix nanowires and nanoparticles (hybrid morphology). Based on the comparison between the performance of DSSCs based on ZnO nanowires and nanowire/nanoparticle mixture found that cell efficiency can be considerably increased from 0.84% to 2.2% but efficiency in both cases was lower than that of TiO₂ based DSSCs (5%) [65]. Influence of morphology and surface area on DSSCs performance has been studied. It shows that the highest efficiency was obtained for ZnO with highest surface area with high dye loading.

Another type of low cost photovoltaics based on ZnO nanostructure is hybrid polymer solar cells. One of the important issues for solar cell application rather than power conversion efficiency is the device life time and stability. ZnO nanoparticle layer is used as an electron-selective contact in polymer solar cell with inverted structure.

1.7 Motivation of the Research work

In the past decades many zinc oxide (ZnO) nanostructures such as nanoparticles, nanorods, nanotubes nanobelts, nanowires, hollow beads, cones reefs, stars, pyramids, cages and shells, dandelions and even nanoflowers have been reported [66-74]. The corresponding methods for synthesizing these nanostructures vary from simple pyrolysis technique to strictly controlled vapour phase epitaxial growth. Physical properties of the final products were often determined by these synthesizing methods. For example, ZnO nanoparticle derived from sol-gel method is entirely different from hydrothermal method. Sol-gel derived particles mainly exhibit deep level emission (DLE) or visible fluorescence, while those nanoparticles with same size derived from hydrothermal methods exhibit near band edge emission (NBE) or UV emission.

In most cases of ZnO nanostructures have two components in the fluorescence emission (i) near band edge emission (ii) visible emission. Near band edge emission produces UV light of about 370 nm because room temperature

bandgap of ZnO is 3.37 eV. Deep level emission is associated with oxygen vacancies but this mechanism is controversial and not clear so far. Researchers reported two popular mechanisms for ZnO visible emission, one is the recombination of a shallowly trapped electron with a hole in a deep trap and other one is the recombination of an electron in singly occupied oxygen vacancies with photogenerated hole in the valence band. These two mechanisms have been coexisting for years because it is difficult to determine the exact location and energy level of the deep traps.

Guo and Co-workers showed that PVP modified ZnO exhibited enhanced UV emission with suppressed visible emission [75] compared with uncapped ZnO. Chang and co-workers also reported the same conclusion with polyaniline modification in ZnO. When metaloxide nanoparticles are synthesized in the presence of capping molecules like polymer, they easily got adsorbed on the surface of the particle. By chemical adsorption on to a polar plane of ZnO, the capping molecule like polymer can passivate facets of ZnO and thereby adjust the growth velocity among different facets and control the growth of ZnO nanoparticles. Surface passivation by PVP reduces surface defects so as to increase the UV emission of ZnO. In addition, relevant reports for unique chemical stability of nickel on zinc sites recognizes, nickel is one of the most efficient doping element to improve optical properties of ZnO.

The previous reports on PVP capped ZnO show that polymer is a best capping agent to produce nanorods with quenched visible emission. Since there is ample scope for enhancing the physico-chemical properties of ZnO composites by polymer capping, I tried ZnO with different catalyst during the synthesis. The aim was to improve the physical properties, mainly the emission spectra of ZnO metaloxide by surface passivation. Though different techniques are available for the synthesis, I tried the simpler and cheapest for developing an easy and economic route for the synthesis of nanomaterials. There are several metal oxides used as a catalyst during the growth of 1D nanostructure. Here I used some transition metals and rare earth metals as a catalyst for the synthesis of nanocomposites and used PVP as the capping agent.

References

- [1] C. Sanchez, H. Arribart and M. M. Giraud-Guille, *Nature Mater.*, 4 (2005) 277.
- [2] S. Mann, *Biomimetic Materials in Chemistry*, ed. S. Mann, Wiley- VCH, Weinheim, 1997.
- [3] H. Schmidt, A. Kaiser, H. Patzelt and H. Sholze, *J. Phys.*, 12 (1982) 275.
- [4] J. Livage, M. Henry and C. Sanchez, *Prog. Solid State Chem.*, 18 (1988) 259.
- [5] D. Avnir, D. Levy and R. Reisfeld, *J. Phys. Chem.*, 88 (1984) 5956.
- [6] Buffat, J. P. Bord, *Phys. Rev.*, 13 (1976) 2287.
- [7] E. O. Hall, *Proc. Phys. Soc. London B*, 64 (1951) 747.
- [8] N.J. Petch, *J. Iron Steel Inst.* 174 (1953) 25.
- [9] J. Schiötz, F. D. Di Tolla, K. W. Jacobsen, *Nature*, 391, (1998) 561.
- [10] Z. Zhung, X. Sun, M. S. Dresselhaus, J. Y. Ying, *Phys. Rev. B*, 61 (2000) 4850.
- [11] A. I. Yanson, G. R. Bollinger, H. E. Van Den Brom, N. Agrait, J. M. Van Ruitenbeek, *Nature*, 395 (1998) 783.
- [12] K. Schwab, E. A. Henriksen, J. M. Warlock, M.L. Roukes, *Nature*, 404 (2000) 974.
- [13] A. Buldum, S. Uruci, C. Y. Fong, *J. Phys. Condens. Mater.*, 12(2000) 3349.
- [14] S. G. Volz, G. Chen, *Appl. Phys. Lett.*, 75 (1999) 2056.
- [15] K. S. W. Sing, D. H. Everett, R. A.W. Haul, L. Moscou, R. A. Pierotti, J. Rouquerol, T. Siemieniewska, *Pure Appl. Chem.* 57 (1985) 603.
- [16] C. Liu, L. Zhang, J. Deng, Q. Mu, H. Dai, H. He, *J. Phys. Chem. C* 112 (2008) 19248.
- [17] J. Zhou, S. Yang, J. Yu, *Colloids Surf. A*. 379 (2011) 102.
- [18] Q. Wu, F. Zhang, J. Yang, Q. Li, B. Tu, D. Zhao, *Microporous Mesoporous Mater.* 143 (2011) 406.
- [19] H. Yoshitake, T. Sugihara, T. Tatsumi, *Chem. Mater.* 14 (2002) 1023.
- [20] F. Jiao, J. C. Jumas, M. Womes, A.V. Chadwick, A. Harrison, P.G. Bruce, *J. Am. Chem. Soc.* 128 (2006) 12905.

- [21] H. Liu, X. Du, X. Xing, G. Wang, S. Z. Qiao, *Chem. Commun.* 48 (2012) 865.
- [22] J. W. Lee, T. Ahn, J. H. Kim, J. M. Ko, J. D. Kim, *Electrochim. Acta* 56 (2011) 4849.
- [23] L. Cheng, M. Shao, D. Chen, Y. Zhang, *Mater. Res. Bull.* 45 (2010) 235.
- [24] C. Yuan, X. Zhang, B. Gao, J. Li, *Mater. Chem. Phys.* 101 (2007) 148.
- [25] Q. Chen, X. Shen, *Cryst. Growth Des.* 10 (2010) 3838.
- [26] J. Li, Y. Wei, W. Li, Y. Deng, D. Zhao, *Nanoscale* 4 (2012) 1647.
- [27] P. Kuhn, A. Forget, D. Su, A. Thomas, M. Antonietti, *J. Am. Chem. Soc.* 130 (2008) 13333.
- [28] P. Kuhn, M. Antonietti, A. Thomas, *Angew. Chem. Int. Ed.* 47 (2008) 3450.
- [29] A. P. Cote, A. I. Benin, N. W. Ockwig, M. O'Keeffe, A. J. Matzger, O. M. Yaghi, *Science* 310 (2005) 1166.
- [30] H. Wang, L. Wang, T. Sato, Y. Sakamoto, S. Tominaka, K. Miyasaka, N. Miyamoto, Y. Nemoto, O. Terasaki, Y. Yamauchi, *Chem. Mater.* 24 (2012) 1591.
- [31] V. Meyen, P. Cool, E. F. Vansant, *Microporous Mesoporous Mater.* 125 (2009) 170.
- [32] Z. Tao, B. Toms, J. Goodisman, T. Asefa, *ACS Nano* 4 (2010) 789.
- [33] J. Lu, M. Liang, Z. Li, J. I. Zink, F. Tamanoi, *Small* 6 (2010) 1794.
- [34] W. Di, X. Ren, H. Zhao, N. Shirahata, Y. Sakka, W. Qin, *Biomaterials* 32 (2011) 7226.
- [35] D. W. Wang, X. M. Zhu, S. F. Lee, H. M. Chan, H. W. Li, S. K. Kong, J. C. Yu, C. H. K. Cheng, Y. X. J. Wang, K. C. F. Leung, *J. Mater. Chem. B* 1 (2013) 2934.
- [36] M. Comes, M. D. Marcos, R. Martinez-Manez, F. Sancenon, L. A. Villaescusa, A. Graefe, G. J. Mohr, *J. Mater. Chem.* 18 (2008) 5815.
- [37] M. H. Huang, S. Mao, H. Feick, H. Yan, Y. Wu, H. Kind, E. Weber, R. Russo, P. Yang, *Science* 292 (2001) 1897.
- [38] A. B. Djurisic, A. M. C. Ng, X. Y. Chen, *Prog. In Quesnt. Electr.* 34 (2010) 259.

- [39] K. H. Yam, C. K. Cheung, Y. H. Heung, A. B. Djurisić, C. C. Ling, C. D. Beling, S. Fung, W. M. Kwurk, W. K. Chan, D. L. Philips, L. Ding, W. K. Ge, *J. Phys. Chem. B*, 110 (2006) 20865.
- [40] J. Jie, G. Wang, Y. Chen, X. Han, Q. Wang, B. Xu, J. G. Hou, *Appl. Phys. Lett.*, 86 (2005) 031909.
- [41] W. I. Park, Y. H. Jun, S. W. Jung, G. C. Yi, *Appl. Phys. Lett.*, 82 (2003) 964.
- [42] S. Ozaki, T. Tsuchiya, Y. Inokuchi, S. Adachi, *Phys. Stat. Sol. A*, 202 (2005) 1325.
- [43] A. B. Djurisić, Y. H. Leung, *Small*, 2 (2006) 944.
- [44] Q. X. Zhao, P. Klason, M. Willander, H. M. Zhong, W. Lu, J. H. Yang, *Appl. Phys. Lett.*, 87 (2005) 211912.
- [45] D. J. Zhang, Z. Y. Xue, Q. P. Wang, *J. Phys. D: Appl. Phys.*, 35 (2002) 2387.
- [46] A. B. Djurisić, Y. H. Leung, *Small*, 2 (2006) 944.
- [47] M. D. McCluskey, S. J. Jokela, *J. Appl. Phys.*, 106 (2009) 071101.
- [48] J. P. Richters, T. Voss, L. Wischmeir, I. Ruckmann, J. Gutowski, *Appl. Phys. Lett.* 92 (2008) 011103.
- [49] S. M. Abarrov, S. H. U. Yuldashev, T. W. Kim, S. B. Lee, Y. H. Known, T. W. Kang, *Opt. Commu.* 250 (2005) 111.
- [50] W. M. Kwok, A. B. Djurisić, Y. H. Leung, W. K. Chan, O. L. Philips, *Appl. Phys. Lett.*, 87 (2005) 223111.
- [51] S. Hong, T. Joo, W. I. Park, Y. H. Jun, G. C. Yi, *Appl. Phys. Lett.* 83 (2003) 4157.
- [52] E. Erhart, K. Albe, A. Klein, *Phys. Rev. B*, 73 (2006) 205203.
- [53] S. Lang, A. Zunger, *Phys. Rev. Lett.*, 98 (2007) 045501.
- [54] Y. Sun, H. Wang, *Physica B*, 325 (2003) 157.
- [55] M. Lannoo, J. Bourrguin (1981), *Point Defects In Semiconductor I: Theoretical Aspects* (Berlin: Springer)
- [56] S. T. Pantelides, 1992 *Deep Centers In Semiconductors : A State Of The Art Approach* 2nd Edn.

- [57] M. Stavola, 1999 Identification Of Defects In Semiconductors, Semiconductors And Semimetals Vol 51 B (San Diego: Academic)
- [58] C. Kittel 2005 Introduction To Solid State Physics 8th Edn. (New York: Wiley)
- [59] M. Lannoo, J. Bourguin (1981), Point Defects In Semiconductor I: Theoretical Aspects (Berlin: Springer)
- [60] S. T. Pantelides, 1992 Deep Centers In Semiconductors: A State Of The Art Approach 2nd Edn.
- [61] M. E. Glicksman 2000 Diffusion in solids: Field theory, solid state Principles and applications (New York: Wiley)
- [62] P. D. Batista and M. Mulato, *Appl. Phys. Lett.*, 87(2005) 143508.
- [63] I. Gonzalez-Valls, M. Lira-Cantu, *Energy Environ. Sci.*, 2 (2009) 19.
- [64] M. Law, L. E. Greene, J. C. Johnson, R. Saykally, P. Q. Yang, *Nat. Mater.* 4 (2005) 455.
- [65] C. H. Ku, J. J. Wu, *Appl. Phys. Lett.* 91 (2007) 093117.
- [66] B. Liu, H. C. Zeng, *J. Am. Soc.*, 125 (2003) 4430.
- [67] P. X. Gao, Z. L. Wang, *Small* 1 (2005) 945.
- [68] H. Yu, Z. Zhang, M. Han, F. Zhu, *J. Am. Chem. Soc.* 127 (2005) 2378.
- [69] M. H. Huang, S. Mao, H. Feick, H. Yan, Y. Wu, H. Kind, E. Weher, R. Russo, P. Yang, *Science* 29 (2001) 1897.
- [70] S. Gao, H. Zhang, X. Wang, R. Deng, D. Sun, G. Zheng, *J. Phys. Chem. B*, 110 (2006) 15847.
- [71] J. Joo, S. G. Kwon, J. H. Yu, T. Hyeon, *Adv. Mater.* 17 (2005) 1873.
- [72] J. H. Choy, E. S. Jang, J. H. Won, J. H. Chung, D. J. Jang, Y. W. Kim, *J. Appl. Phys. Lett.*, 87 (2005) 13.
- [73] Y. Lv, C. Li, L. Guo, Q. Wang, R. Wang, H. Xu, S. Yang, X. Ai, J. Zhang, *Appl. Phys. Lett.* 87 (2005) 14792
- [74] S. H. Choi, E. G. Kim, J. Park, K. An, N. Lee, S. C. Kim, T. Heon, *J. Phys. Chem. B* 109 (2005) 1479
- [75] P. X. Gao, Z. L. Wang, *J. Am. Chem. Soc.* 125 (2003) 11299.

Chapter 2

Synthesizing strategies and characterization tools

This chapter introduces the synthesising routes for preparing ZnNiO and its composites with aluminium oxide, cupric oxide, palladium oxide, dysprosium oxide, and cerium oxide, and the characterisation techniques for exploring the structure and properties of the compounds.

2.1 Introduction

The shape of the crystal is determined by the relative specific surface energies associated with the facets of the crystal. According to Wulff facets theorem, at equilibrium condition crystal has to be bounded by facets giving a minimum surface energy. The shape of the crystal is also considered in terms of growth kinetics by which the fastest growing planes should disappear to leave behind the slowest growing plane [1]. This argument implies that final shape of the crystal is controlled by introducing appropriate surface modifiers (capping agents) [2]. These capping agents change the free energies of the crystallographic surfaces and thus alter their growth rate and it shows mesoporosity.

2.2 Mesoporous synthesizing strategies

There are several synthesizing strategies for the development of mesoporous materials. Some of them are based on the use of organic templates as structure directing agents. This method is called soft-template method and another method called hard template method, uses inorganic silica and carbon are used as the template.

2.2.1 Soft template method

In this approach, the organic template is removed by calcination after the formation of mesophase. This generates the ordered mesoporous structures. Whose mesoporous sizes can be tuned by using different structure directing agents or different concentrations of surface directing agents. Widely used templates for the preparation of mesoporous materials are cationic [3], amphibilic [4] and anionic [5] surfactants, chiral peptide-modified surfactants [6], emulsions [7], vitamin derivatives [8], ionic liquids [9] and biological materials [10]. This strategy allows the precise control over the particle morphology, pore diameter and mesoporosity. Mesoporous materials may exhibit different morphologies of particles such as spheres [11], hollow spheres [12], rods [13] and others [14]. It is a simple technique gives good shape, size and morphology to the particles. Schematic representation of soft template method is shown in fig 2.1.

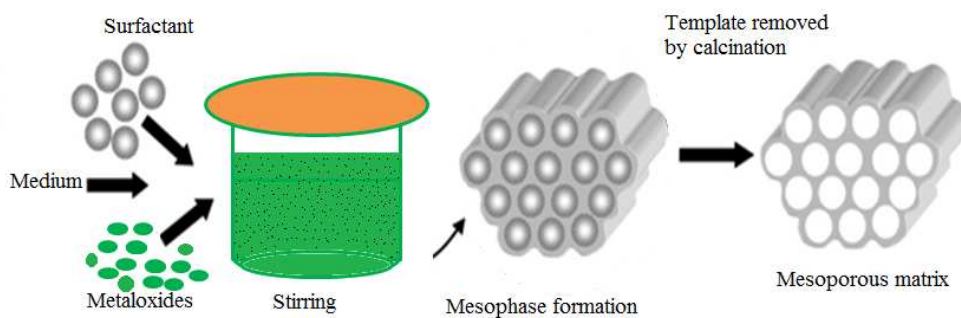


Figure: 2.1: Schematic representation of soft template method.

2.2.2 Hard template method

The second method involves the use of hard template such as porous silica for the preparation of mesoporous materials. This method is commonly applied for the synthesis of mesoporous carbon [15]. In this case mesoporous template is loaded with organic materials and this organic filler is carbonized in the vacuum. Dissolution of silica shell by sodium hydroxide (NaOH) results uncovering carbon frame work. In this method, it is hard to get good morphology and it is very costly. Schematic representation of hard template method is shown in fig.2.2.

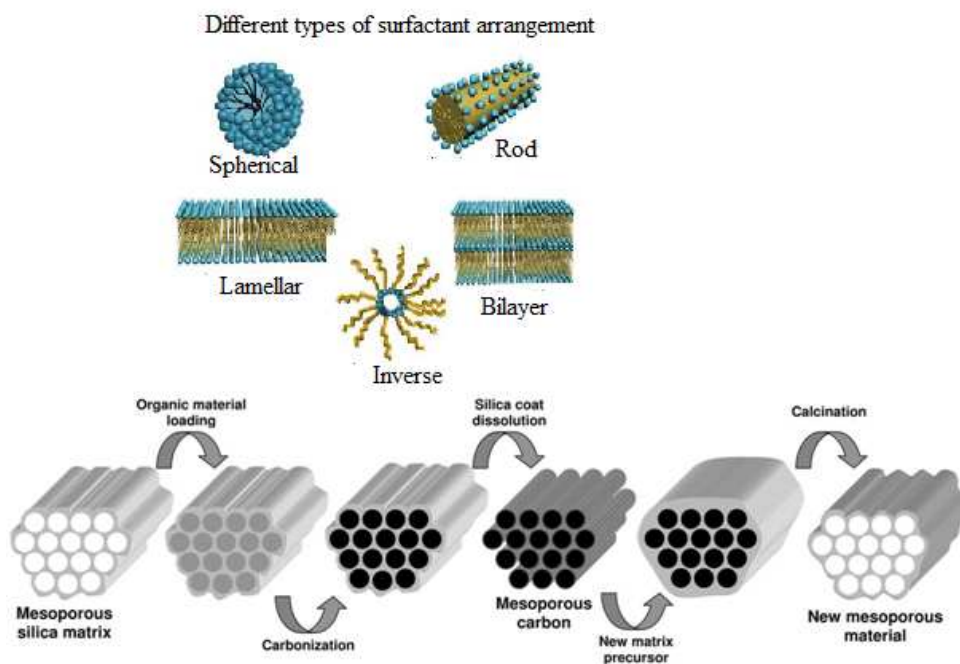


Figure: 2.2: Schematic representation of hard template method

2.3 Role of capping agents

Typically nanoparticles are synthesized in solution method by reacting metal precursors with appropriate reducing agents in the presence of capping agents to stabilize the high energy surface of the nanoparticles and also it protects the particle from agglomeration. Capping agents play an important role in the synthesis of nanoparticles. For instance, capping agents often act as a ligand and it forms complexes with metal precursors and thereby it affects the growth kinetics. Another important role played by capping agents is their selective adsorption on particular crystallographic planes that induces the anisotropic growth.

2.3.1 Exploitation of Polyvinyl pyrrolidone (PVP-30K)

Polyvinyl pyrrolidone (PVP) is a surface directing agent to control nucleation and alignment of crystals. The exploitation of PVP is motivated by a reason that by coordinating the water from the dehydration reaction of the ZnO precursor, PVP may accelerate the crystal formation and promote the crystallization of ZnO. In aqueous solution of PVP, water can be bound and this solution containing high concentration of PVP, wherein this condition water molecule doesn't act as a solvent but is referred to a "bound water" [16]. Furthermore PVP is extensively used as the stabilizer in nanotechnology because of its excellent adsorption ability. Compared to reported directing agents such as poly (vinyl alcohol), citrates, acetate, cetyltrimethyl ammonium bromide (CTAB), peptide, ammonia, Tween -85 ($C_{100}H_{188}O_{28}$) and KBr, polyvinyl pyrrolidone is a cheap, bio compatible reagent and it is also a pharmaceutical product additive. Furthermore PVP capped ZnO shows an excellent optical property.

2.4 Zinc nickel oxide (ZnNiO)

Oxide based diluted magnetic semiconductors (DMS) such as transition metal doped semiconductors with room temperature ferromagnetism (RTFM) have been studied for advanced applications in spintronic devices where the effort was made to find the ways for the utilization of nanoparticles in both information processing and data storage within one material system. In recent studies, DMSs are formed by the potential substitution of the cations of the host semiconductors with small amount of transition metal ions [17].

The transition metals doping in ZnO facilitates the generation of carrier mediated ferromagnetism [18]. Several researchers addressed room temperature ferromagnetic behaviour of 3d transition metals (such as Fe, Ni, Mn, Co, Cr, etc.) doped ZnO [19-20]. Among them, Ni is an important dopant to achieve Curie temperature above room temperature. It is well known that transition metal ion substitution in ZnO semiconductors exhibit sp-d hybridisation [21]. The s-d and p-d exchange interaction between the band electrons and localised 3d electrons makes

positive and negative corrections in the valence band and the conduction band respectively. This leads to the red shift in the near band edge emission and also increasing green emission.

In addition, relevant reports for ZnO doped with metal (Al, Pd and Cu) indicate that the doping effect increased optical and electrical effects of ZnO. The photoluminescence characteristics of aluminium doped ZnO show that the optical quality degenerated gradually with increasing aluminium concentration and the presence of copper has been reported to increase the intensity of deep trap emission ZnO as well as the intensity of band gap emission of ZnO. So I tried to introduce Al, Cu and Pd in ZnO to enhance the optical properties and magnetic properties. Palladium a 4d metal is taken as a impurity in ZnO significantly improves sensitivity and specificity of hydrogen. Rare earth elements cerium and dysprosium are technologically important material because of its unique properties and various biological applications.

2.4.1 Synthesis of ZnNiO based mesoporous nanocomposites

A simple cost effective soft template method is used for the synthesis of surface passivated nanocomposites (ZnNiO, Al:ZnNiO, Cu:ZnNiO, Pd:ZnNiO, Dy:ZnNiO and Ce:ZnNiO). Here the nanocomposites were synthesized by dissolving zinc nitrate hexahydrate (99.99%), nickel nitrate hexahydrate (99.99%) in de-ionized water. These metal nitrates were purchased from Sigma Aldrich and used without further purification. Poly vinyl (pyrrolidone -30K) (PVP) was used as the additive surfactant. The mixed solution of zinc nitrate (0.5 M), nickel nitrate (0.2M) was precipitated in NaOH (0.5M) solution. After vigorous stirring for about 1 h, the suspension was filtered and washed in de-ionized water several times to remove biproducts. The filtrate was made into paste in 2g PVP solution and dried at 70°C, until the mixture turns into powder form. The final product was calcined at 300°C for 4 hrs. Doping with post transition metal (Al), transition metals (Cu and Pd) and rare-earth metals (Dy, Ce) were accomplished in the same procedure by adding 0.05M (aluminium nitrate, cupric nitrate, palladium nitrate, dysprosium nitrate and cerium nitrate) solution sequentially in the mixture of zinc-nickel nitrate solution. Then NaOH was added drop wisely in the mixture of three metal nitrate solutions.

The precipitate was centrifuged and washed several times in to remove byproducts and PVP added. This suspension was dried in the oven at the same temperature mentioned above and calcined at 200°C. The products were subjected to various physical and chemical examinations.

2.4 Characterization techniques

The crystallographic information of the as prepared composites were investigated by powder X-ray diffractometer (Rigaku Miniflex 600) with $\text{CuK}\alpha$ radiation, ($\lambda = 0.15406 \text{ nm}$) and morphology of the sample was characterized and analyzed by Field Emission Scanning Electron Microscopy, FESEM. Chemical composition of the composite were analysed by using energy dispersive x-ray Spectrometer, which was attached to the SEM instrument. The specific surface areas of the sample were determined from nitrogen adsorption isotherms using a Micrometrics Gemini Surface Area and Porosity Analyzer. Diffuse reflectance spectra of the nanocomposites were characterized by using UV-Vis NIR spectrophotometer in the wavelength range from 350-600 nm. Room temperature fluorescence measurements were carried out by a fluorescence spectrometer and magnetic studies of the nanocomposites were analyzed by Vibrating sample magnetometer (VSM).

2.5.1 X-ray diffractometer

X-ray powder diffraction (XRD) is a rapid analytical technique primarily used for phase identification of a crystalline material and can provide information on unit cell parameters, volume, density etc. X-ray diffraction is based on constructive interference of monochromatic X-rays and a crystalline sample. X-ray diffractometer consist of three basic elements: an X-ray tube, a sample holder, and an X-ray detector. X- Rays are generated in a cathode ray tube by heating a filament to produce electrons, accelerating the electrons toward a target by applying a voltage, and bombarding the target material with electrons. When electrons have sufficient energy to dislodge inner shell electrons of the target material, characteristic X-ray spectra are produced. Copper is the most common target material for single-crystal diffraction, with $\text{CuK}\alpha$ radiation = 1.5418\AA . These X-rays are collimated and directed onto the sample. As the sample and detector are rotated,

the intensity of the reflected X-rays is recorded. When the geometry of the incident X-rays impinging the sample satisfies the Bragg Equation, $n\lambda = 2d \sin \theta$, constructive interference occurs and a peak in intensity occurs. A detector records and processes this X-ray signal and converts the signal to a count rate which is then output to a device such as a printer or computer monitor.

2.5.2 Field Emission Scanning Electron Microscopy (FESEM)

The scanning electron microscope (SEM) enables the investigation of specimens with a resolution down to the nanometer scale. Here an electron beam is generated by an electron cathode and the electromagnetic lenses of the column and finally swept across the surface of a sample. A normal scanning electron microscope operates at a high vacuum. The basic principle is that a beam of electrons is generated by a suitable source, typically a tungsten filament or a field emission gun. The electron beam is accelerated through a high voltage and pass through a system of apertures and electromagnetic lenses to produce a thin beam of electrons, then the beam scans the surface of the specimen.

2.5.3 Energy Dispersive X-ray Spectra (EDS)

Energy dispersive X-ray analysis, also known as EDX, or EDAX, is a technique used to identify the elemental composition of a sample. During EDS, a sample is exposed to an electron beam inside a scanning electron microscope (SEM). These electrons collide with the electrons within the sample, causing some of them to be knocked out of their orbits. The vacated positions are filled by higher energy electrons which emit x-rays in the process. By analyzing the emitted x-rays, the elemental composition of the sample can be determined. EDS is a powerful tool for microanalysis of elemental constituents.

2.5.4 Vibrating Sample Magnetometer (VSM)

Magnetic properties of the samples were studied at room temperature, by using a vibrating sample magnetometer (VSM). A vibrating sample magnetometer (VSM) operates on Faraday's Law of Induction, which tells us that a changing magnetic field will produce an electric field. A VSM operates by first placing the sample to be studied in a constant magnetic field. If the sample is magnetic, this constant

magnetic field will magnetize the sample by aligning the magnetic domains or the individual magnetic spins, with the field. The stronger the constant field, the larger the magnetization will be. The magnetic dipole moment of the sample will create a magnetic field around the sample. As the sample is moved up and down, this magnetic field is changing as a function of time and can be sensed by a set of pick-up coils. The alternating magnetic field will cause an electric field in the pick-up coils according to Faraday's Law of Induction. This current will be proportional to the magnetization of the sample. The induction current is amplified by a transimpedance amplifier and lock-in amplifier. The various components are hooked up to a computer interface. Using controlling and monitoring software, the system can tell you how much the sample is magnetized and how its magnetization depends on the strength of the constant magnetic field.

2.5.5 Diffuse reflectance spectroscopy (DRS)

The UV-Vis spectroscopy is frequently used to characterize semiconductor thin films [22]. It is easy to extract their bandgap values from absorption spectra (knowing their film thickness) because of low scattering in films. Scattering effect in colloidal sample is enhanced since more area is exposed to the light beam. In normal incidence mode dispersed light is counted as the absorbed light. In case of powdered samples UV-absorption spectroscopy is carried out by dispersing the sample in water, ethanol or methanol. If the size of the particle is small enough, it will precipitate and UV spectrum becomes more complicated to interpret. In order to avoid these types of problems, desirable to do diffuse reflectance spectra (DRS).

Kubelka-Munk was proposed a theory, which makes possible to use DRS spectroscopy [23]. They proposed a model to describe the behaviour of light inside a light scattering material based on the equations.

$$\frac{-di}{dx} = -(S + K)i + Sj \quad (2.1)$$

$$\frac{dj}{dx} = -(S + K)j + Si \quad (2.2)$$

Where i and j are the intensities of light travelling inside the material towards unilluminated and illuminated surfaces. S and K are the scattering and absorption

coefficient respectively. Where dx is the differential segment along the path. In the limiting case of an infinitely thick sample, thicknesses of the sample holder have no influence on reflectance. So Kubelka-Munk equation at any wavelength becomes

$$K / S = \left(\frac{1 - R_{\infty}}{2R_{\infty}} \right) = F(R_{\infty}) \quad (2.3)$$

$F(R_{\infty})$ is the re-emission function.

2.5.6 Fluorescence spectroscopy

Fluorescence is a photon emission process that occurs during molecular relaxation from electronic excited states. This photonic process involves transition between electronic and vibrational states of fluorophores. The fluorophore remains in the lowest vibrational states of the excited electronic state for a period on the order of nanoseconds is called the fluorescence life time. Fluorescence emission in the molecule occurs as the fluorophore decay from the singlet electronic states to an allowable vibrational level in the electronic ground state. Molecules in the excited electronic states relax by radiative and nonradiative process. Radiative decay process describes molecular deexcitation processes accompanied by photon emission. In nonradiative process excitation energy is not converted into photons but it is dissipated by thermal processes such as vibrational relaxation and collisional quenching. Fluorescence is the result of a three-stage process that occurs in fluorophores.

Stage 1: Excitation. A photon is supplied by an external source such as an incandescent lamp or a laser and this is absorbed by the fluorophore, creating an excited electronic singlet state (S1'). This process distinguishes fluorescence from chemiluminescence, in which the excited state is populated by a chemical reaction.

Stage 2: Excited-State Lifetime. The excited state exists for a finite time (typically 1–10 nanoseconds). During this time, the fluorophore undergoes conformational changes and is also subject to a multitude of possible interactions with its molecular environment.

Stage 3: Fluorescence Emission. Energy of photon is emitted, returning the fluorophore to its ground state S_0 . Due to energy dissipation during the excited-state lifetime, the energy of this photon is lower, and therefore of longer wavelength, than the excitation photon. The difference in energy or wavelength represented by the absorbed and emitted photon is called the Stokes shift. The Stokes shift is fundamental to the sensitivity of fluorescence techniques because it allows emission photons to be detected against a low background, isolated from excitation photons.

2.5.6 Surface area Analyzer (Adsorption measurements)

Gas adsorption method is a technique used to characterize the solid samples. It is designed to perform physical adsorption and chemisorptions for the determination of specific surface area and porosity. Adsorption measurement is one of the most diffuse techniques to characterize porous nanomaterials and to estimate the surface area, the porosity and pore size distribution of the materials. Adsorption happens when gaseous or vapour molecules interact with a solid surface, passing from the gaseous phase to an adsorbed state. In a typical adsorption measurement a solid is put in contact with a defined amount of a pure substance, or a mixture with known composition, to study the specific interaction between the two phases. Concerning nanoporous materials, adsorption phenomenon is generally rare and they are investigated only by adsorption techniques. Adsorbed material is generally classified as exhibiting physisorption or chemisorption.

Physisorption

Physisorption or physical adsorption is a type of adsorption in which the adsorbate adheres to the surface only through Van der Waals (weak intermolecular) interactions. Physisorption occurs at any environmental condition but it is measurement at low temperature, usually at the boiling temperature of liquid nitrogen at atmospheric pressures. Presence of an intrinsic energy is the reason for taking place adsorption. When the material is exposed to a gas, an attractive force acts between the exposed surface of the solid and the gas molecule. This force is characterized as a physical adsorption.

Due to the weak bonds involved between the gas molecules and the surface adsorption is a reversible phenomenon. The complete adsorption/desorption analysis is called adsorption isotherm. Once the isotherm is obtained, a number of calculation models (BET, Dubinin, Langmuir) can be applied to different regions of the adsorption isotherm to evaluate the surface area.

Chemisorption

Chemisorption is a type of adsorption whereby a molecule adheres to a surface through the formation of a chemical bond, as opposed to the Van der Waals forces. Adsorption is usually described through isotherms, that is, functions which connect the amount of adsorbate on the adsorbent, with its pressure (if gas) or concentration (if liquid). Several models can be describing the process of adsorption, namely; Freundlich isotherm, Langmuir isotherm, BET isotherm, etc.

BET model

BET theory aims to explain the physical adsorption of gas molecules on a solid surface and serves as the basis for an important analysis technique for the measurement of the specific surface area of a material. In 1938, Stephen Brunauer, Paul Hugh Emmett, and Edward Teller published an article [24] about the BET theory in a journal for the first time; “BET” consists of the first initials of their family names. The concept of the theory is an extension of the Langmuir theory [25], which is a theory for monolayer molecular adsorption, to multilayer adsorption with the following hypotheses: (a) gas molecules physically adsorb on a solid in layers infinitely; (b) there is no interaction between each adsorption layer; and (c) the Langmuir theory can be applied to each layer. The specific surface area of a powder is determined by physical adsorption of a gas on the surface of the solid and by calculating the amount of adsorbate gas corresponding to a monomolecular layer on the surface. Physical adsorption results from relatively weak forces (Vander Waals forces) between the adsorbate gas molecules and the adsorbent surface area of the test powder. The determination is usually carried out at the temperature of liquid nitrogen. The amount of gas adsorbed can be measured by a volumetric or continuous flow procedure.

The Brunauer-Emmett-Teller method is the most widely used procedure for the determination of the surface area of solid materials. Total surface area S_{total} and a specific surface area S are evaluated by the following equation.

$$S_{BET, total} = \left(\frac{V_m N S}{V} \right) \quad (2.4)$$

where V_m is in units of volume which are also the units of the molar volume of the adsorbent gas

$$S_{BET} = S_{total} / a \quad (2.5)$$

N stands for Avogadro's number, s : adsorption cross section of the adsorbing species, V : molar volume of adsorbent gas. a : mass of adsorbent (in g)

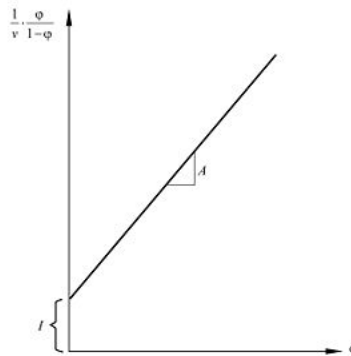


Figure 2.3: BET Plot

Procedure

Static volumetric adsorption requires a high vacuum pumping system able to generate a good vacuum over the sample of at least 10^{-4} Torr. The experiment is carried out by starting from high vacuum and increasing step by step, the pressure upto adsorbate saturation pressure.

Introducing consecutive known amount of adsorbate to the sample holder, this is kept at liquid nitrogen temperature (77K). Adsorption of the injected gas into the sample causes the pressure to slowly decrease until an equilibrium pressure is

established in the manifold. The equilibrium pressure is measured by a transducer chosen according to the pressure range. The gas uptake is directly calculated from the equilibrium pressure values but a dead volume calibration has to be performed before and after the measurement by a blank run.

References

- [1] J. A. Venables, Introduction to surface and Thin Film process Cambridge University Press, Cambridge 2000, 4.
- [2] H. M. Xiong *J. Mater. Chem.*, 20 (2010) 4251.
- [3] J. S. Beck, J. C. Vartuli, W. J. Roth, M. E. Leonowicz, C. T. Kresge, K. D. Schmitt, C. T. W. Chu, D. H. Olson, E. W. Sheppard, S. B. McCullen, J. B. Higgins, J. L. Schlenker, *J. Am. Chem. Soc.* 114 (1992) 10834.
- [4] Z. Jin, X. Wang, X. Cui, *Colloids Surf. A* 316 (2008) 27.
- [5] T. Yokoi, H. Yoshitake, T. Tatsumi *Chem. Mater.* 15 (2003) 4536.
- [6] K. Ariga, T. Aimiya, Q. Zhang, A. Okabe, M. Niki, T. Aida, *Int. J. Nanosci.* 1 (2002) 521.
- [7] Y. G. Lee, C. Oh, S. K. Yoo, S. M. Koo, S. G. Oh, *Microporous Mesoporous Mater.* 86 (2005) 134.
- [8] D. Coutinho, R. A. Orozco-Tevan, R. F. Reidy, K. J. Balkus Jr, *Microporous Mesoporous Mater.* 54 (2002) 229.
- [9] N. Zilkova, A. Zukal, J. Cejka, *Microporous Mesoporous Mater.* 95 (2006) 176.
- [10] X. Sun, C. Zheng, M. Qiao, J. Yan, X. Wang, N. Guan, *Chem. Commun.* (2009) 4750.
- [11] W. Cheol, A. Stein, *Chem. Mater.* 23 (2011) 1761.
- [12] Z. Teng, X. Su, Y. Zheng, J. Sun, G. Chen, C. Tian, J. Wang, H. Li, Y. Zhao, G. Lu, *Chem. Mater.* 25 (2013) 98.
- [13] H. Wang, P. Van Der Voort, H. Qu, S. Liu, *J. Nanoparticle Res.* 15 (2013) 1501.
- [14] D. Zhao, P. Yang, Q. Huo, B. F. Chmelka, G. D. Stucky, *Curr. Opin. Solid State Mater. Sci.* 3 (1998) 111 *Am. Chem. Soc.* 122 (2000) 10712.
- [15] A. P. Mackenzie, D. H. Hamann, Water structure at the water-polymer interface (Ed: H. H. G. Jellinek) John Wiley, New York 1972.
- [16] M. G. Pei, C. Xia, B. Wu, T. Wang, L. Zhang, Y. Dong, J. Xu, *Comput. Mater. Sci.* 43 (2008) 489.

- [17] S. J. Pearton, C. R. Abernathy, M. E. Overberg, G. T. Thaler, D. P. Norton, N. Theodoropoulou, A. F. Hebard, Y. D. Park, F. Ren, J. Kim, L. A. Boatner, *J. Appl. Phy.* 93 (2003) 1.
- [18] P. V. Radovanovic, D. R. Gamelin, *Phy. Rev. Lett.* 91 (2003) 157202.
- [19] N. S. Norberg, K. R. Kittilstved, J. E. Amonette, R. K. Kukkadapu, D. A. Schwartz, D. R. Gamelin, *J. Am. Chem. Soc.* 126 (2004) 9387.
- [20] K. J. Chen, T. H. Fang, F. Y. Hung, L.W. Ji, S. J. Chang, S. J. Young, Y. J. Hsiao, *Appl. Surf. Sci.* 254 (2008) 5791.
- [21] U. Paul, D. Samanta, S. Ghorai, A.K. Chaudhari, *J. Appl.Phys.*74 (1993) 6368.
- [22] P. Kubelka, F. Munk, *Z. Tech, Phys.*12 (1931) 593.
- [23] S. Brunauer, P. H. Emmett, E. Teller, *J. Amer. Chem. Soc.*, 60 (1938) 309.
- [24] I. Langmuir, *J. Amer. Chem. Soc.* 38 (1916) 2263.

Chapter 3

Capping effects on structure and morphology of ZnNiO based nanocomposites

3.1 Introduction

Zinc oxide (ZnO) belongs to the group of II-VI semiconductors, crystallizes in the hexagonal wurtzite (WZ) structure and belongs to the $P6_3mc$ space group. Besides the lattice parameters a and c wurtzite structure has one free internal parameter u which specifies the bond length parallel to the c axis [Fig.3.1]. Under ideal condition, ie all bond lengths and bond angles are same, u will be 0.375 [1]. The lattice parameters of the hexagonal unit cells mostly range from 0.3247 to 0.32501 nm for a and from 0.5204 to 0.5207 nm for c . The density of ZnO is 5.606 g/cm³ [2]. ZnO is a polar crystal consisting of a negative polar plane and a positive polar plane. In addition to polar surfaces, it has also a non polar plane [3]. When the bond along the c -direction are from cation (Zn) to anion (O) the polarity is referred to as Zn polarity, while when the bonds along the c -direction are from anion (O) to the cation (Zn) the polarity is referred to as oxygen polarity. The four most common faces of wurtzite ZnO are the Zn-terminated (0001) and O-terminated (000 $\bar{1}$) faces (c -axis oriented), and the non-polar (2 $\bar{1}$ $\bar{1}$ 0) (a -axis) and (01 $\bar{1}$ 0) faces which contain an

equal number of Zn and O atoms. It has been observed that the origination of various shapes of the ZnO crystals is due to the relative growth rates of different crystal facets and differences in the growth rates of different crystal planes [4]. Here we investigated, structure and morphology of the ZnNiO based nanocomposites synthesised by soft template method.

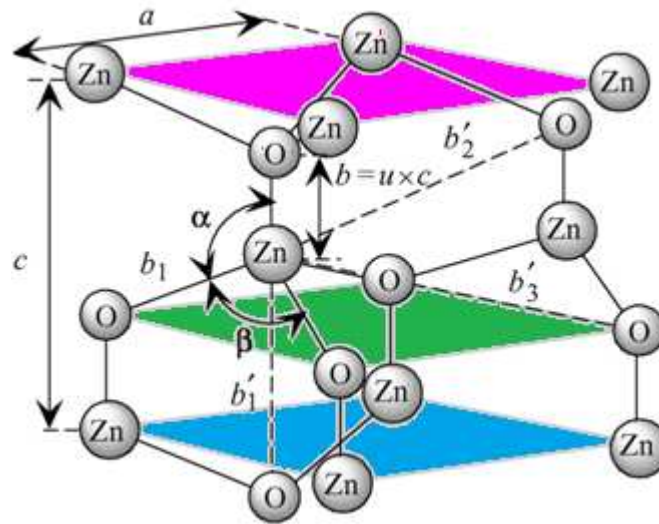


Figure 3.1: Wurtzite structure of ZnO showing a , c and u parameters

3.2 Structural Analysis

Crystal structure of the prepared nanocomposites were confirmed by powder X-ray diffractometer (Rigaku Miniflex 600 with scan rate $1^\circ/\text{min}$ and $\text{CuK}\alpha$ radiation, $\lambda = 0.15406 \text{ nm}$). X-ray diffraction patterns of the ZnNiO nanocomposites after and before surface passivation were investigated. These composites doped with various transition metals (Al, Pd & Cu) and rare earth metals (Dy & Ce) were also investigated.

3.2.1 XRD patterns of ZnNiO and ZnNiO/PVP nanocomposites

XRD patterns of the uncapped and capped ZnNiO nanocomposites were compared and are shown in Fig.3.2 (a) & (b). Fig 3.2(a) shows the XRD patterns of the as-synthesized uncapped ZnNiO and capped ZnNiO. These samples showed semi-crystalline nature even before performing calcinations and the grain size obtained

was so small (~ 3.5 nm). The average crystallite size were calculated using the Debye - Scherrer formula, ($D = 0.9\lambda/\beta\cos\theta$), where λ is the x-ray wavelength, β is the full width half maximum of the most intense peak. After undergoing calcinations, crystallinity of the samples increased and particles grew bigger in size.

Fig. 3.2(b) shows XRD patterns of the calcined samples of (a) pure ZnO (b) uncapped ZnNiO (c) PVP capped ZnNiO at 300 °C respectively. By incorporating Ni, the sample has not been deviated from its parental wurtzite structure which indicates that the dopant Ni^{2+} ions (radius 0.069 nm) are effectively substituted in the inner lattice of Zn^{2+} ions (radius 0.074 nm). After calcination crystallites size increases from 3.5 nm to 27.5nm for capped ZnNiO. The peaks of capped ZnNiO corresponds to hexagonal wurtzite structure of ZnO (ICDD number 01-078-3344) and this peaks originates from (100), (002), (101), (102), (110), (103), (200), (112), (201), (202) reflections [seen from Fig.3.3]. This indicates that crystal structure of ZnO is not modified due to the presence of nickel or PVP capping.

The main structural parameter such as crystallite size was calculated from the peak width analysis. In general, crystallite size of the material is a measure of the size of a coherently diffraction domain. The lattice parameters in semiconductors mainly depend on the parameters such as defects, external strain, foreign contents and the differences in the ionic radii of the dopant. Lattice parameters calculated from the diffraction peaks are shown in table 3.1. The decrease of the lattice parameter indicates that Ni^{2+} is introduced into the ZnO/PVP crystal lattice and substituting the Zn^{2+} site [5].

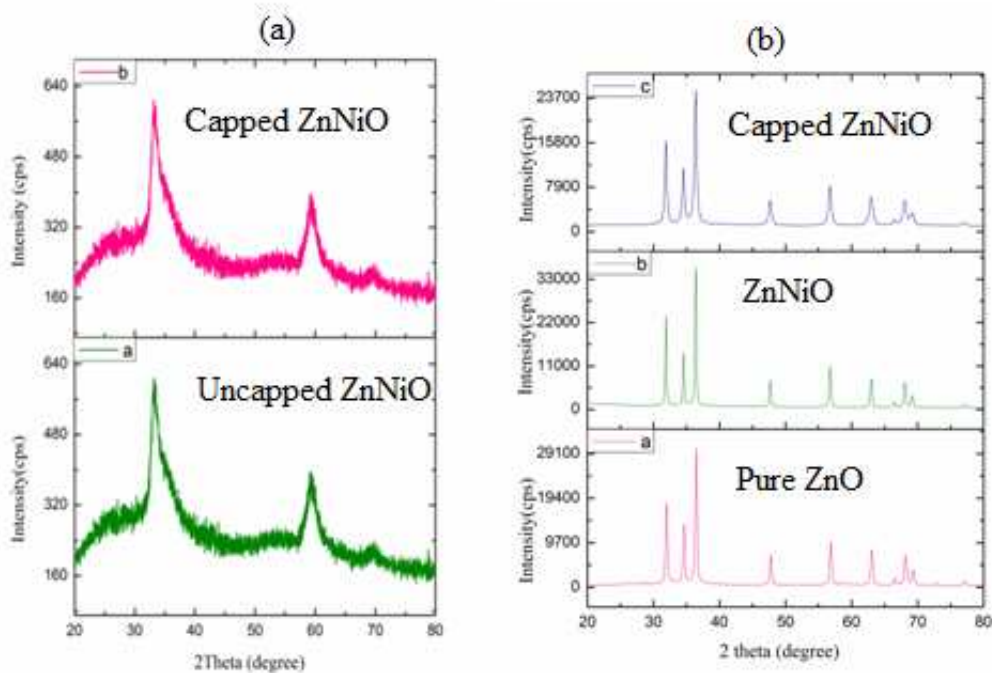


Figure 3.2: (a) X-ray diffraction patterns of as-synthesized form of uncapped and capped ZnNiO (b) calcined form of pure ZnO, uncapped ZnNiO, and capped ZnNiO at 300 °C.

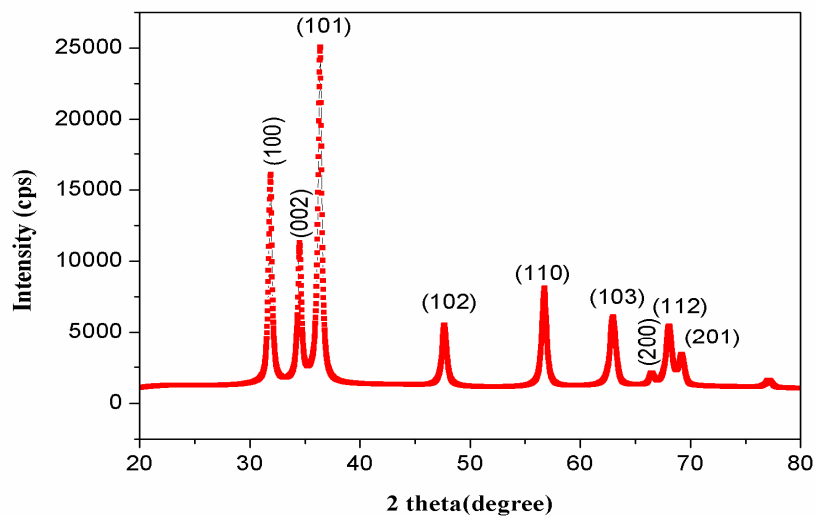


Figure 3.3: Indexed XRD pattern of polymer capped ZnNiO

3.2.2 XRD patterns of Al:ZnNiO, Pd:ZnNiO and Cu:ZnNiO nanocomposites

Appendage of aluminium, palladium and copper in polymer capped ZnNiO nanocomposites shows excellent crystallinity as that of polymer capped ZnNiO

nanocomposites. Xrd patterns of these samples are shown in fig 3.4. These results show that crystallographic phases of these double doped compounds are belongs to the standard crystallographic structure of hexagonal ZnNiO (ICDD no. 01-071-6735). The sharp XRD peaks confirm the formation of good crystalline phases of the nanocomposites which originates from (100), (002), (101), (102), (110), (103), (200), (112), (201), (202) reflections. The lattice constants of these samples are shown in table 3.1. But copper adjunction in ZnNiO shows a trace amount of NiO (200) phase because Ni ions did not enter in the crystallite site of ZnO and crystallized alone forming NiO grains in the composite phase.

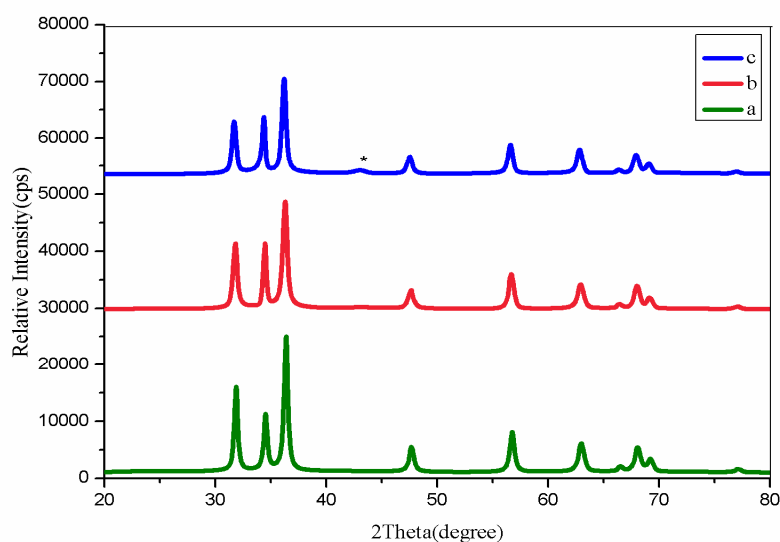


Figure 3.4: Xrd pattern of polymer capped (a) Al:ZnNiO (b) Pd:ZnNiO (c) Cu:ZnNiO nanocomposites

3.2.3 XRD patterns of Dy:ZnNiO and Ce:ZnNiO nanocomposites

X-ray diffraction studies of rare- earth metals (Dy & Ce) doped ZnNiO/PVP were also investigated. These nanocomposites show good crystallinity and calculated grain size is in the nano range. Structure of the cerium doped samples doesn't deviate from the parental structure but in the case of dysprosium doped samples, it is indexed to the hexagonal structure of ZnNiO. Calculated grain size, lattice parameters and density of all the samples are shown in table 3.1. The grain growth is mainly due to movement and diffusion of Zn^{2+} . However, in the case of Ni doped

ZnO, Ni may exist as the grain in the boundary, which can enhance the energy barrier for the movement and diffusion of Zn^{2+} . It was also found that capping with PVP, decreases the average particle size of the three composites compared to pure ZnO and ZnNiO, whereas Dy and Ce in ZnNiO leads to increase in lattice parameter with increase in average grain size.

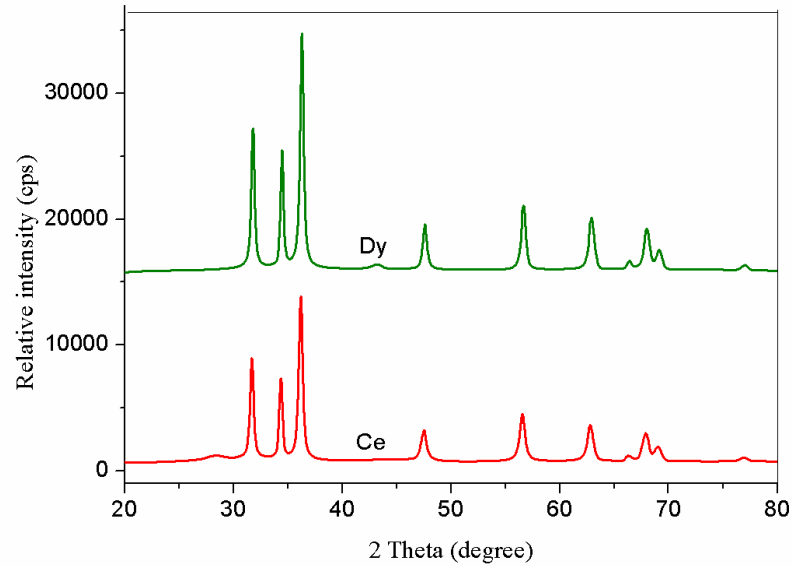


Figure 3.5: Xrd pattern of polymer capped (a) Dy:ZnNiO (b)Ce: ZnNiO nanocomposite

3.3 Calculation of nearest-neighbour distances

The wurtzite structure with hexagonal unit cell has two lattice parameters a and c in the ratio $c/a = 1.663$ (for an ideal wurtzite structure) The structure is composed of two interpenetrating hexagonal close -packed sub-lattices, each of which consists of one type of atom displaced with respect to each other along the three fold c -axis by the amount of $u = 0.375$ (for an ideal wurtzite structure) in fractional co-ordinates. In addition to composition, the lattice parameter can be affected by free charge, impurities, stress and temperature. The nearest neighbour distances ($b'_1, b'_2, \text{ and } b'_3$) are determined by the relation [6].

$$u = \left[\frac{a^2}{3c^2} \right] + \frac{1}{4} \quad (3.1)$$

The nearest neighbour bond lengths along the c-direction (b) and off c-direction as (b₁) can be calculated using

$$b = cu \quad \text{and} \quad b_1 = \sqrt{\left[\left(\frac{1}{3}\right)a^2 + \left(\frac{1}{2}-u\right)^2 c^2\right]} \quad (3.2)$$

Second nearest neighbour distances are

$$b'_1 = c(1-u), \quad b'_2 = \sqrt{a^2 + (uc)^2}, \quad b'_3 = \sqrt{4/3(a^2) + c^2\left(\frac{1}{2}-u\right)^2} \quad (3.3)$$

The calculated values are given in table 3.2. The nearest neighbour distances along c-axis and off c-axis are found to be the same. There is a strong correlation between the atomic factor ratio and 'u' parameter. The c/a ratio decreases with increasing 'u'.

Compound	Crystallite size (nm)	Lattice parameter (Å) (±0.01)		Density(g/cm ³)	Atomic factor
		A	c		c/a
ZnNiO	40.2	3.258	5.208	5.621	1.5985
ZnNiO/PVP	27.5	3.247	5.197	5.689	1.6005
Al:ZnNiO	19.7	3.236	5.180	5.747	1.6007
Pd:ZnNiO	33.1	3.241	5.192	5.721	1.6019
Cu:ZnNiO	32.2	3.245	5.194	5.732	1.6006
Dy:ZnNiO	39.8	3.240	5.199	5.692	1.6046
Ce:ZnNiO	32.6	3.256	5.204	5.644	1.5982

Table 3.1: Calculated grain size, lattice parameters and density of the samples

Compound	u parameter	Bond length (Å)	Bond length (Å)			
		b	b_1	b'_1	b'_2	b'_3
ZnNiO	0.3804	1.9842	1.9842	3.238	3.811	3.812
ZnNiO/PVP	0.3801	1.9767	1.9781	3.228	3.805	3.979
Al:ZnNiO	0.3800	1.9684	1.9684	3.211	3.788	3.768
Pd:ZnNiO	0.3798	1.9713	1.9714	3.220	3.792	3.788
Cu:ZnNiO	0.3801	1.9732	1.9741	3.221	3.797	3.798
Dy:ZnNiO	0.3794	1.9745	1.9745	3.224	3.799	3.799
Ce:ZnNiO	0.3804	1.9801	1.9805	3.236	3.809	3.810

Table 3.2: Calculated u parameter, bond lengths of the samples

3.4 FESEM Analysis and EDS spectra

The morphology and chemical composition of the samples were characterized and analyzed by Field emission Scanning Electron Microscopy, FESEM (JEOL JSM-5600LV) and Energy Dispersive X-ray Spectrometer (EDS, JEOL JED-220), which was attached to the SEM instrument. Fig. 3.6 (a) shows the representative scanning electron microscopy of the uncapped ZnNiO nanocomposite. From the SEM image, got flakes like structure for uncapped ZnNiO but after passivation, morphology of the ZnNiO nanocomposite changes to one dimensional structure like nanowires [Fig.3.7 (a)]. This change may be occurred due to the presence of poly vinylpyrrolidone (PVP). Researchers showed that PVP could control ZnO crystallization and morphology [7-10]. Capped ZnNiO was apt to grow into one-dimensional nanomaterials because PVP preferred to physically adsorb on a specific crystallographic plane of ZnNiO, which passivated this plane and facilitated the crystal growth along the c-axis.

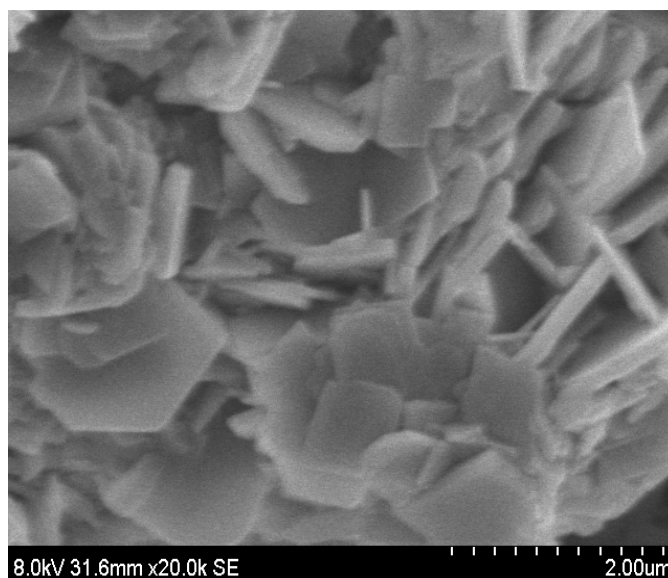


Figure 3.6: (a) SEM image of uncapped ZnNiO nanocomposite

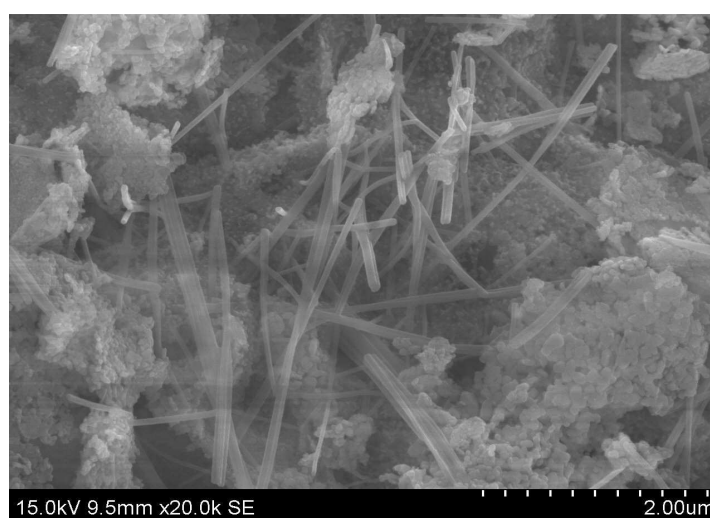


Figure 3.7: (a) SEM image of capped ZnNiO nanocomposite

Fig 3.8 (a, b, c & d) show the representative scanning electron microscopy images of Al:ZnNiO nanowires grown on polymer matrix in different scale bar. The SEM images corroborated the one dimensional shape. These results also confirmed the possibility of growing particles in one dimension with surface passivation by PVP. SEM images of Pd: ZnNiO in different scale bar are also shown in fig 3.9 (a & b). It is seen that the PVP has augmented preferential growth of the nuclides into

hexagonal geometry in the case of palladium doped sample. J. Zhang et.al, mentioned that PVP could manage control over the crystallization and influence the morphology of the nanostructures [11]. Cu: ZnNiO nanocomposite also shows one dimensional nature, shown in Fig 3.10 (a). Dy: ZnNiO and Ce:ZnNiO nanocomposites [Fig. 3.11 (a) and Fig.3.12 (a)] are also grown in one dimensional structure with the effect of capping agent. EDS spectra of all the composites are shown in figures

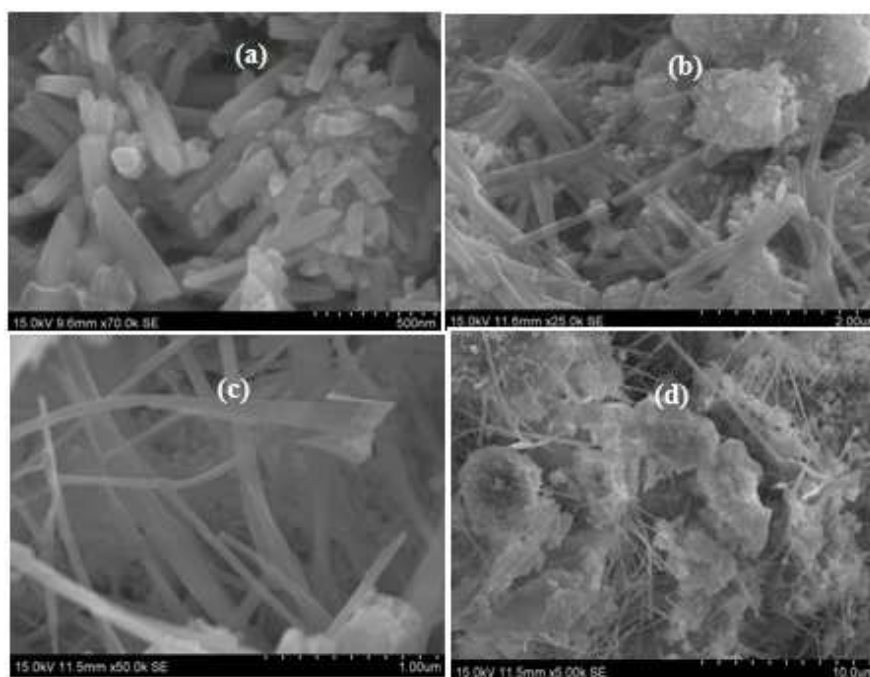


Figure 3.8: (a, b, c & d) SEM image of capped Al:ZnNiO nanocomposite with different scale bar

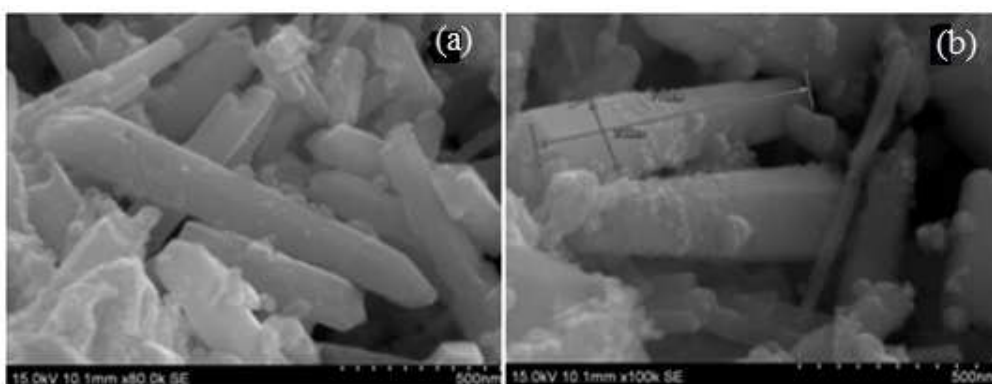


Figure 3.9: (a, b) SEM image of capped Pd:ZnNiO nanocomposite with different scale bars

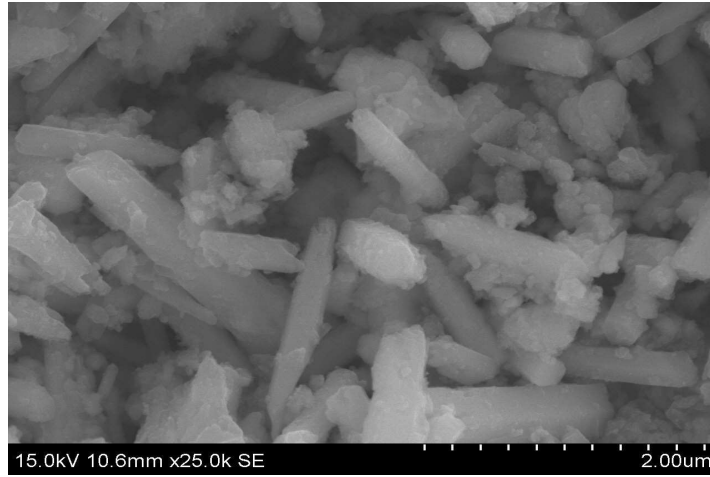


Figure 3.10: (a) SEM image of capped Cu:ZnNiO nanocomposites

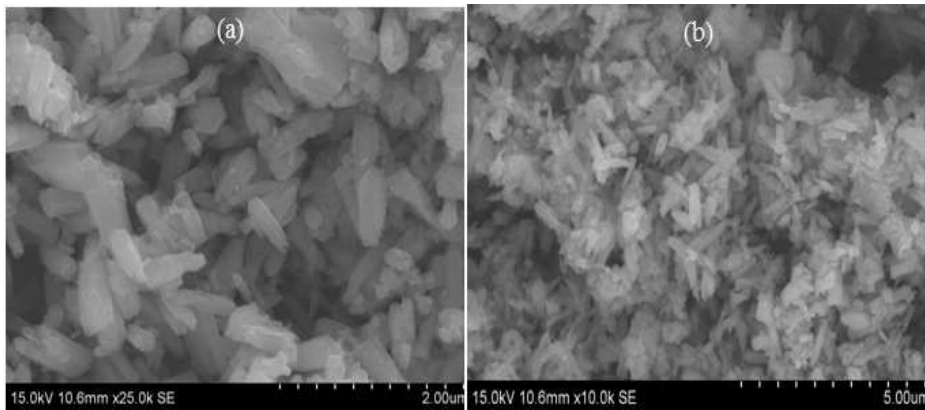


Figure 3.11: SEM image of capped Dy: ZnNiO nanocomposite at different scale bars

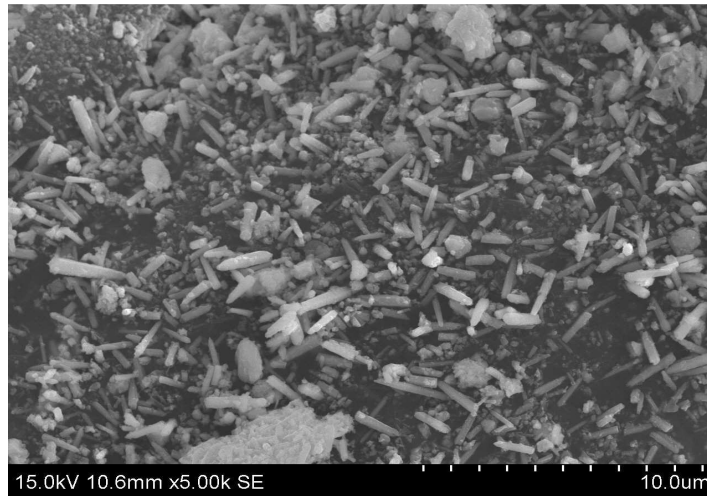
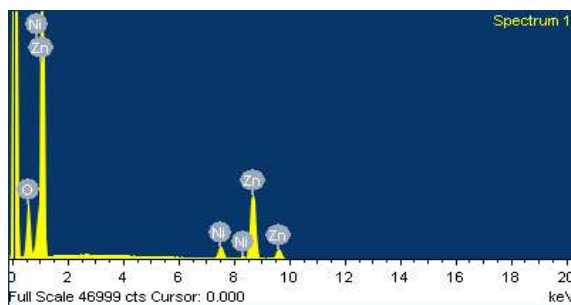


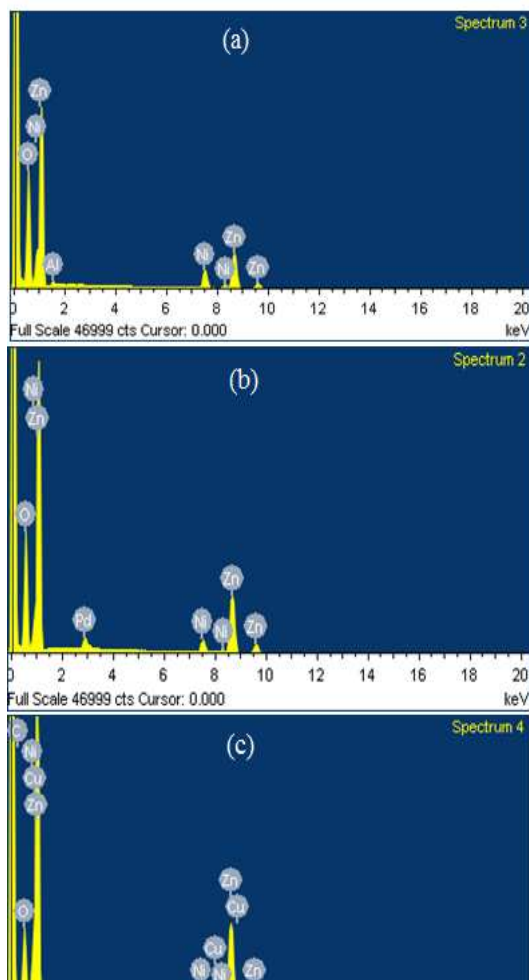
Figure 3.12: SEM image of capped Ce:ZnNiO nanocomposite

Corresponding EDS spectra of capped ZnNiO, Al:ZnNiO, Pd:ZnNiO, Cu:ZnNiO, Dy:ZnNiO and Ce:ZnNiO nanocomposites are shown in [Fig: 3.13, Fig: 3.14 (a), (b) & (c) and Fig: 3.15 (a) & (b)], confirmed the presence of metals (Zn, Ni, Al, Pd, Cu, Dy & Ce) and C, O contained in the nanocomposites.



Element	Weight %	Atomic %
O K	23.73	55.78
Ni K	5.44	3.48
Zn K	70.83	40.74

Figure 3.13: EDS spectra of ZnNiO nanocomposites

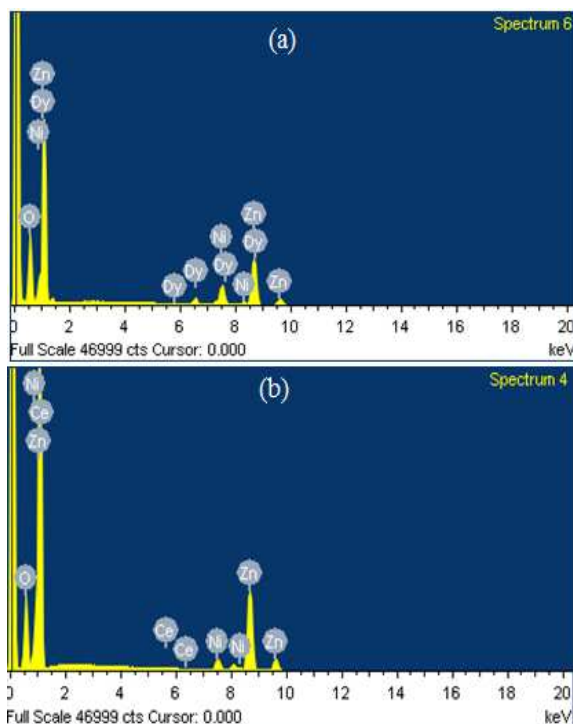


Element	Weight %	Atomic %
O K	45.64	76.53
Al K	1.15	1.15
Ni K	10.57	4.83
Zn K	42.63	17.50

Element	Weight %	Atomic %
O K	40.02	73.38
Ni K	5.18	2.59
Zn K	51.57	23.14
Pd L	3.23	0.89

Element	Weight %	Atomic %
O K	25.39	57.98
Ni K	4.23	2.63
Cu K	3.73	2.14
Zn K	66.65	37.25

Figure 3.14: EDS spectra of (a) AL:ZnNiO(b) Pd:ZnNiO (c) Cu:ZnNiO nanocomposites



Element	Weight %	Atomic %
O K	30.71	65.41
Ni K	10.82	6.28
Zn K	51.51	26.85
Dy L	6.96	1.46

Element	Weight %	Atomic %
O K	26.50	59.43
Ni K	4.18	2.55
Zn K	69.24	38.00
Ce L	0.08	0.02

Figure 3.15: EDS spectra of (a) Dy:ZnNiO (b) Ce::ZnNiO nanocomposites

3.4 Conclusion

Surface passivation effects on ZnNiO nanocomposite do not damage the hexagonal structure of ZnNiO nanocomposite. X-ray diffraction studies of the uncapped and capped metaloxide nanocomposites showed excellent crystallinity and all the samples indexed to hexagonal structure. Crystallite size of the samples decreased due to the effect of surface passivation because it prevents the particles from agglomeration. Morphological analysis supports the ability of polyvinyl pyrrolidone to grow in one dimensional structure. The polymer, PVP could prefer to physically adsorb on a specific crystallographic plane of ZnO, which passivated this plane and facilitate the crystal growth only along the c-axis. The EDS spectra of all the samples reveals the presence of metals in the composites.

References

- [1] D. Kriegner, S. Assali, A. Belabbes, T. Etzelstorfer, V. Holy, T. Schulli, F. Bechstedt, E. P. A. M. Bakkers, G. Bauer, J. Stangl, *Phy. Rev. B.* 88 (2013) 115315.
- [2] C. Klingshirn, B. Meyer, A. Wang, A. Hoffmann, J. Geurt's, Zinc oxide :From Fundamental properties towards novel applications, vol.120 (springer series in material science 2010).
- [3] J. Zhang, H. Liu, Z. Wang, N. Ming, Z. Li, A. S. Biris, *Adv.Funct.Mater.* 17 (2007) 3897.
- [4] L. E. Greene, M. Law, D. H. Tan, M. Montano, J. Goldberger, G. Somarjai, P. Yang, *Nano Lett.* 5 (2005) 1231.
- [5] B. Zhang, X. T. Zhang, He. C. Gong, Z. Shen Wu, S. M. Zhou, Z. L. Du, *Phys. Lett. A.* 372 (2008) 2300.
- [6] O. Ambacher, J. Majeski, C. Miskys, A. Link, M. Hermann, M. Eickhoff, M. Sturtzmann, F. Bernardini, V. Fiorentini, B. Schaff, V. Tilak, L. F. Eastman, *J. of Physics: Condensed mater.* 14 (2002) 3399.
- [7] K. Shijina, U. Megha, George Varghese, *J. Lumin.* 145 (2014) 219.
- [8] K. Shijina, George Varghese, Megha U, *J. Lumin.* 175 (2016) 207.
- [9] K. Shijina, George Varghese, U. Megha, *Mater. Sci. Engineer. B* 199 (2015) 125.
- [10] K. Shijina, George Varghese, U. Megha, *Mater. Sci. Semiconductor processing* 34 (2015) 21.
- [11] J. Zhang, H. Liu, Z. Wang, N. Ming, Z. Li, A. S. Biris, *Adv. Funct. Mater.* 17 (2007) 3897-3905.

Chapter 4

Surface passivation effects on adsorption properties

4.1 Introduction

In the last decades mesoporous ZnO material has been attracting more attention because of its great potential application in electronics, optics, catalysis, solar energy conversion and other optoelectronic devices, due to the special characteristics of the large specific surface area, high porosity and narrow pore size distribution. ZnO with various low dimensional structures including nanowire, nanoring, nanocages and nanoflowers have wide applications in nanosieve filters, catalyst supports, masks and gas sensors [1-3]. Among these nanostructures, porous ZnO has a high surface to volume ratio as well as excellent inherent properties. Researchers prepared mesoporous thin films by sol-gel method using poly (ethylene glycol) (PEG) as the capping agent. Considerable amount of papers have been reported on the synthesis of nanoporous ZnO structures with various methods such as wet-chemical method [4], electrochemical deposition [5], RF sputtering [6], metal-organic chemical vapour deposition (MOCVD) [7] and thermal transition [8,9]. Here my great interest has focused on the synthesis of mesoporous ZnNiO and ZnNiO based nanocomposites.

4.2 BET Isotherm

BET (Brunauer-Emmett-Teller) Nitrogen adsorption-desorption isotherms are used for the determination of specific surface area, pore size distribution, total pore area and total pore volume of the mesoporous and macroporous materials. The specific surface area of the uncapped and capped samples were determined from nitrogen adsorption /desorption isotherms at 77 K using a Micrometrics ASAP 2020 Surface Area and Porosity Analyzer. The powder samples were degassed at 150⁰ C in a vacuum below 10⁻³ Torr for 16 h prior to the measurements.

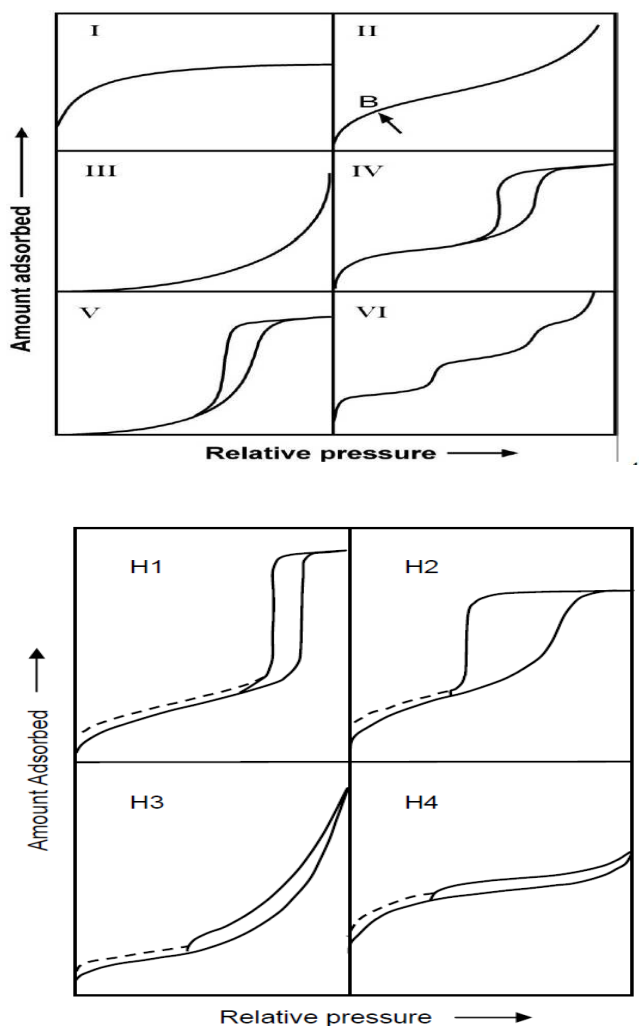


Figure 4.1: Schematic diagram of BET isotherms

Four types of isotherms out of the six proposed by IUPAC are commonly encountered [10]: I, II, IV, and VI. Similarly, the hysteresis loops, corresponding to mesoporous systems have been classified in terms of their forms into four categories: H1, H2, H3, and H4 [Fig 4.1]. N₂ adsorption-desorption isotherms of the uncapped ZnNiO is shown in Fig 4.2. This isotherm reveals microporosity, moreover it contains less number of mesoporous particles. This microporosity was completely changed when this ZnNiO nanocomposite capped with PVP. According to the Brunauer–Deming–Deming–Teller (BDDT) classification, all of the capped (ZnNiO, Al:ZnNiO, Cu:ZnNiO, Pd:ZnNiO, Dy:ZnNiO and Ce:ZnNiO) isotherms are of type IV with a type H3 hysteresis loop, suggesting the existence of abundant mesoporous structures. Isotherms of all the capped samples are shown in Fig [4.2, 4.3, 4.4, 4.5, 4.6 and 4.7].

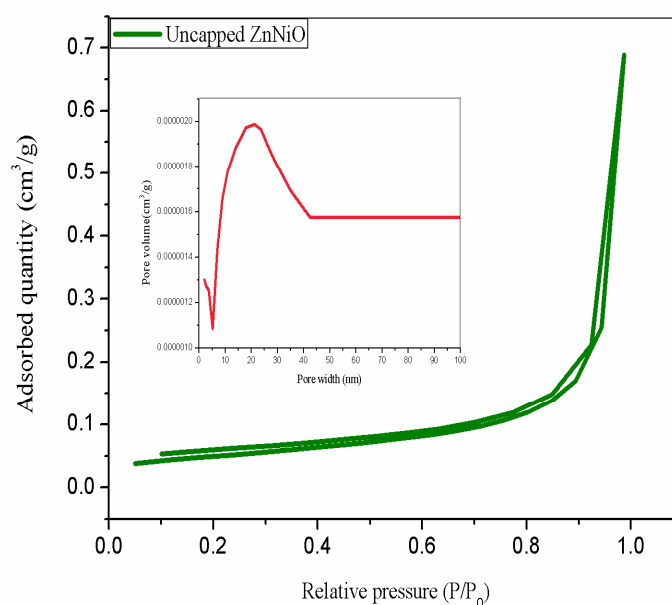


Figure 4.2: Adsorption –Desorption isotherm plots of uncapped ZnNiO.

Inset figure shows PSD of uncapped ZnNiO nanocomposite

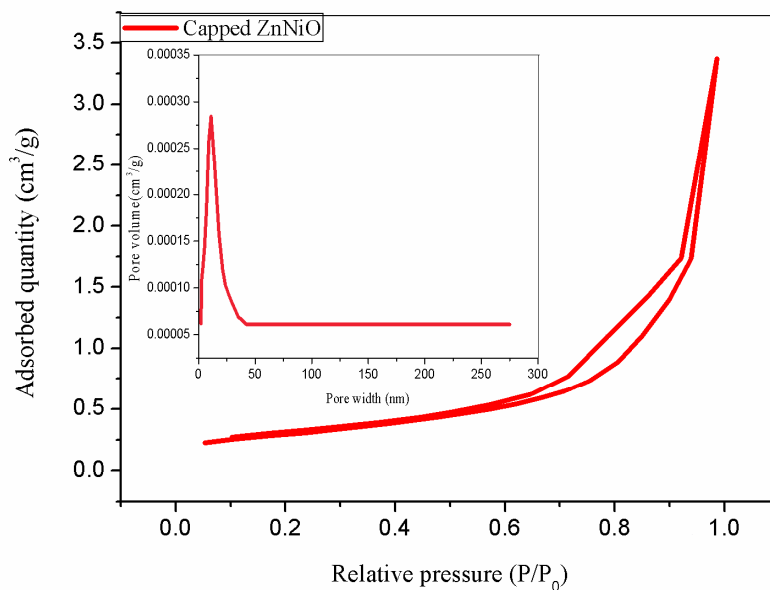


Figure 4.3: Adsorption –Desorption isotherm plots of capped ZnNiO.
Inset figure shows PSD of capped ZnNiO nanocomposite

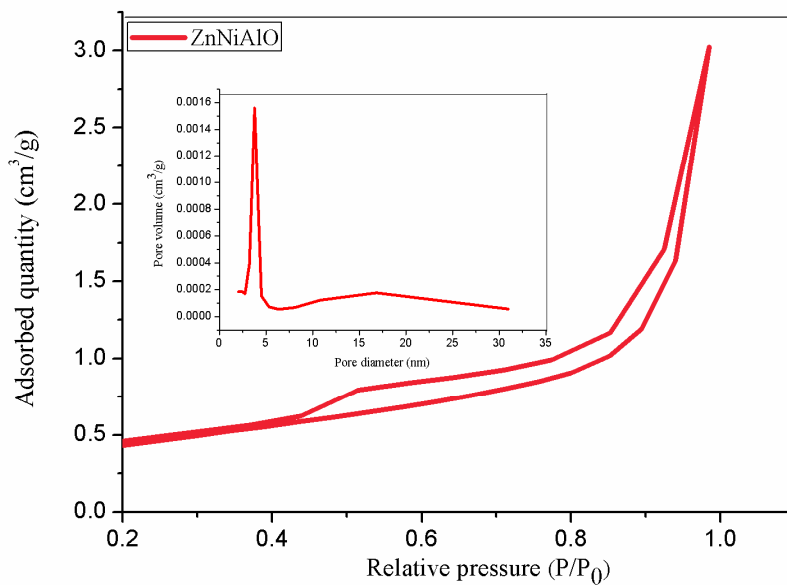


Figure 4.4: Adsorption –Desorption isotherm plots of Al: ZnNiO.
Inset figure shows PSD of Al: ZnNiO nanocomposite

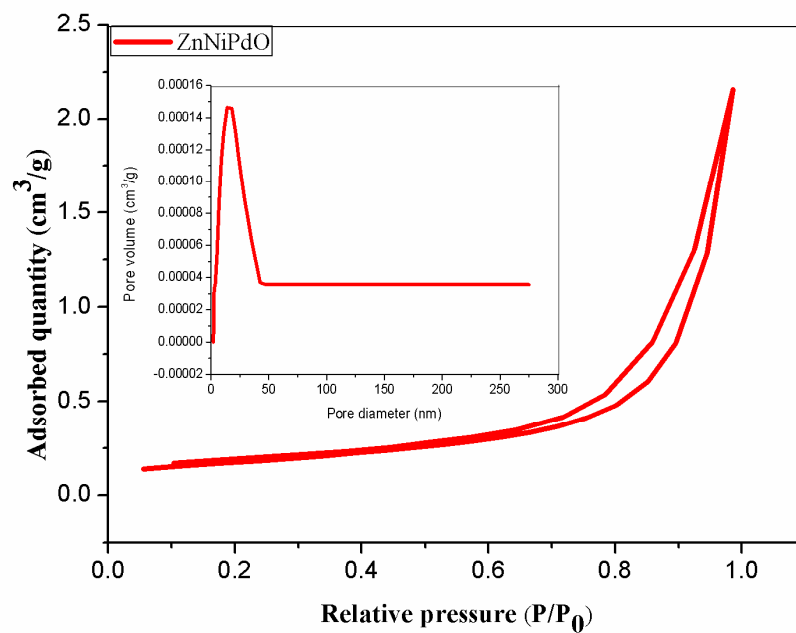


Figure 4.5: Adsorption –Desorption isotherm plots of Cu:ZnNiO.
Inset figure shows PSD of Cu: ZnNiO nanocomposite

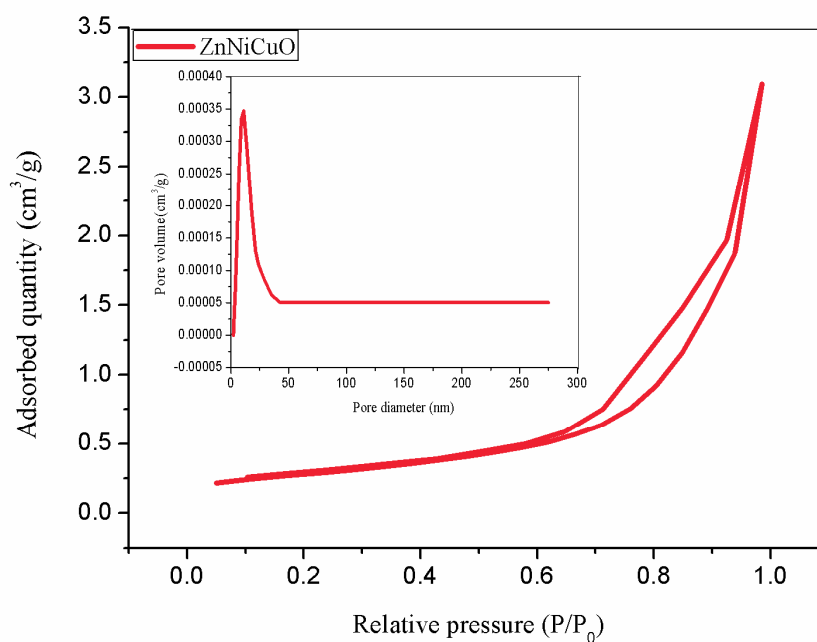


Figure 4.6: Adsorption –Desorption isotherm plots of Pd:ZnNiO.
Inset figure shows PSD of Pd: ZnNiO nanocomposite

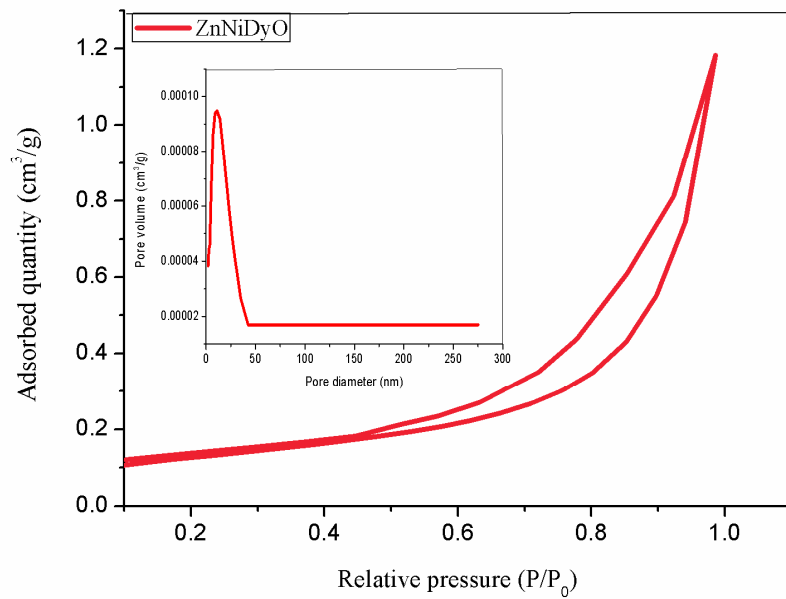


Figure 4.7: Adsorption –Desorption isotherm plots of Dy:ZnNiO. Inset figure shows PSD of Dy: ZnNiO nanocomposites

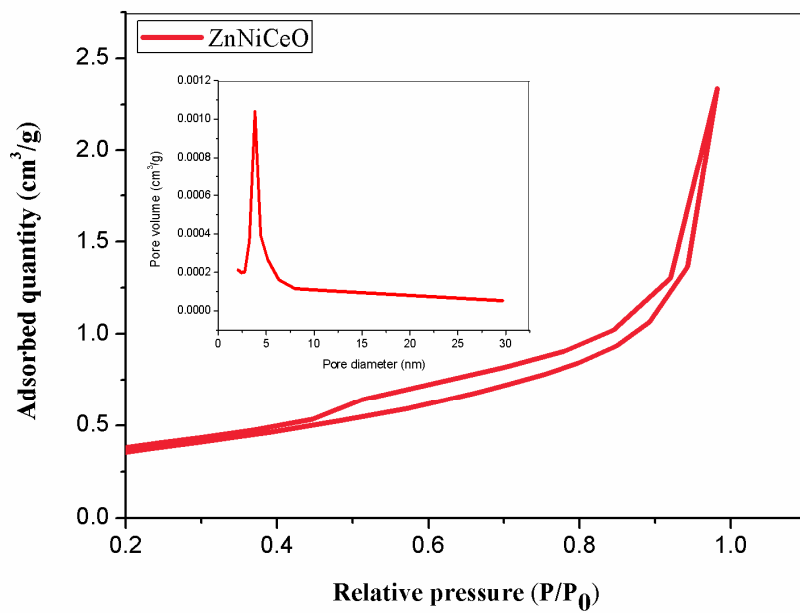


Figure 4.8: Adsorption –Desorption isotherm plots of Ce:ZnNiO. Inset figure shows PSD of Ce: ZnNiO nanocomposites

4.3 Specific surface area determination

The Brunauer-Emmett-Teller (BET) method is the most widely used procedure for the determination of the surface area of solid materials and involves the use of BET equation

$$\frac{1}{Q \left[\left(\frac{p_0}{p} \right) - 1 \right]} = \frac{1}{W_m c} + \frac{c-1}{W_m c} \left(\frac{p}{p_0} \right) \quad (4.1)$$

Q is the weight of the gas adsorbed at a relative pressure and W_m is the weight of the adsorbate constituting a monolayer of surface coverage.

The BET equation requires a linear plot of $\frac{1}{Q \left[\left(\frac{p_0}{p} \right) - 1 \right]}$ versus $\frac{p}{p_0}$,

which for most solids using nitrogen as adsorbate is restricted to a limited region in the P/P_0 range of 0.05 to 0.35. W_m can be obtained from slope and intercept of the BET plot.

Specific surface area of the sample can be expressed as $S = \frac{S_t}{w}$ where

$S_t = W_m N A_{cs} / M$, A_{cs} is the molecular cross section of the adsorbate molecule (16.2 \AA^2 for N_2 at 77 K), M is the molecular weight of the adsorbate gas and N is the Avogadro number.

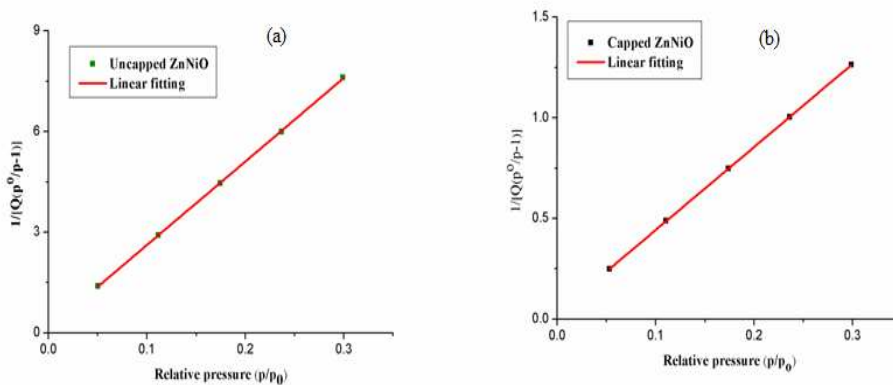


Figure 4.9: BET surface area plots of (a) uncapped ZnNiO (b) capped ZnNiO nanocomposites

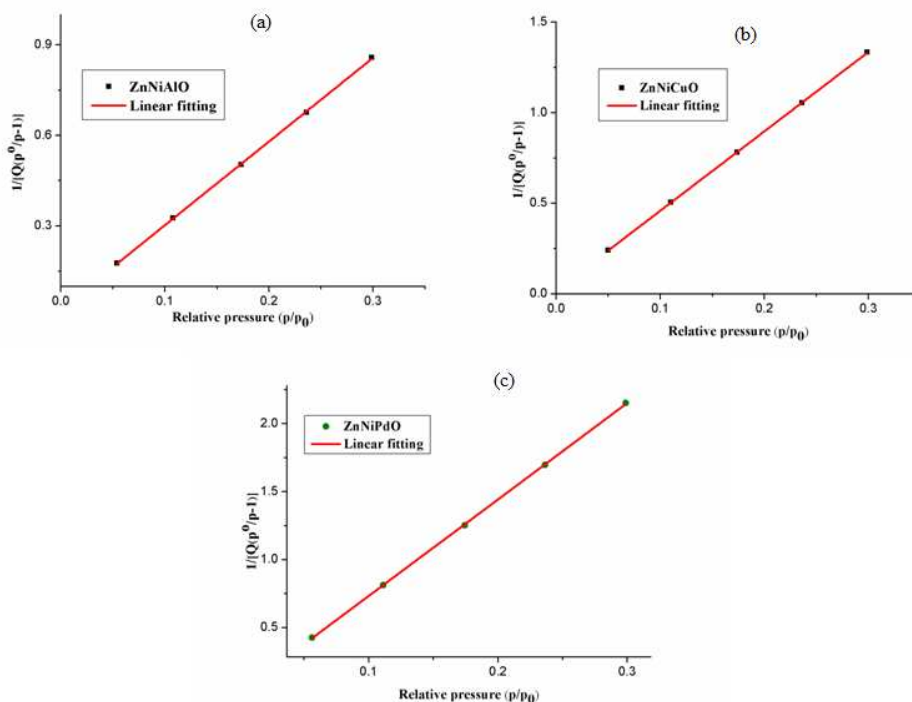


Figure 4.10: BET surface area plots of capped (a) Al:ZnNiO (b) Pd:ZnNiO (c) Cu:ZnNiO nanocomposites

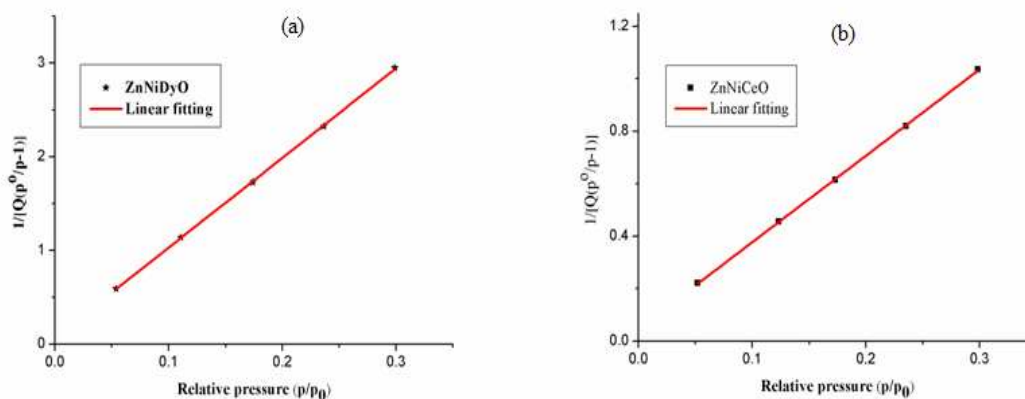


Figure 4.11: BET surface area plots of capped (a) Dy:ZnNiO (b) Ce:ZnNiO nanocomposites

BET plot of all the capped and uncapped samples are shown in figures [4.9 (a, b) 4.10 (a, b & c), 4.11 (a, b)] and surface area calculated from this plot is tabulated in table 4.1. Determination of surface areas from the BET theory is a straightforward application of the BET equation. This results shows that all the capped samples have high surface area compared to uncapped samples due to the effect of poly vinyl pyrrolidone (PVP). PVP protects the particles from agglomeration and formed small

size particles compared to uncapped ones. Surface area of the particles increased when size decreased in the nanometer range.

Sample	Surface area (m ² /g) BET (S)	Average pore size (nm)		Pore volume (cm ³ /g)
		BET	BJH	
ZnNiO	3.8981 ± 0.022	24.51	25.67	0.0237
ZnNiO/PVP	23.4802 ± 0.043	19.91	18.48	0.1171
Al:ZnNiO	34.8653 ± 0.240	12.02	12.74	0.0102
Cu:ZnNiO	22.1434 ± 0.068	19.38	17.27	0.0107
Pd:ZnNiO	13.7017 ± 0.072	21.83	20.92	0.0745
Dy:ZnNiO	10.1071 ± 0.064	16.2	16.09	0.0408
Ce:ZnNiO	29.1680 ± 0.180	11.09	11.13	0.0799

Table 4.1: Calculated surface area, average pore size from BET and BJH method and pore volume of the samples

4.4 Determination of total pore volume and average pore radius

The total pore volume is derived from the amount of vapor adsorbed at a relative pressure close to unity ($P/P_0 \approx 1$), by assuming that the pores are then filled with liquid adsorbate. The volume of nitrogen adsorbed (V_{ads}) can be converted to the volume of liquid nitrogen (V_{liq}) contained in the pores using this equation

$$V_{liq} = P_a V_{ads} V_m / RT \quad (4.3)$$

V_m is the molar volume of the adsorbate. The average pore size can be estimated from the pore volume.

$$r_p = 2V_{liq} / S \quad (4.4)$$

S is the BET surface area of the sample. Calculated pore size and pore volume of the samples listed in table 4.1.

4.5 Pore size distribution (PSD)

Porosity is defined as the ratio of the volume of pores and voids to the volume occupied by the solid and powder porosity is the ratio of volume of voids plus that of open pores to the total volume occupied by the powder. If cylindrical pore geometry can be assumed, the average pore diameter of porous materials can be calculated by the following relation

$$D = \frac{4V}{S_{BET} - S_{ext}} \quad (4.2)$$

The total surface area S_{total} can be calculated either from the BET-method or from t-plot [11-12]]. The total pore volume, V , is derived from the amount of vapour adsorbed at p/p_0 close to one. The pore size distribution (PSD) is the distribution of pore volume with respect to pore size. The pore-size distributions were calculated from the data of the desorption branch of the isotherm using the Barret-Joyner-Halenda (BJH) method. BJH pore size distribution of uncapped and all capped samples shown in the inset plot of Fig [4.5, 4.6, 4.7, 4.8, 4.9, 4.10 & 4.11]. The average pore size and pore volume of the samples are shown in table 4.1.

4.5.1 t-Plot

Microporosity includes the specific surface area S_{BET} , external surface area and pore volume. These parameters of the samples were determined by using the t-plot. The procedure is same as BET surface area measurement, but it extends the pressure range to higher pressures to permit calculation of the external surface area, that is, non-microporous part of the material. The t-Plot method is attributed to Lippens and De Boer [13-14]. They proposed the plotting of the nitrogen adsorbed volume (v) at different P/P_0 values as a function of the layer thickness (t). The resulting curve is compared with the experimental isotherm in the form of t-plot. The slope of the t-plot, V/t , is equal to the external area. The model allows separating the micropores from meso, macro and outside surface. This separation is illustrated by the equation [15].

$$V(P/P_0) = V(\text{micro}) + k S_{\text{ext}} (P/P_0) \quad (4.2)$$

The layer thickness t values are calculated as a function of de Boer equation.

$$t = [13.99 / (0.034 - \log P/P_0)]^{1/2} \quad (4.3)$$

t -plot of the samples are shown in figures [4.12(a, & b), 4.13(a, b & c), 4.14(a & b)] and the surface area calculated from t -plot is shown in table 4.2. Micropore area is not observed in Al:ZnNiO and Ce:ZnNiO nanocomposites.

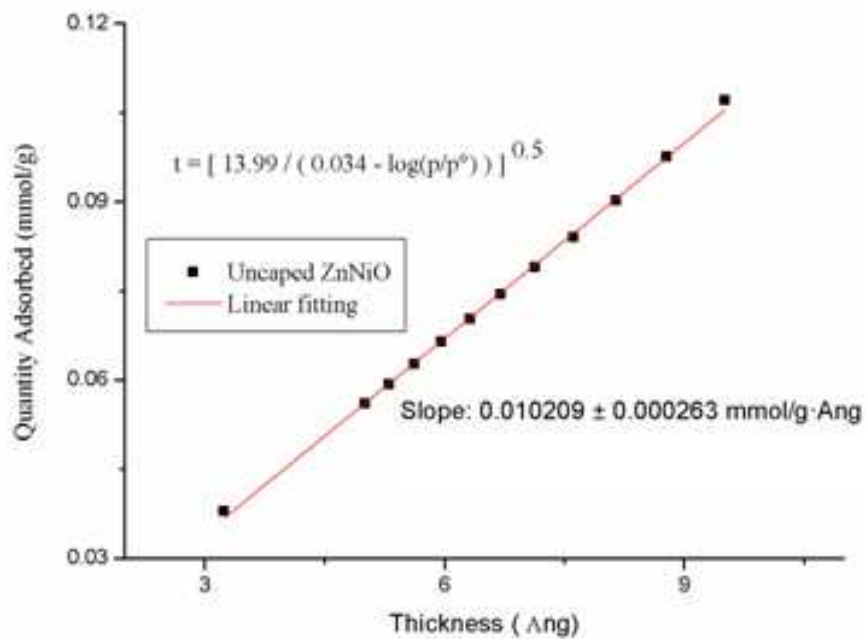


Figure 4.12: t -Plot of (a) uncapped ZnNiO nanocomposite

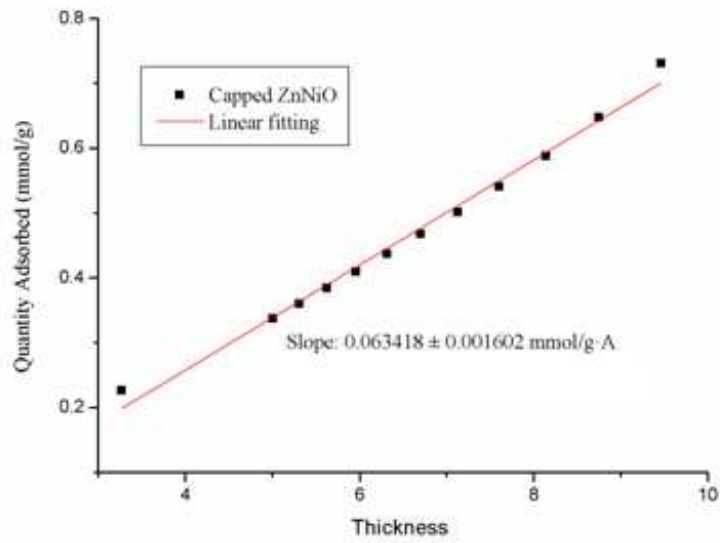


Figure 4.12: (b) t-Plot of capped ZnNiO nanocomposite

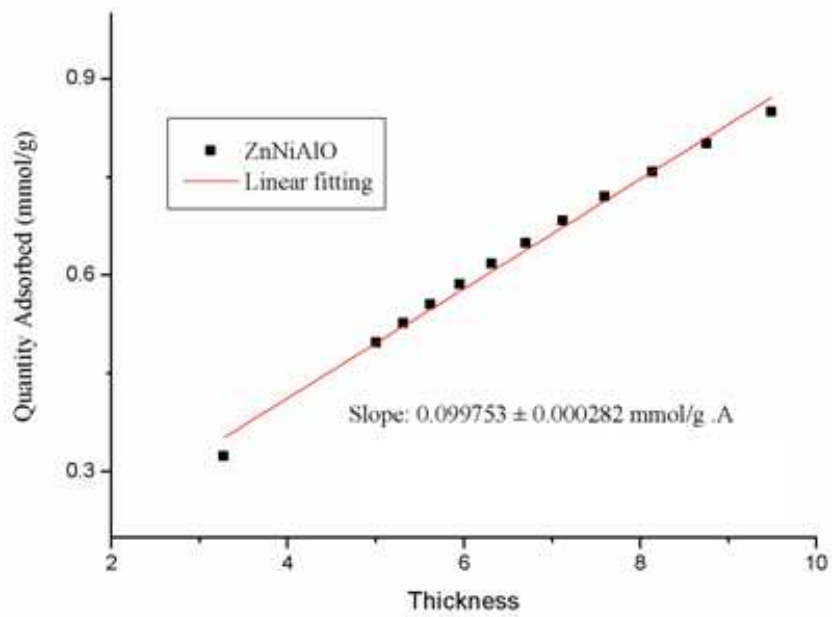


Figure 4.13: (a) t-Plot of capped Al:ZnNiO nanocomposites

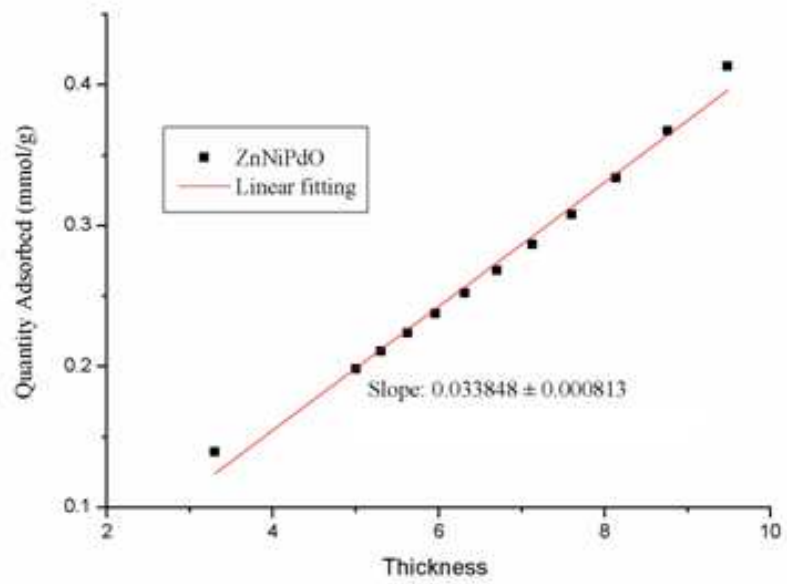


Figure 4.13: (b) t-Plot of capped (b) Pd:ZnNiO nanocomposites

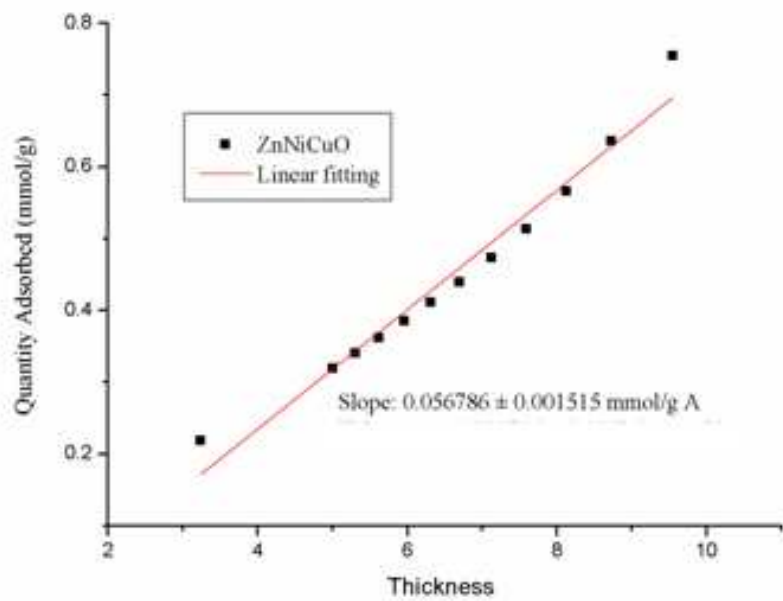


Figure 4.13: (c) t-Plot of capped Cu:ZnNiO nanocomposites

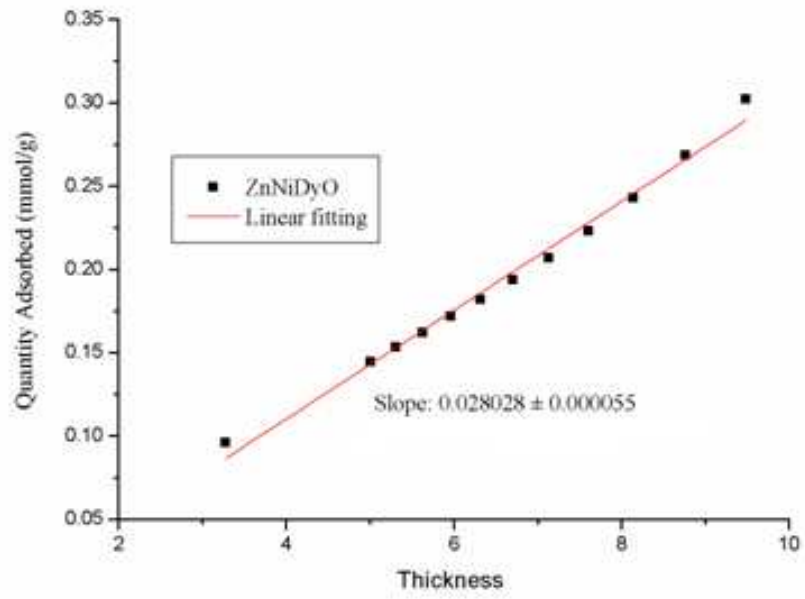


Figure 4.14: (a) t-Plot of capped Dy:ZnNiO nanocomposites

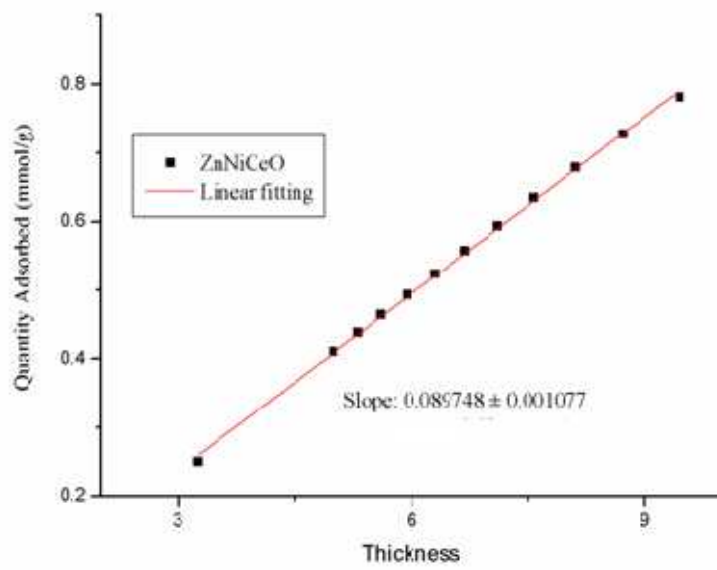


Figure 4.14: (b) t-Plot of capped Ce:ZnNiO nanocomposites

Sample	Micropore area (m ² /g)	External area (m ² /g)	Micropore volume (cm ³ /g)
ZnNiO	0.3585	3.539	0.00016
ZnNiO/PVP	1.4929	21.987	0.00055
Al:ZnNiO	No micropore	34.584	-----
Cu:ZnNiO	2.4555	19.687	0.00010
Pd:ZnNiO	1.9667	11.735	0.00092
Dy:ZnNiO	0.3899	9.717	0.00014
Ce:ZnNiO	No micropore	31.115	-----

Table 4.2: Calculated micropore area, external area and micropore volume of the samples from t-plot

4.6 Conclusion

The specific surface areas of the uncapped and capped samples were determined from nitrogen adsorption /desorption isotherms at 77 K using a Micrometrics ASAP 2020 Surface Area and Porosity Analyzer. The isotherm hysteresis loop of the uncapped sample shows that it is not mesoporous but all capped samples are mesoporous with low pore size. Pore size changed with different catalysts. Surface passivated Al:ZnNiO and Ce:ZnNiO are mostly mesopores with zero micropore area. These results focus that, these capped samples are good catalyst with mesoporous nature and high surface area.

References

- [1] C. V. Cojocaru, C. Harnagea, F. Rosei, A. Pignolet, *Appl. Phys. Lett.* 8 (2005) 183107.
- [2] X. Wang, C. Lao, E. Graugnard, C.J. Summers, Z.L. Wang, *Nano Lett.* 5 (2005) 1784.
- [3] G. Sberveglieri, S. Groppelli, P. Nelli, A. Camanzi, *J. Mater. Sci. Lett.* 10 (1991) 602.
- [4] Z. H. Dai, K. Liu, Y.W. Tang, X. D. Yang, J. C. Bao, J. Shen, *J. Mater. Chem.* 18 (2008) 1919.
- [5] H. W. Yan, Y. L. Yang, Z. P. Fu, B. F. Yang, L.S. Xia, S.Q. Fu, F.Q. Li, *Electrochem. Commun.* 7 (2005) 1117.
- [6] G. Q. Ding, W. Z. Shen, M. J. Zheng, D. H. Fan, *Appl. Phys. Lett.* 88 (2006) 103106.
- [7] J. L. Yang, S. J. An, W. I. Park, G. C. Yi, W. Choi, *Adv. Mater.* 16 (2004)1661.
- [8] J. B. Shen, H. Z. Zhuang, D. X. Wang, C. S. Xue, H. Liu, *Cryst. Growth Des.* 9 (2009) 2187.
- [9] W. Q. Peng, G. W. Cong, S. C. Qu, Z. G. Wang, *Nanotechnology*16 (2005) 1469.
- [10] D. Uzio, Textural Characterization of Catalysts, in: Lynch J. (Editor), Physico-Chemical Analysis of Industrial Catalysts, Edition Technip, Paris, 2001, 5.
- [11] J. H. De Boer, B. C. Lippens, B. G. Linsen, J. C. P. Broekhoff, A. van den Heuvel, T. J. Osinga, *J. Colloid Interface Sci.* 21 (1966) 405.
- [12] S. J. Gregg, K. S. W. Sing, Adsorption, Surface Area and Porosity, 2nd ed., Academic Press, London, 1982.
- [13] B. C. Lippens, J. H. de Boer, *J. Catal.* 4 (1965) 319.
- [14] J. H. De Boer, B. C. Lippens, B. G. Linsen, J. C. P. Broekhoff, A. van den Heuvel, Th. J. Osinga, *J. Colloid Interface Sci.* 21(1966) 404.
- [15] I. Siminiceanu, C. Petrila, A. Pop, *Chem. Tech.*, 43 (1991) 257.
- [16] G. Jura, W. D. Harkins, *J. Amer. Chem. Soc.* 66 (1944) 1362.

Chapter 5

Capping effects on magnetic properties

5.1 Introduction

The study of magnetic nanoparticle is a subject of intensive research from the viewpoint of probing their magnetic behaviour, (size and surface effects [1-6], quantum tunnelling of magnetization [7]) and practical significance (high density magnetic recording media [8-10], giant magneto-resistive sensors [11] and ferrofluids [12-14]). The magnetic behaviour of nanoparticle has a marked dependence with decrease in particle size and the surface effects [15]. Nanoparticles with large surface to volume ratio, the surface-spin-driven arrangements may eventually modify the magnetic properties. This spin disorder is caused by lower coordination of the surface atoms, broken exchange bonds. This broken exchange bonds produce a spin-glass like state of spatially disordered (canted) spins in the surface cations with high anisotropy surface layer. The disorder manifests strongly in nanocrystalline metaloxides, where the super-exchange interaction occurs through the oxygen ions. The absence of oxygen ions from the surface leads to the broken exchange bonds that induce surface spin disorder. Thus, the contribution of surface

effects is essentially due to breaking of symmetry of the lattice that result in site specific anisotropy of unidirectional character, broken ex-change bonds, and weak exchange interactions. The result of which is that magnetization at the surface is smaller than the core. It would be expected that the magnetization vector will point along the particle anisotropy axis in the core of the particle and would gradually change the direction on approaching the surface.

Recent observations compel one to infer that the ferromagnetism obtained in semiconductors does not rely exclusively on the localized moments in magnetic ions, but can also be leading to magnetic moments generated due to the defects [16, 17]. Others proposed room temperature ferromagnetism (RTFM) to be associated with holes in the d shell due to charge transfer [18-23] from the Zn atom at the surface to the capping agent. In case of doped ZnO NCs, it is usually believed that dopant induced defects contribute to RTFM [24-26]. In spite of the considerable efforts undertaken to understand the optical and magnetic properties of the d^0 ferromagnetic materials, the detailed underlying mechanism is still not clear. Compared to the conventional diluted magnetic semiconductors, one obvious advantage of d^0 ferromagnetism is that clusters or secondary phases formed by the dopant do not contribute to magnetism [27].

5.2 Results and Discussion

M-H hysteresis loop of the polymer capped and uncapped ZnNiO are shown in fig [5.1 (a) & (b)]. From the M-H hysteresis loop, it is clear that uncapped ZnNiO with small coercivity and remanent magnetization, which is closer to the conditions of the superparamagnetic state (SPM) with some single domain (SD) or multi-domain (MD) grains. Superparamagnetic particles exhibit no remanence or coercivity. The shape of the hysteresis loop is thus extremely thin. SPM grains show a very steep initial rise in magnetization with field and then a more gradual increase to saturation. However a mixture of mostly superparamagnetic grains with some SD or MD grains has $M_r/M_s \ll 0.01$. The values of saturation magnetization (M_s), Coercivity (H_c) and Retentivity (M_r) are 0.01585 emu/g, 58.661G and 149.18×10^{-6} emu/g respectively. Here, the M_r/M_s ratio, 0.009 confirms superparamagnetic behaviour with multi domains. Loops for single domain materials are typically wider than loops for multi

domain materials. This is just a reflection of the higher coercivity and remanence in single domain materials. Polymer capped ZnNiO showed room temperature ferromagnetism with high coercivity and higher retentivity compared to uncapped samples. Calculated ratio of retentivity and magnetisation (M_r/M_s) is greater than zero. So the cause of anisotropy is intrinsic. The values of Magnetization, retentivity and coercivity of the capped and uncapped ZnNiO are shown in table 5.1

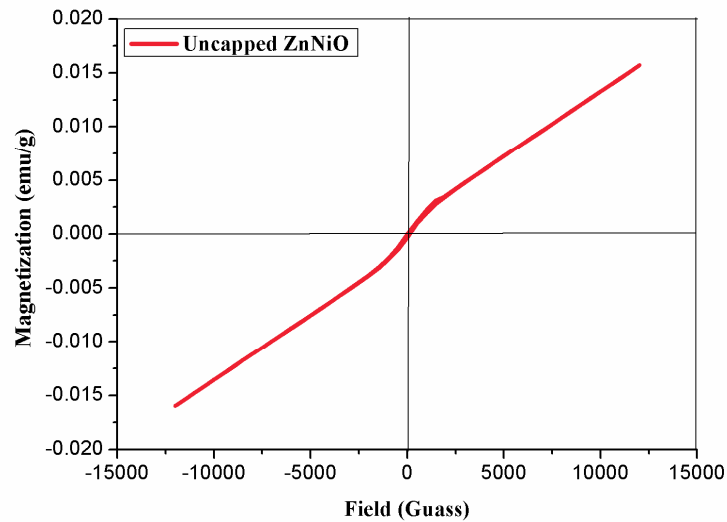


Figure 5.1: (a) Room temperature M-H Hysteresis loop of ZnNiO without capping

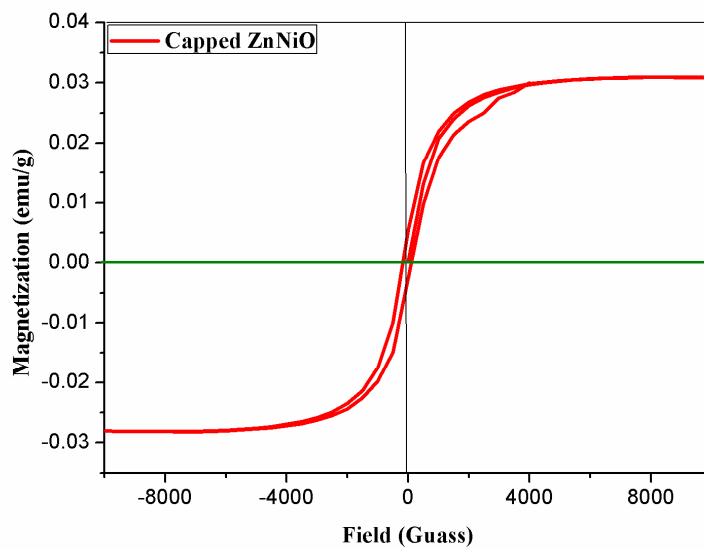


Figure 5.1: (b) Room temperature M-H Hysteresis loop of capped ZnNiO

Room temperature ferromagnetic hysteresis loop of Al:ZnNiO, Cu:ZnNiO and Pd:ZnNiO nanocomposites with polymer capping are shown in fig. 5.2 (a), (b) and (c). From the figure it may be noted that polymer capped nanocomposites exhibit room temperature ferromagnetism. The coercivity is influenced by the coupling of the particle. Ferromagnetism in dilute magnetic semiconductors is considered to originate from either the exchange interaction between the holes and electrons from the valence band and the localized d spins on the transition metal ions and the origin of ferromagnetism in ZnO nanoparticles may be related to the O^{1-} defects, since they can initiate a lattice defect or vacancy induced ordering leading to the magnetism in the system. Calculated saturation magnetization, coercivity and retentivity of the samples is shown in table 5.1.

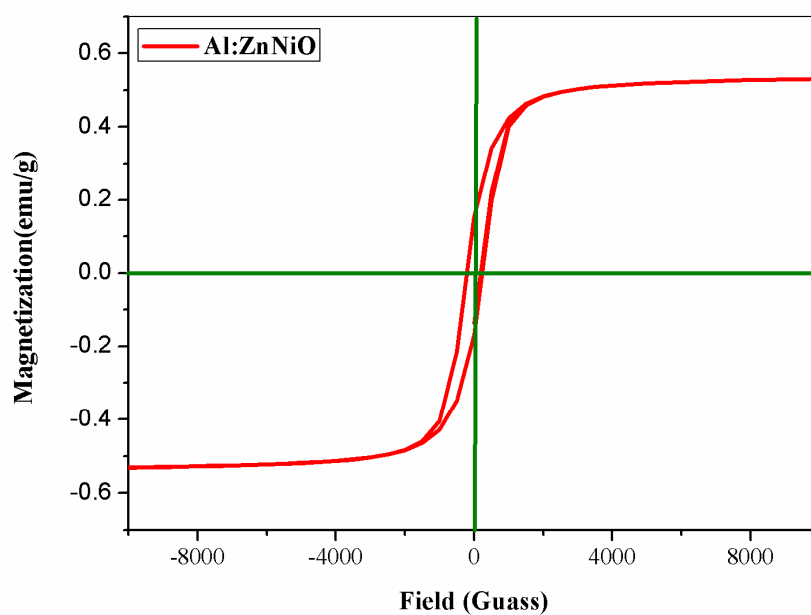


Figure 5.2: (a) Hysteresis loop of polymer capped Al:ZnNiO nanocomposites

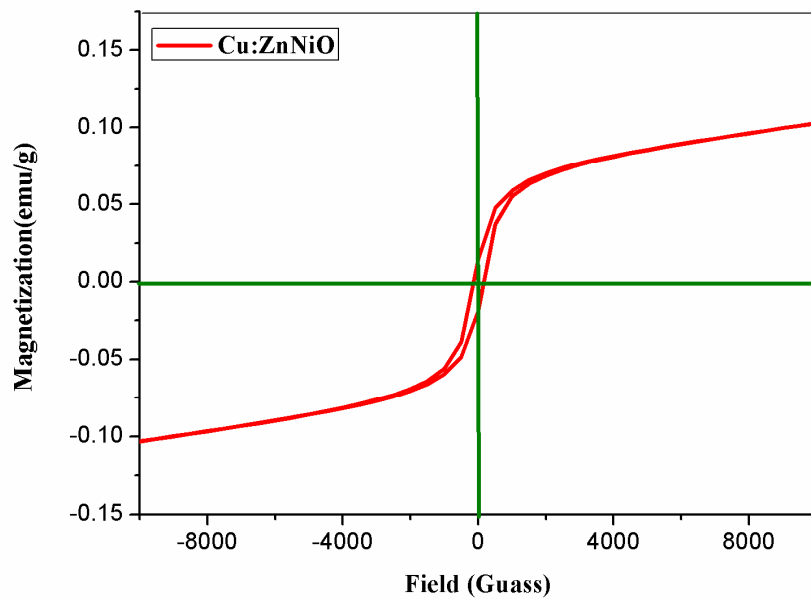


Figure 5.2: (b) Hysteresis loop of polymer capped Cu:ZnNiO nanocomposite

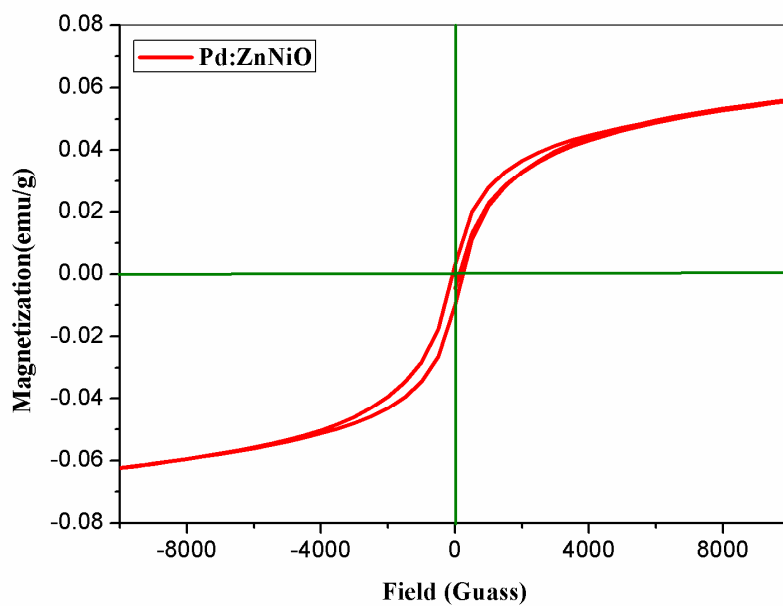


Figure 5.2: (c) Hysteresis loop of polymer capped Pd:ZnNiO nanocomposites

Room temperature hysteresis loop of surface passivated and rare-earth metals (Dy, Ce) doped ZnNiO nanocomposites [Dy:ZnNiO and Ce:ZnNiO] are shown in fig 5.3 (a) and (b). These samples show ferromagnetic behaviour with high magnetization, coercivity and retentivity than undoped and passivated ZnNiO. This suggests that

Ce:ZnNiO, Dy:ZnNiO nanocomposites are good material for ferroelectric applications. The shape of the hysteresis loop confirms that this material is a good ferromagnetic material with multi-domains [narrow loop].

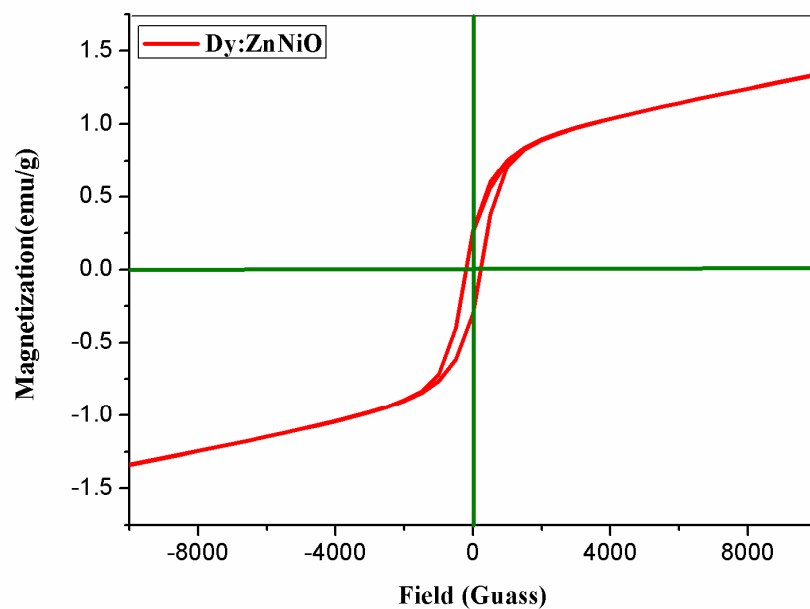


Figure 5.3: (a) Hysteresis loop of polymer capped Dy:ZnNiO nanocomposites

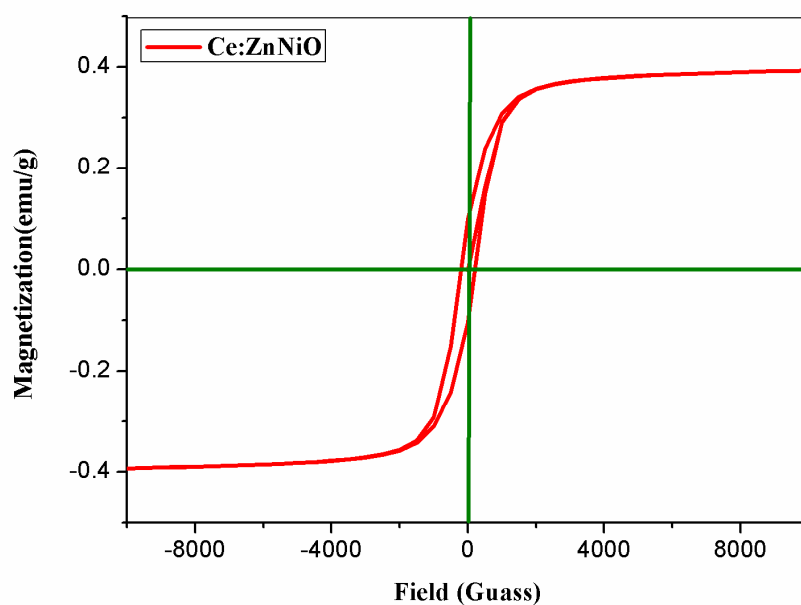


Figure 5.3: (b) Hysteresis loop of polymer capped Ce:ZnNiO nanocomposites

Compound	Magnetization (M_s) (emu/g)	Retentivity (M_r) (emu/g)	Mr/Ms ratio	Coercivity (H_c) (G)
ZnNiO	0.0158	0.00015	0.094	58
ZnNiO/PVP	0.0295	0.000519	0.176	172
Al:ZnNiO	0.5342	0.16146	0.303	219
Cu:ZnNiO	0.1904	0.01661	0.087	152
Pd:ZnNiO	0.0594	0.00640	0.107	153
Dy:ZnNiO	1.4330	0.28522	0.199	212
Ce:ZnNiO	0.3930	0.10112	0.254	201

Table 5.1: Magnetization, Retentivity and Coercivity of uncapped and capped ZnNiO, Al:ZnNiO, Cu:ZnNiO, Pd:ZnNiO, Dy:ZnNiO and Ce:ZnNiO nanocomposites

5.3 Antibacterial studies

Intrinsic properties of ZnO nanoparticles are mostly characterized by their size, crystallinity and morphology. Reducing the size to nanometer scale can modify their electrical, structural, optical and magnetic properties. ZnO is currently investigated as an antibacterial agent in nanoscale formulation. Nano sized ZnO can interact with the bacterial core or surface and subsequently exhibits distinct bacterial mechanisms. The antibacterial action of the material mainly depends on the production of reactive oxygen species on the surface of the nanoparticles. To determine their ability as an antibacterial agent, generally depends on the reactive oxygen species (ROS) which is mainly attributed to large surface area and enhanced oxygen vacancies. The superoxide, hydroxyl radical and hydrogen peroxide belonging to the ROS group can damage to DNA and cellular proteins and can lead to cell death.

Preparation of bacterial cultures

Antibacterial activity was determined by disc diffusion method against bacteria *Pseudomonas aeruginosa* (Gram negative) MTCC 2642 (Gram negative) MTCC 896 using PVP capped ZnNiO, uncapped ZnNiO, Al:ZnNiO, Pd:ZnNiO, Cu:ZnNiO,

Dy:ZnNiO and Ce:ZnNiO nanocomposites. These samples were suspended in sterile dimethyl sulfoxide (DMSO) and constantly sonicated until a uniform suspension was formed. Luria bertani (LB) agar medium was prepared and poured into petri dishes. After solidification, LB plates were streaked with test bacterial strains 2–3 times by rotating the plates at 60° angles for each streak to ensure the homogeneous distribution of the inoculums. After inoculation, sterile discs (6 mm Hi-Media) loaded with photo activated test samples were placed on the bacteria-seeded plates using sterile forceps. Simultaneously, DMSO loaded disc was used as a control and the plates were incubated at 37°C . After 24 h incubation, the zones of inhibition were measured and the assays were performed in triplicate.

Antibacterial activities of nanocomposites against Pseudomonas bacteria

Nanocomposites were studied to explore their utility as a potential candidate for biological applications due to their nontoxicity. In this work uncapped ZnNiO, capped ZnNiO and all the doped nanocomposites (Al:ZnNiO, Pd:ZnNiO, Cu:ZnNiO, Dy:ZnNiO and Ce:ZnNiO) were tested against *Pseudomonas aeruginosa* bacteria using disc diffusion method and the size of the inhibited zone formed around each disc. Fig. 5.4(a) and (b) shows photographs of antibacterial activity of capped ZnNiO and uncapped ZnNiO nanocomposite against *Pseudomonas* bacteria respectively. Among this uncapped ZnNiO show highest antibacterial activity (29 mm) than capped ZnNiO nanocomposite. The greater number of reactive oxygen species is mainly attributed to the diffusion ability of the reactant molecules and the formation of more oxygen vacancies. After surface passivation oxygen vacancies are decreased in capped ZnNiO than uncapped ZnNiO nanocomposite. Fluorescence spectra of the uncapped ZnNiO show an increased visible emission (green emission) due to the increase of oxygen vacancies. This is a confirmation for enhanced oxygen vacancies in uncapped ZnNiO.

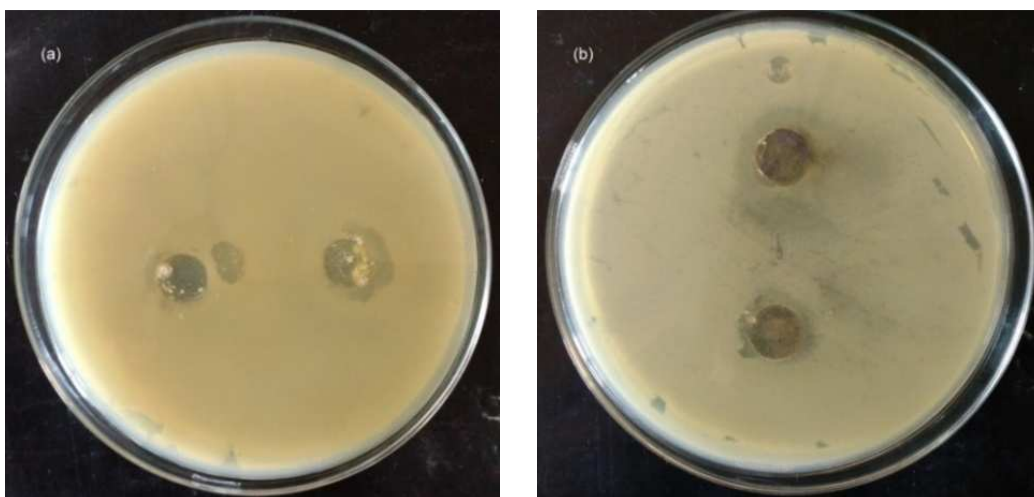


Figure 5.4: (a) Photographs of antibacterial activity of (a) capped ZnNiO and (b) uncapped ZnNiO nanocomposites respectively.

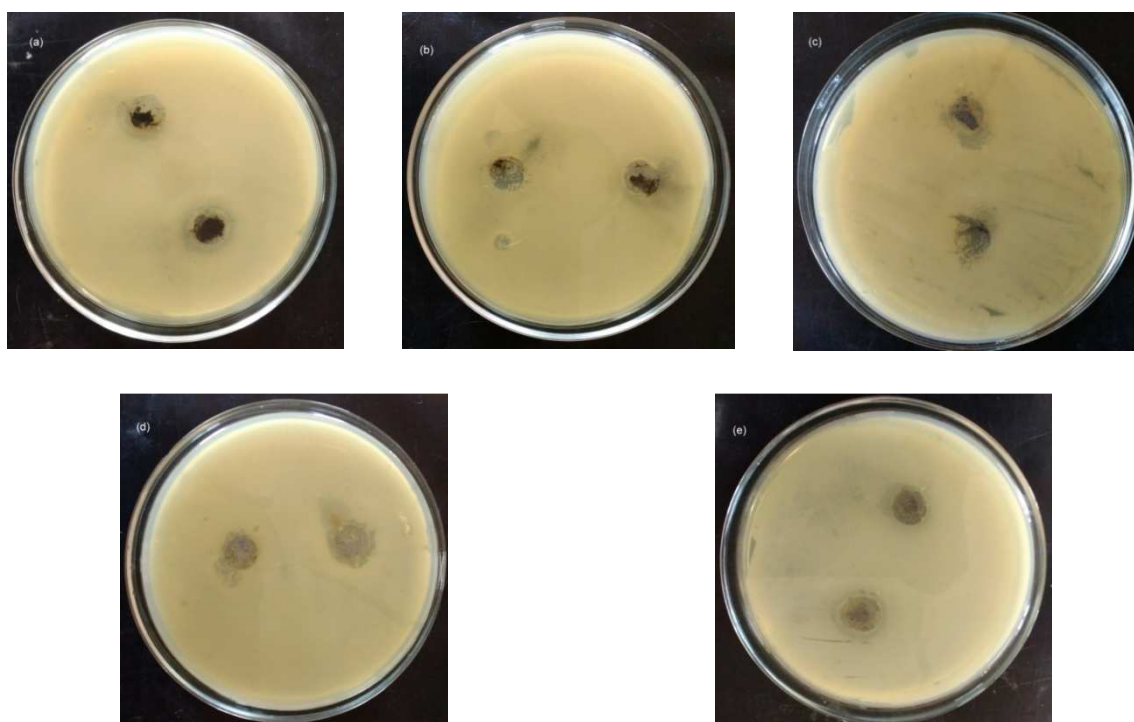


Figure 5.5: Photographs of antibacterial activity of (a) Al: ZnNiO and (b) Pd:ZnNiO (c) Cu:ZnNiO (d) Dy:ZnNiO (e) Ce:ZnNiO nanocomposites

Compound	Minimum Inhibitory Concentration			
	Pseudomonas aeruginosa			
	MIC (200 µg)	Activity (mm)	Activity (mm)	MIC (100 µg)
ZnNiO	0.855	29	18	0.820
ZnNiO/PVP	0.890	22	16	0.840
Al:ZnNiO	0.895	21	15	0.915
Pd:ZnNiO	0.865	27	23	0.770
Cu:ZnNiO	0.915	17	15	0.850
Dy:ZnNiO	0.860	28	18	0.820
Ce:ZnNiO	0.910	18	14	0.860

Table 5.2: Calculated antibacterial activities and MIC of all the nanocomposites.

Antibacterial activity of all the doped nanocomposites (Al:ZnNiO, Pd:ZnNiO, Cu:ZnNiO, Dy:ZnNiO and Ce:ZnNiO) are shown in Fig 5.5(a), (b),(c),(d) & (e). Among all the doped nanocomposites Al:ZnNiO and Dy:ZnNiO nanocomposites has the maximum antibacterial activity against Pseudomonas bacteria.

Minimum inhibitory concentrations (MIC) were calculated by subtracting the zone of inhibition from the sample and the whole divided by the concentration of the sample and the diameter of the inhibition on around each disc was measured in mm after 24 hrs.

$$MIC = \frac{\text{Concentration of the test sample} - \text{Zone of inhibition in mm}}{\text{Concentration of the test sample}}$$

Antibacterial activity and minimum inhibitory concentration of all the nanocomposites are shown in table 5.2.

5.4 Conclusion

The surface layer magnetic moment anomalies may be due to broken exchange bonds and high anisotropy layer on the surface. These effects are more intense in

case of metaloxides because of the super-exchange interactions through the oxygen ions. The presence of another atom in the form of impurity or an absence of the oxygen ions at the surface leads to the breakage of the super-exchange bonds between the magnetic cations, inducing a large surface spin disorder. If the surfactant molecules adsorb on the surface and the electrons involved can no longer participate in the super-exchange interaction, spin pinning occurs. The superparamagnetic behaviour of non-capped ZnNiO may be due to the small size of the particle. All the capped particles are showed ferromagnetic nature, may be originated from either the exchange interaction between the holes and electrons from the valence band and the localized d spins on the transition metal ions or may be related to the O^{1-} defects. This ferromagnetism of the samples may lead to applications in industries. Antibacterial activity test of the samples against pseudomonas bacteria show that after surface passivation, the activity was decreased due to the lack of oxygen vacancy. Adjunction of Pd and Dy in ZnNiO activity was increased than other capped nanocomposites.

References

- [1] R. D. K. Misra, A. Kale, R. S. Srivatsava, O. Senkov, *Mater. Sci. Technol.* 19 (2003) 826.
- [2] R. D. K. Misra, A. Kale, B. Hooi, J.Th. DeHosson, *Mater. Sci. Technol.* 19 (2003) 1617.
- [3] A. Kale, S. Gubbala, R. D. K. Misra, *J. Magn. Magn. Mater.* 277 (2004) 350.
- [4] T. Sato, K. Haneda, M. Seki, T. Ijima, *Appl. Phys. A*, 50 (1990) 139.
- [5] R. H. Kodama, *J. Magn. Magn. Mater.* 200 (1999) 359.
- [6] A. E. Berkowitz, R. H. Kodama, S. A. Makhlof, F. T. Parker, F. E. Spada, E. J. McNiff Jr., S. Foner, *J. Magn. Magn. Mater.* 196 (1999) 591.
- [7] E. M. Chudnovsky, L. Gunther, *Phy. Rev. Lett.* 60 (1988) 661.
- [8] F. T. Parker, F. F. Spada, T. J. Cox, A. E. Berkowitz, *J. Magn. Magn. Mater.* 162 (1996) 122.
- [9] R. W. Chantrell, K. O'Grady, et al., in: R. Gerber (Ed.), *Applied Magnetism*, Kluwer Academic Publishers, Dordrecht, the Netherlands, (1994)113.
- [10] G. C. Hadjipanayis, G. A. Prinz, G. C. Hadjipanayis, G.A. Prinz (Eds.), *Science and Technology of Nanostructured Materials*, Plenum Press, New York, 1991.
- [11] S. S. Perkins, N. More, K. P. Roche, *Phys. Rev. Lett.* 64 (1990) 2304.
- [12] D. K. Kim, W. Voit, W. Zapka, B. Bjelk, M. Muhammed, K. V. Rao, *Mater. Res. Soc. Symp. Proc.* 676 (2001) 321.
- [13] P. C. Fannin, A. Slawska-Waniewska, P. Didukh, A. Giannitoics, S. W. Charles, *Eur. Phys. J. Appl. Phys.* 17 (2002) 3.
- [14] M. H. Sousa, F. A. Tourinko, J. Depeyrot, G. J. da Silva, M. C. F. Lara, *J. Phys. Chem. B* 105(2001) 1169.
- [15] M. E. McHenry, D. E. Loughin, *Acta Mater.* 48 (2000) 223.
- [16] M. Venkatesan, C. B. Fitzgerald, J. M. D. Coey, *Nature* 430 (2004) 630.
- [17] A. Sundaresan, R. Bhargavi, N. Rangarajan, U. Siddesh, and C. N. R. Rao, *Phys. Rev. B* 74 (2006) 161306(R) .

- [18] S. Bannerjee, M. Mandal, N. Gayathri, M. Sardar, *Appl. Phys. Lett.* 91 (2007) 182501.
- [19] P. Crespo, R. Litraín, T. C. Rojas, M. Multigner, J. M. de la Fuente, J. C. Sánchez-Lopez, M. A. García, A. Hernando, S. Penade's, A. Fernández, *Phys. Rev. Lett.* 93 (2004) 087204.
- [20] M. A. Garcia, J. M. Merino, P. E. Fernández Pinel, A. Quesada, J. de la Venta, M. L. Ruiz González, G. R. Castro, P. Crespo, J. Llopis, J. M. González-Calbet, and A. Hernando, *Nano Lett.* 7 (2007) 1489.
- [21] K. Potzger, S. Zhou, J. Grenzer, M. Helm, and J. Fassbender, *Appl. Phys. Lett.* 92 (2008) 182504.
- [22] C. Madhu, A. Sundaresan, and C. N. R. Rao, *Phys. Rev. B* 77 (2008) 201306(R).
- [23] H. Pan, J. B. Yi, L. Shen, R. Q. Wu, J. H. Yang, J. Y. Lin, Y. P. Feng, J. Ding, L. H. Van, and J. H. Yin, *Phys. Rev. Lett.* 99 (2007) 12720.
- [24] K. W. Liu, M. Sakurai, M. Aono, *J. Appl. Phys.* 108 (2010) 043516.
- [25] D. Y. Inamdar, A. D. Lad, A. K. Pathak, I. Dubenko, N. Ali, and S. Mahamuni, *J. Phys. Chem. C* 114 (2010) 1451.
- [26] D. Gao, J. Zhang, G. Yang, J. Zhang, Z. Shi, J. Qi, Z. Zhang, and D. Xue, *J. Phys. Chem. C* 114 (2010) 13477.
- [27] K. Yang, R. Wu, L. Shen, Y. P. Feng, Y. Dai, and B. Huang, *Phys. Rev. B*, 81 (2010) 125211.

Chapter 6

Effects of capping agent on optical properties

6.1 Introduction

Zinc oxide is an excellent semiconductor and its properties have been extensively studied since the early days of semiconductor technology [1]. More than its bulk usage, nowadays zinc oxide has been widely used in electro-optic industry, thanks to the unprecedented level of research work going on with these metal oxides. Its bulk and nanoform have many interesting features. Among the various metal oxides, nanoparticles of ZnO have a vast range of applications extending from cosmetics to electronics. Owing to its wide band gap (3.36 eV), large exciton binding energy (~ 60 meV) and reasonably good bond strength, it is considered as a very good material for short wavelength opto-electronic applications. The quantum size effects shown by the nano materials have made them more attractive and aroused great interest in recent years. Due to the remarkable properties exhibited by the nano structures, researchers have been pondering over the synthesis and characterization as well as device applications using ZnO and its related compounds. A great deal of

work has been going on elucidating the emission processes of ZnO and its related nano structures near band edge to make sufficiently suitable emitters as well as light detectors in the visible-UV region.

Generally, ZnO exhibits near band edge UV emission from free exciton recombination with broad visible emission which originates from intrinsic or extrinsic defects [2-7]. In order to fabricate high efficient optoelectronic devices, the deep level emissions (DLE) in the visible region should be eliminated. Ritchers et al. have studied the PL properties of ZnO/Al₂O₃ core-shell nanowires and found that, near band emission (NBE) at low temperature was enhanced, by suppressing deep level emissions [8]. Hong et al. reported the study of annealing effect on the property of UV emission and green emission. Cheol Hyoun Ahn, et al. have made a comparative analysis of deep level emission in ZnO layers on samples deposited by various methods and they finally concluded that, the growth methods as well as the growing conditions have remarkable impact on the deep level emission [9]. In addition, hydrogenation can also found to improve optical properties by decreasing deep level emission [10]. The surface modified nanoparticles have been found to exhibit significantly strong UV emissions as well as third order non-linear optical properties. Capping the nanoparticles by a suitable polymer could be effectively demonstrated in the suppression of deep level emissions, caused by oxygen vacancies [11]. Polymer capping has also been demonstrated to suppress deep level emission with enhanced UV emission [12- 13].

6.2 Diffuse reflectance spectra (DRS)

Diffuse reflectance spectra of the nanocomposites were characterized by using UV-Vis NIR spectrophotometer (JASCO V 550 UV/Vis) in the wavelength range from 300-600 nm. Room temperature UV-vis/diffuse reflectance spectra of the uncapped and PVP capped ZnNiO nanoparticles are presented in Fig 6.1. The exciton absorption edge wavelengths of capped ZnNiO (~368 nm) is substantially blue shifted compared to uncapped ZnNiO (~384 nm) nanocomposites. This blue shift is due to the strong confinement effect [14]. Another difference between the uncapped and capped ZnNiO is the appearance of a bump around 469 nm for uncapped sample

and is due to the exciton absorption from large nanoparticles from the composite. It is well established that particle size calculated from XRD is well matched to the particle size estimated from the excitonic absorption peak based on effective mass approximation [15]. Diffuse reflectance spectra of the Al:ZnNiO, Cu:ZnNiO and Pd:ZnNiO nanocomposites are shown in Fig. [6.2 (a), (b) and (c)] and Dy:ZnNiO and Ce:ZnNiO are shown in Fig [6.3(a) and b)]. Generally particles exhibit blue shift of excitonic peak in the absorption spectra [16]. Electron-phonon coupling, lattice distortion and localization of charge carriers due to point defects are perhaps the main causes for the red shift of the absorption edge when compared to pure ZnO (3.47 eV). Here observed the red shifted near band edge emission, which on similar lines are probably due to preferential emissions of the large sized nanorods. This in fact confirms the presence of such large rods, as observed in SEM image.

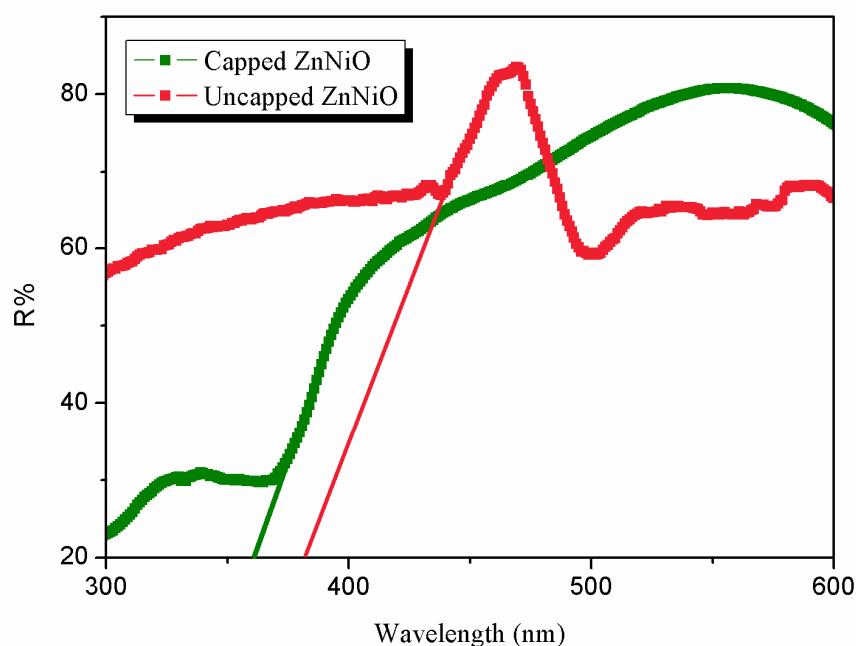


Figure 6.1: UV-vis/diffuse reflectance spectra of the uncapped and polymer capped ZnNiO nanocomposites

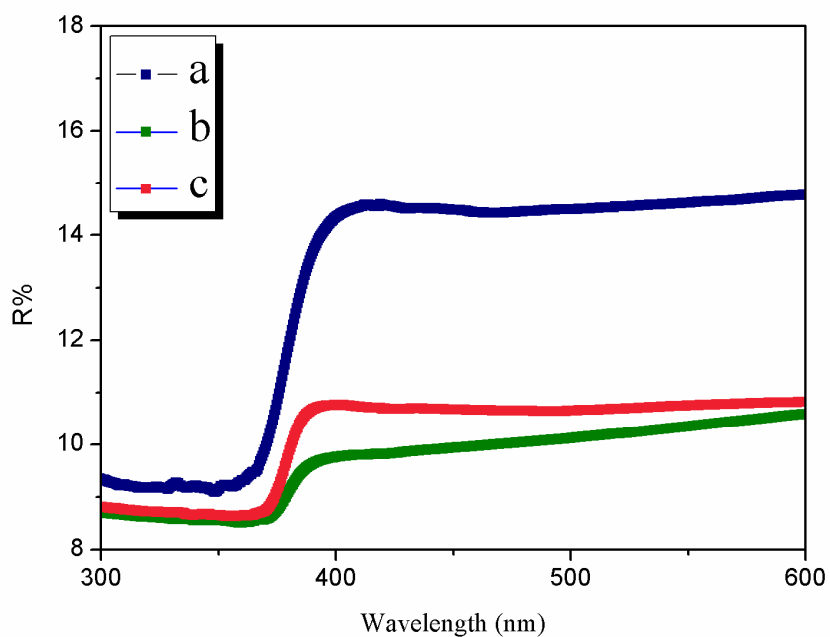


Figure 6.2: UV-vis/diffuse reflectance spectra of the polymer capped (a) Al:ZnNiO (b) Pd:ZnNiO (c) Cu: ZnNiO nanocomposites

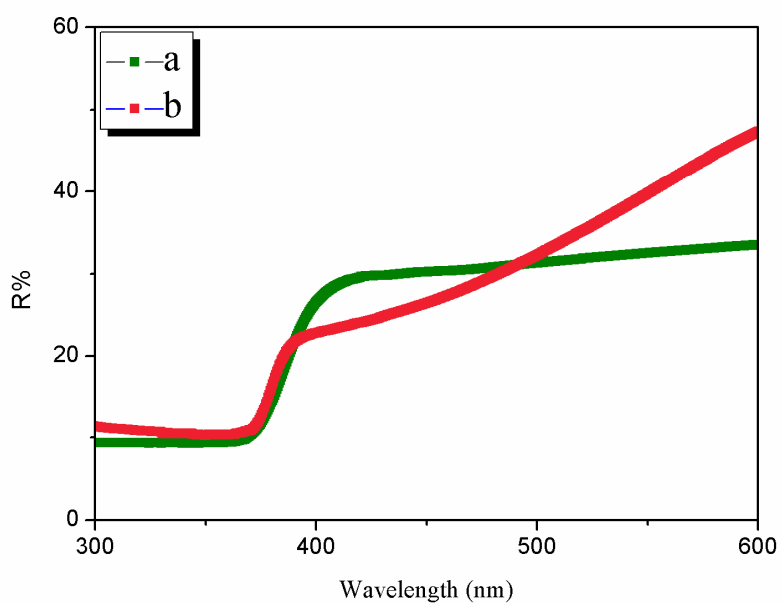


Figure 6.3: UV-vis/diffuse reflectance spectra of the polymer capped (a) Dy:ZnNiO (b) Ce: ZnNiO nanocomposites

6.2.1 Particle size determination

From the diffuse reflectance spectra, average particle size has been confirmed by using the relation following the hyperbola band model [17].

$$R = \frac{\sqrt{(2\pi^2 h^2 E_{gb})}}{\sqrt{(m^* [E_{gn}^2 - E_{gb}^2])}} \quad (6.1)$$

Here $2R$ corresponds to the particle size, E_{gb} and E_{gn} represents the bulk bandgap and nanoparticle bandgap (calculated from the absorption edge, as shown in fig. 6.1, 6.2 and 6.3) respectively and m^* , is the effective mass. Particle size, assessed from both XRD and absorption edge, are well matching.

6.2.2 Bandgap determination

Using the Kubelka-Munk treatment on diffuse reflectance spectra of the samples, it is possible to extract their bandgap unambiguously. Determination of bandgap is an important feature for selecting these materials in optoelectronics. The optical bandgap of the nanocomposites was determined by applying Kubelka-Munk function.

$$F(R) = (1-R)^2/2R = K/S \quad (6.2)$$

where, R is the reflectance, K is the molar absorption coefficient and S is the scattering coefficient. The Kubelka-Munk theory predicts a linear relationship between the intensity of spectral lines and concentration of the scatterer when it encounters almost uniform scattering in non-absorbing medium. Since the particles sizes of the nano-composites prepared are small and uniform to a great extent, the Kubelka-Munk model could be applied for the determination of band gap using the reflectance spectra. Using the Tauc-plot $[F(t)hv]^n$ vs hv , the semiconductor band gap is determined. An extrapolation of the linear region of a plot of $[F(t)hv]^2$ on the Y axis, versus hv , on the X axis, gives the value of the optical bandgap E_g . The calculated bandgaps, from diffuse reflectance spectra of PVP capped ZnNiO nanocomposites and all doped ZnNiO nanocomposites were found to be less than

that of bulk ZnO. Reduction in bandgap is caused by the presence of occupied Ni 3d states, this 3d states raises the valence band maximum and lowering the conduction band minimum [18]. Researchers note that band gap increases with reducing particle size [19, 20], but here we have observed a reduced bandgap that is only due to Ni doping. Furthermore, the observed redshift in the band edge for Ni doped ZnO nanoparticle is attributed to the increasing sp-d exchange interactions between the band electrons and the localized d-electrons of the Ni²⁺ ions. Band gap reductions are controlled by the surface of the nanoparticles, lattice strain, and vacancies. $[F(t)h\nu]^2$ vs $h\nu$ plots of the polymer capped and uncapped nanocomposites are shown in fig 6.4, 6.5 and 6.6.

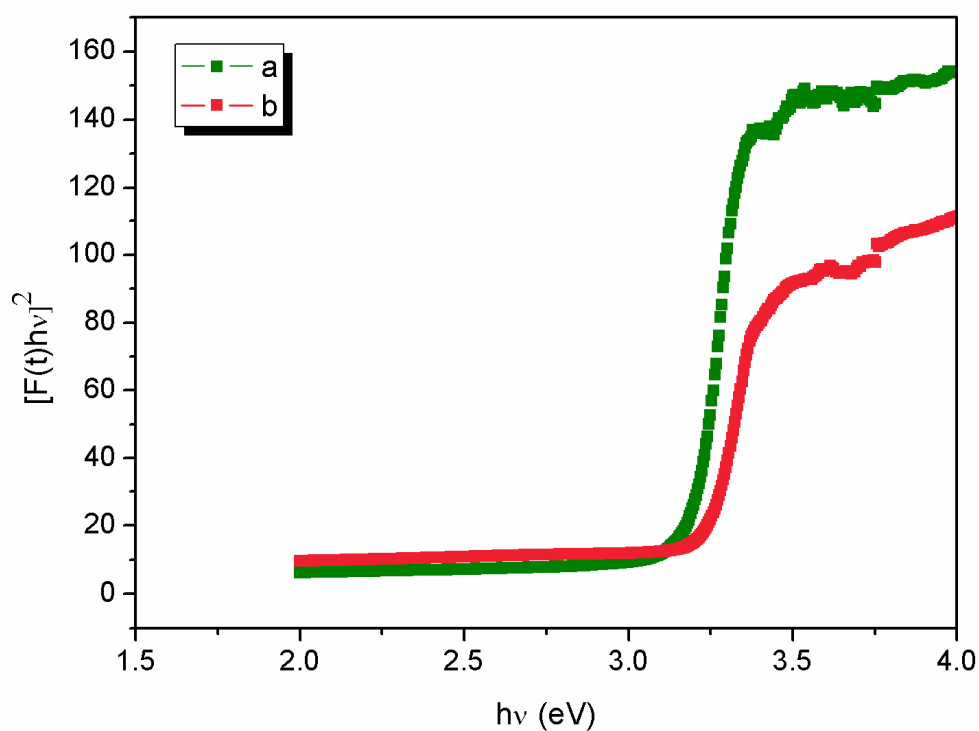


Figure 6.4: $[F(t)h\nu]^2$ vs $h\nu$ plots of (a) uncapped ZnNiO
(b) polymer capped ZnNiO nanocomposites

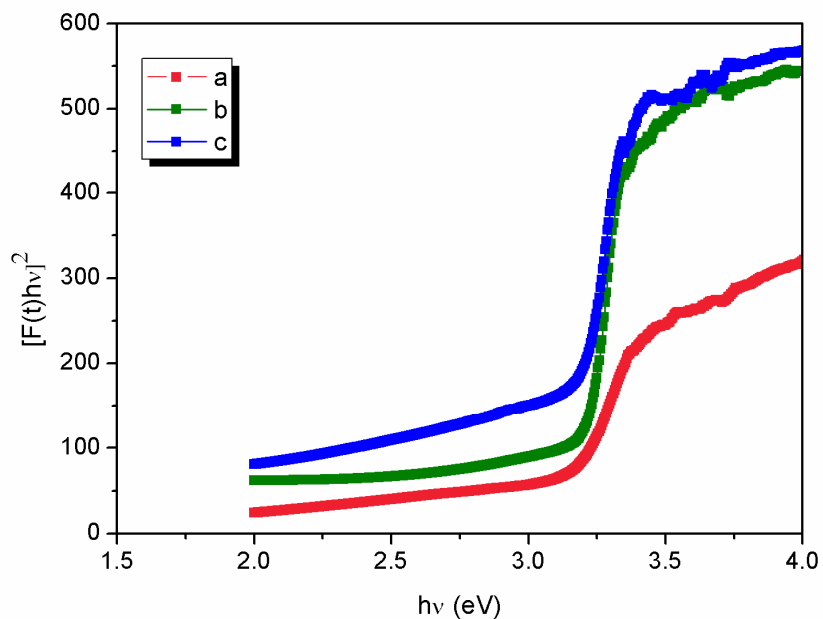


Figure 6.5: $[F(t)hv]^2$ vs $h\nu$ plots of polymer capped (a) Al:ZnNiO (b) Pd:ZnNiO (c)Cu:ZnNiO nanocomposites

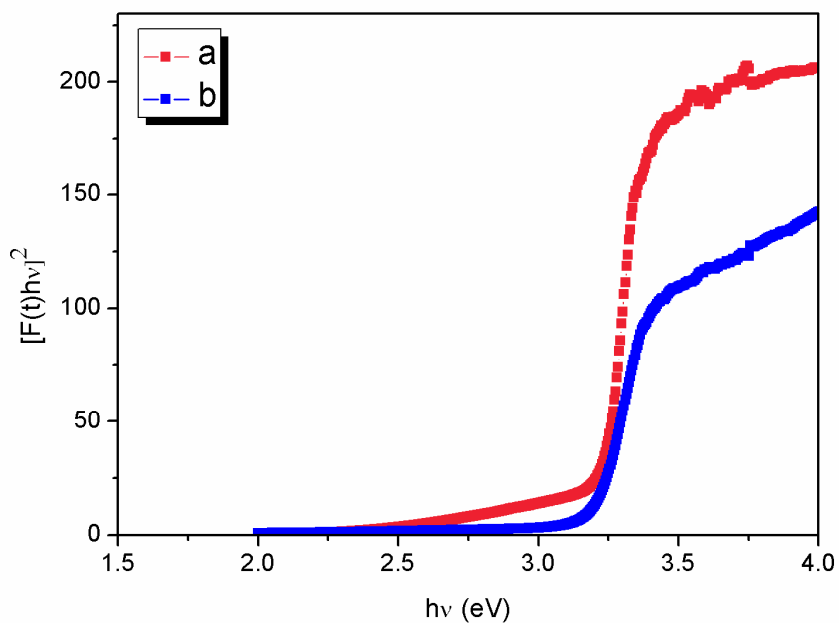


Figure 6.6: $[F(t)hv]^2$ vs $h\nu$ plots of polymer capped (a) Dy:ZnNiO (b) Ce:ZnNiO nanocomposites

6.2.3 Urbach energy determination

The width of the defect bands formed as an intermediate state in the band gap of ZnO can be determined from the reflectance spectra. These defect band states create a band tail extending from the lower of conduction band to deep down of band gap, and similarly, the defect states very near to the valence band also smear the valence band edge deep inside the gap. Therefore, on both sides of the valence band maximum and conduction band minimum, an energy tail is formed. This defect tail is known as the Urbach tail, and the energy associated with this defect tail is referred to as Urbach energy.

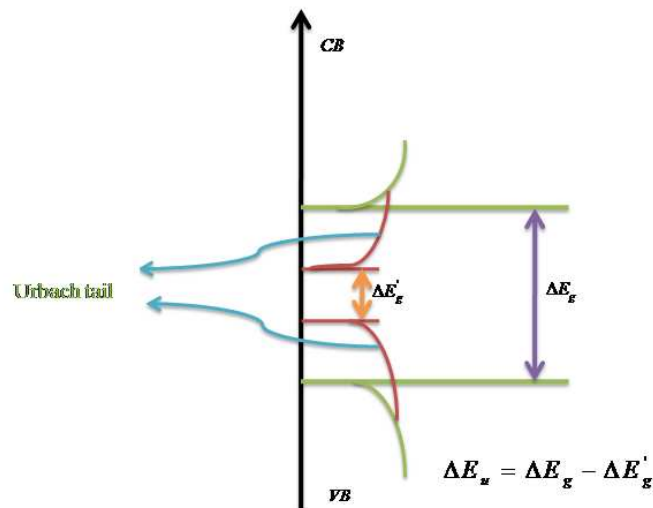


Figure 6.7: Schematic diagram of Urbach tail formation

Urbach energy often refers to the exponential slope of optical absorption data in the bandgap, which arises from the convolution of the valence band with the conduction band tail. Urbach energy (E_u) is calculated by using the equation $\alpha = \alpha_0 \exp(E / E_u)$ [21], where α is the absorption coefficient and E is the photon energy of the sample. Generally band gap reductions are controlled by the surface properties of the nanoparticles, lattice strain, and vacancies in the body of the material. The Urbach

tail decays exponentially into the bandgap of the material with Urbach energy E_u . The defects which are created mainly by making deviations from ideal stoichiometry will change the magnitude of Urbach energy. Calculated values of Urbach energy and bandgap of all the samples are shown in table.

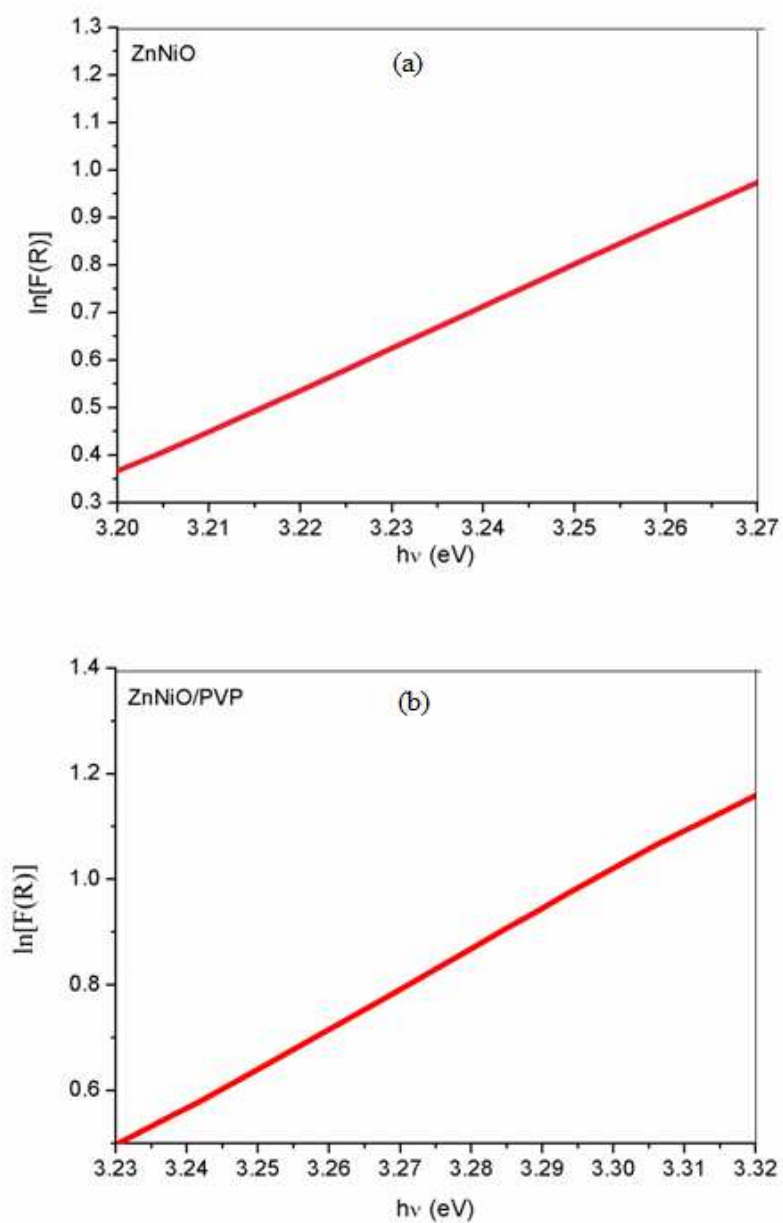


Figure 6.8: $\ln[F(R)]$ vs $h\nu$ plots of (a) uncapped ZnNiO
(b) polymer capped ZnNiO nanocomposite

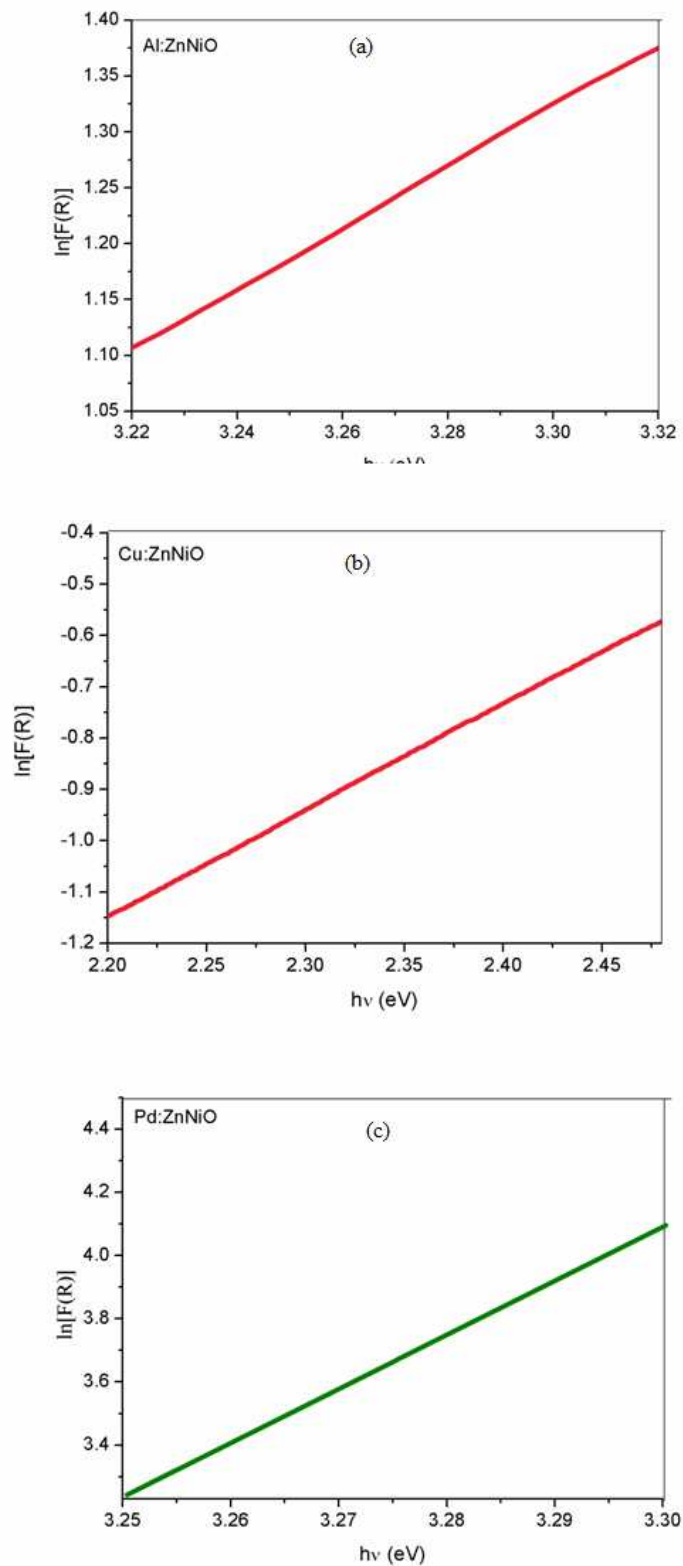


Figure 6.9: $\ln[F(R)]$ vs $h\nu$ plots of polymer capped (a) Al:ZnNiO (b) Cu:ZnNiO (c) Pd: ZnNiO nanocomposites

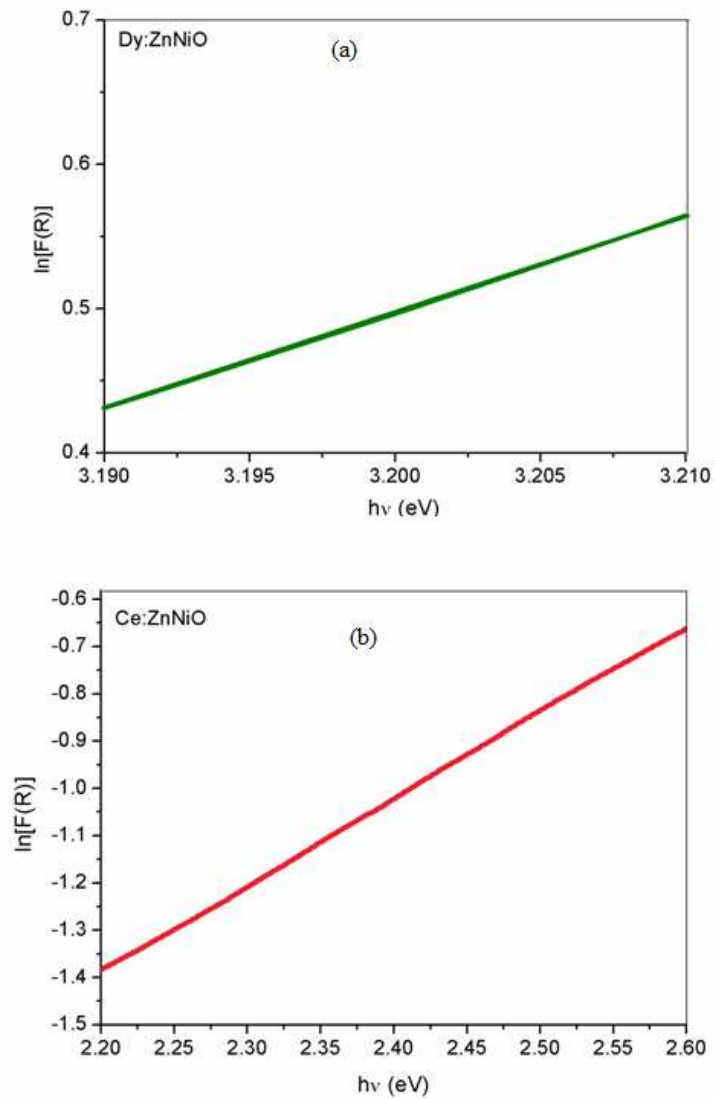


Figure 6.10: $\ln[F(R)]$ vs $h\nu$ plots of polymer capped (a) Dy:ZnNiO (b) Ce:ZnNiO nanocomposites

Sample	Bandgap(eV)	Urbach energy (eV)
ZnNiO	3.186	0.294
ZnNiO/PVP	3.241	0.128
Al:ZnNiO	3.239	0.118
Cu:ZnNiO	3.209	0.250
Pd:ZnNiO	3.214	0.320
Dy:ZnNiO	3.199	0.217
Ce:ZnNiO	3.182	0.227

Table 6.1: Calculated bandgap energy and Urbach energy

6.3 Fluorescence spectra

Fluorescence is a very effective method for the investigation of the intrinsic point defects in the sample responsible for visible and UV emission. Room temperature fluorescence spectra of the nanocomposites were carried out by a fluorescence spectrometer (SPEX F212) excited at exciton wavelength of 325 nm. Fig 6.13 shows the fluorescence spectra of capped and uncapped ZnNiO nanocomposites. Capped sample evince two emission bands (one is at ~ 356.3 nm and other is at ~ 390 nm in the ultraviolet region. This ultraviolet near band edge emission is attributed to the recombination of free excitons. The UV fluorescence peak is quite weak in case of uncapped one but this is strong in capped nanocomposites [Fig.6.13] due to the quenching of visible emission. The strong fluorescence emission observed in this case demonstrates the good quality of the sample due to surface passivation. Near band edge emission of the capped samples extended to their emission in the violet –blue region. Excited electrons in the conduction band relax to the zinc interstitials band through non-radiative transition and then transit to the valence band which makes violet emission in ZnO. Electronic transition from donor energy level of zinc interstitials to acceptor level of zinc vacancies is responsible for blue emissions. Normally strong violet emission indicates that high concentrations of zinc interstitials exist on the surface. Schematic diagram of energy level transitions are shown in fig 6.11. In the case of capped ZnNiO this highly enhanced violet-blue emission may be due to the effect of PVP because PVP itself has a blue emission [Shown in fig 6.12]. Emission of ZnNiO and blue emission of PVP combined together and results highly enhanced UV extended blue emission in capped ZnNiO nanocomposites. The double peak emissions in the ultraviolet region are associated with ground state emissions from islands in different size branches [22]. Surface passivation effects have significantly enhanced the UV emission with reducing surface defects [23-24]. This in turn suppresses the oxygen vacancy related green emissions by surface passivation in this case, because oxygen vacancies are mainly located at the rod surfaces. So I got a suppressed deep level emission with enhanced UV emission [Fig.6.13]. This highly intensed double peak emission in UV region enhanced their applications in UV emitters. The same results are repeated in case of

capped Al:ZnNiO, Pd:ZnNiO, Cu:ZnNiO, Dy:ZnNiO and Ce:ZnNiO nanocomposites [Fig. 6.14, 6.15 (A) & (B), 6.16 (A) & (B), 6.17(A) &(B)].

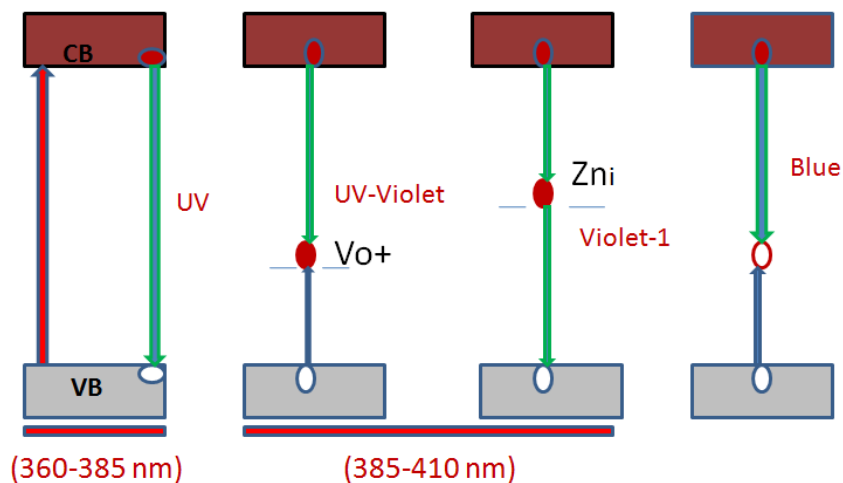


Figure 6.11: Schematic diagram of energy level transition

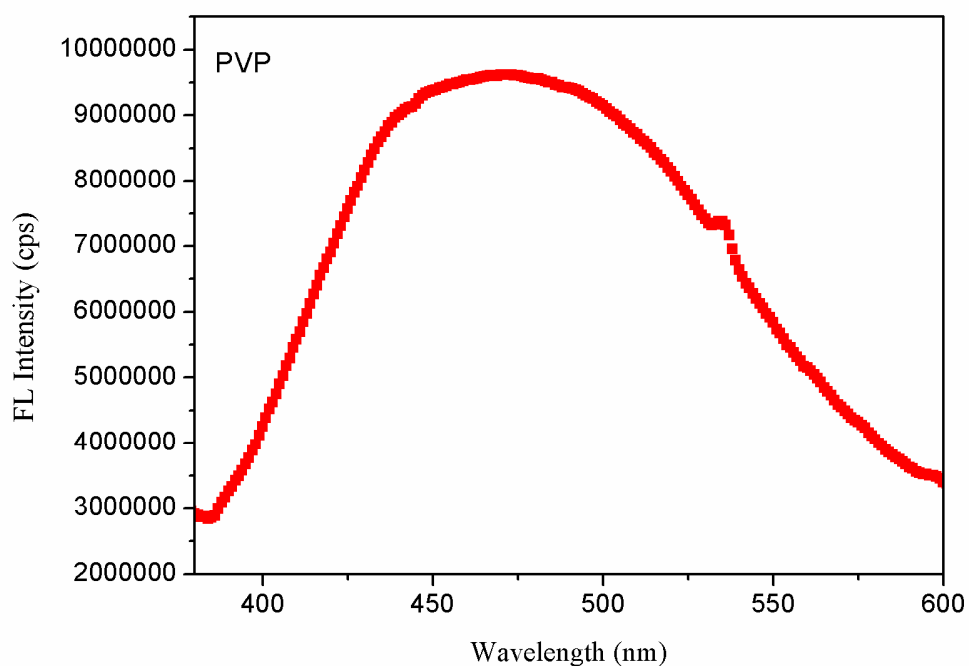


Figure 6.12: Fluorescence spectra of polyvinyl pyrrolidone (PVP)

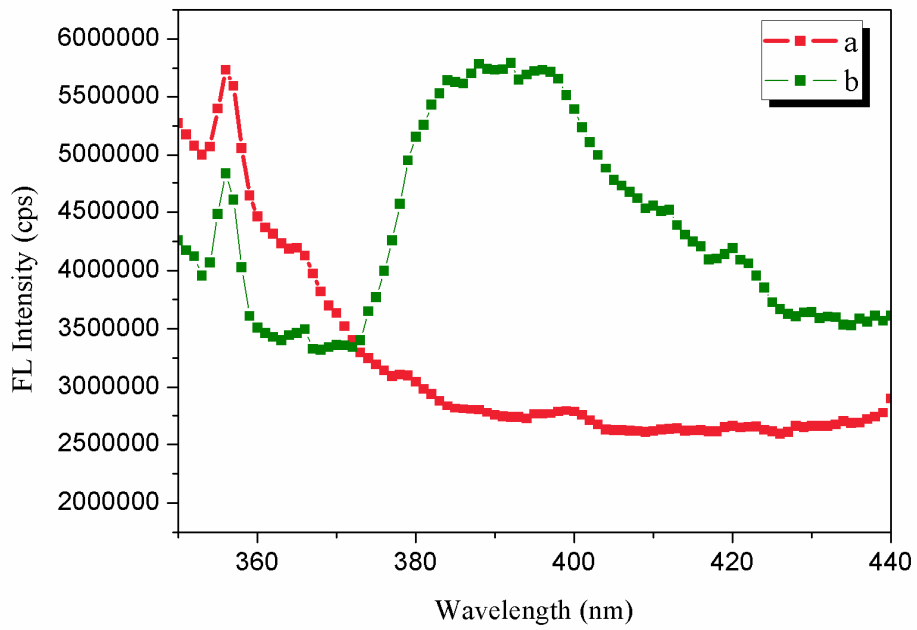


Figure 6.13: Room temperature fluorescence spectra of (a) ZnNiO (b) ZnNiO-PVP nanocomposite in the UV region

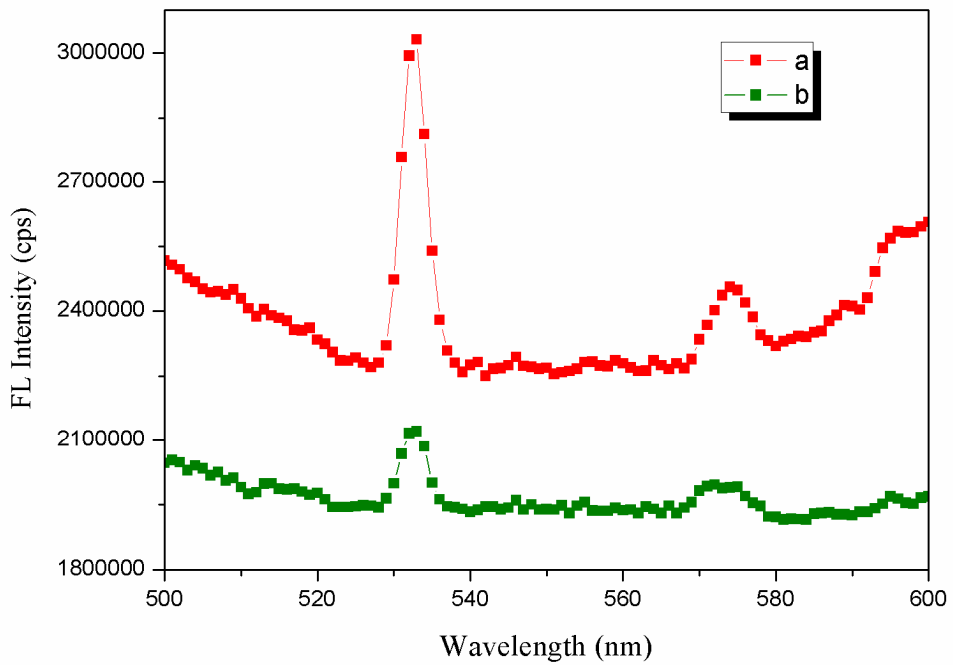


Figure 6.14: Room temperature fluorescence spectra of (a) ZnNiO (b) ZnNiO-PVP nanocomposite in the visible region

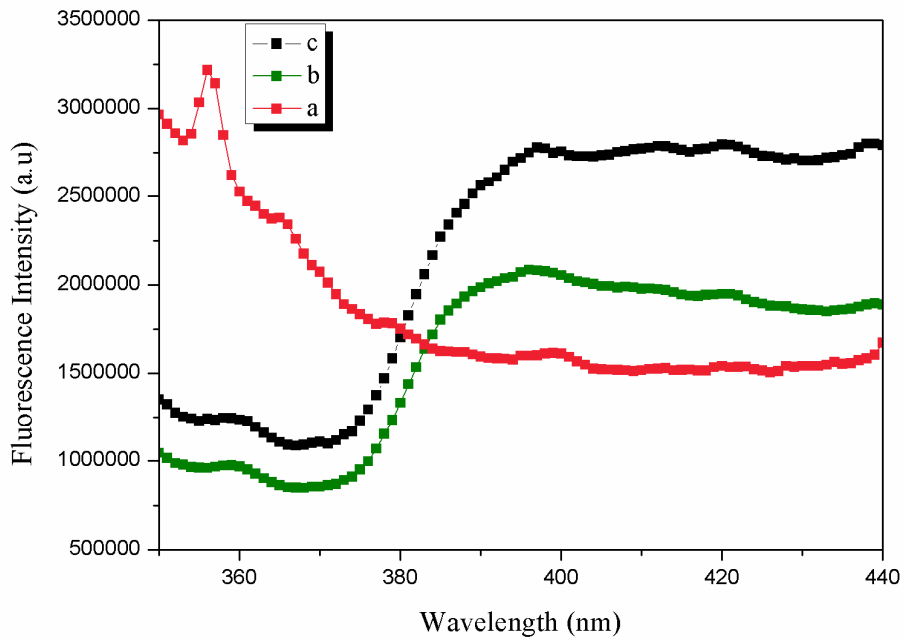


Figure 6.15: (A) Room temperature fluorescence spectra (a) ZnNiO (b) Pd: ZnNiO and (c)Al: ZnNiO nanocomposite

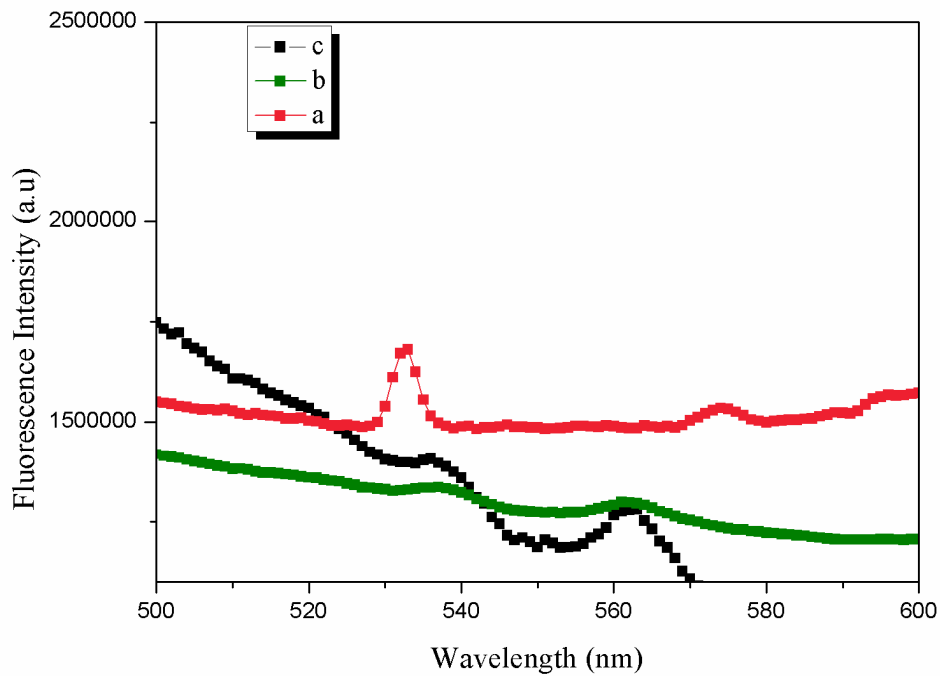


Figure 6.15: (B) Room temperature fluorescence spectra (a) ZnNiO (b) Pd: ZnNiO and (c)Al: ZnNiO nanocomposite in the visible region

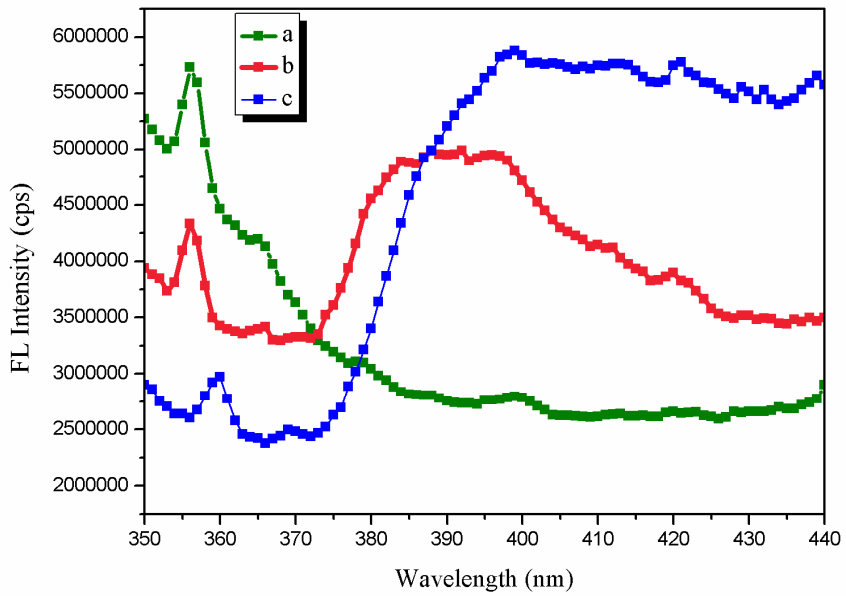


Figure 6.16: (A) Room temperature fluorescence spectra (a) ZnNiO (b) ZnNiO-PVP and (c) Cu:ZnNiO nanocomposite

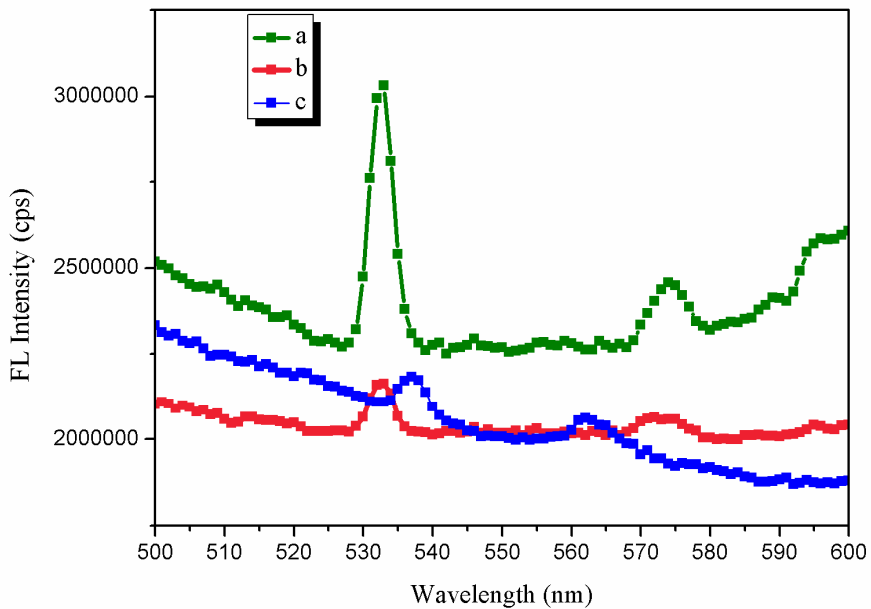


Figure 6.16: (B) Room temperature fluorescence spectra (a) ZnNiO (b) ZnNiO-PVP and (c) Cu:ZnNiO nanocomposite in the visible region

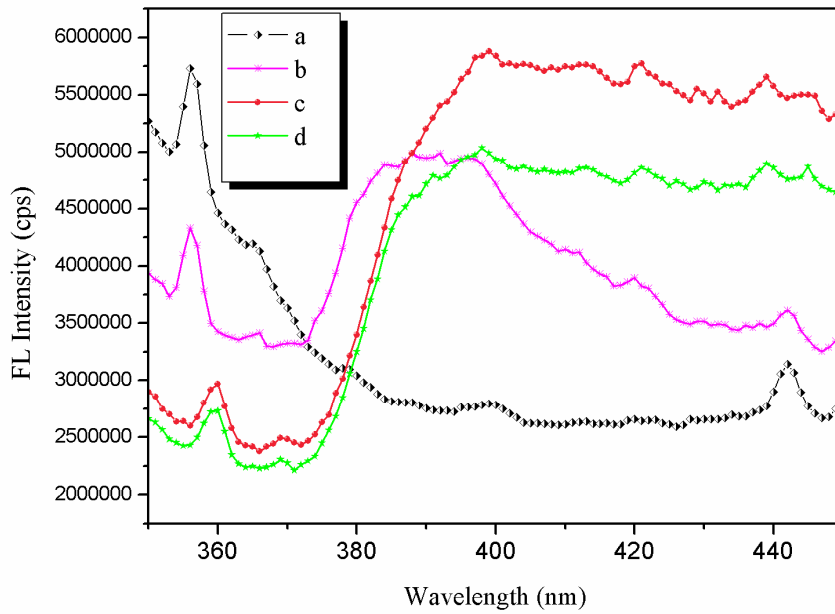


Figure 6.17: (A) Room temperature fluorescence spectra of (a) ZnNiO (b) ZnNiO-PVP (c) Dy:ZnNiO (d) Ce:ZnNiO nanocomposite in the UV region

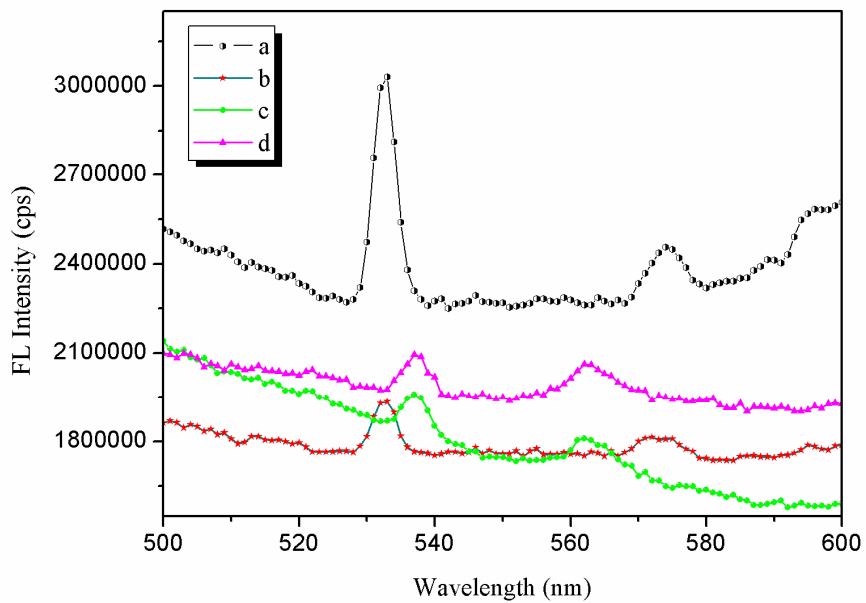


Figure 6.17: (B) Room temperature fluorescence spectra of (a) ZnNiO (b) ZnNiO-PVP (c) Dy:ZnNiO (d) Ce:ZnNiO nanocomposite in the visible region

6.3.1 Fluorescence lifetime

Fluorescence lifetime decay measurement is an exceptional tool in biology, chemistry and physics for investigating the dynamics of excited states. Fluorescence lifetime of the fluorophore is determined by using time domain and frequency domain data acquisition methods. Instrumentation and data acquisition methods for time domain and frequency domain methods are different but both approaches are mathematically equivalent and data can be interconverted through Fourier transform.

In time domain approach, sample is excited with a short pulse of light < 2 ns from the flash lamp, pulsed lasers, laser diodes with sufficient delay between pulses. A variety of fluorescence detection methods are available for lifetime measurements but time-correlated single photon counting TCSPC has enhanced quantitative photon counting. Avalanche photodiodes are used to record this time dependent distribution of emitted photons after each pulse. The fluorescence life time is calculated from the slope of the decay curve according to the equation

$$F(t) = F_0 e^{-t/\tau} \quad (6.1)$$

Where F_0 is the intensity at time $t=0$ and t is the time after absorption.

Fluorescence decay spectra of the samples were recorded at 325 nm excitation wavelength at room temperature. Fluorescence lifetime of the particles mainly depends on the excited state from which the electron transition starts. All fluorescence processes have a common excited state, that is, the conduction band edge. If the electrons in conduction band edges relaxed to the deep levels and combined with holes captured from the valance band, fluorescence life time would be in the range of nanoseconds otherwise conduction band electrons first relaxed to a shallow donor level and then combined with holes to release photons, then lifetime of fluorescence would be up to several hundred of nanoseconds [25].

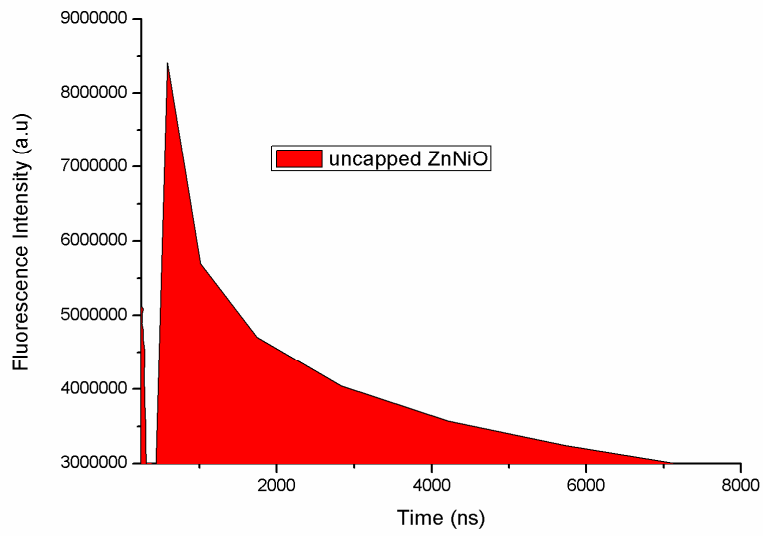


Figure 6.18: Fluorescence decay curve of uncapped ZnNiO nanocomposite

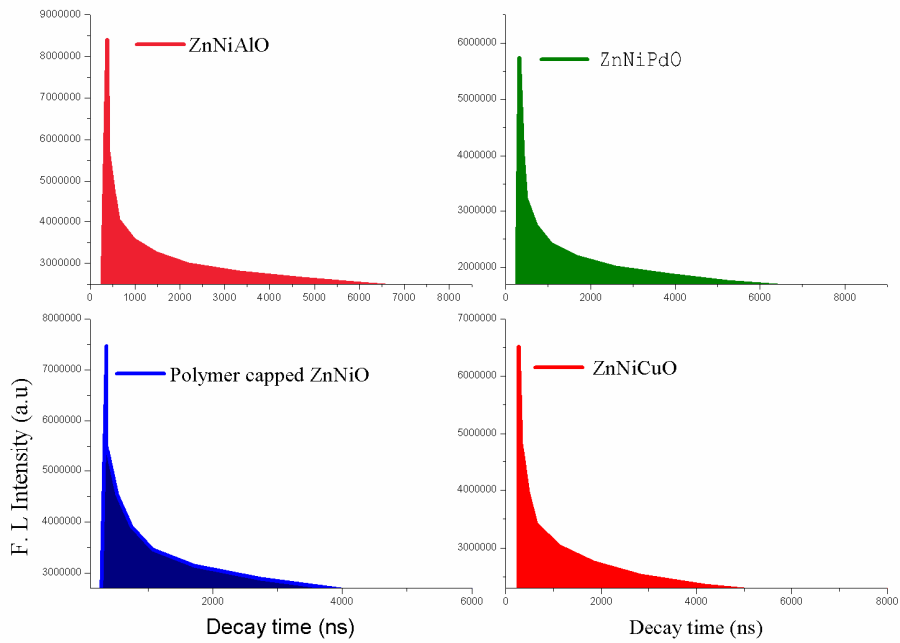


Figure 6.19: Fluorescence decay curve of polymer capped ZnNiO, Al:ZnNiO, Pd:ZnNiO and Cu:ZnNiO nanocomposites

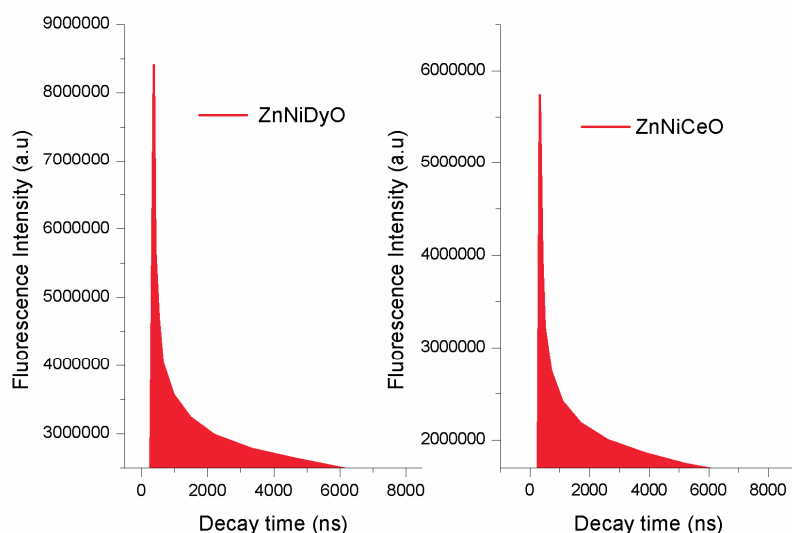


Figure 6.20: Fluorescence decay curve of Dy: ZnNiO and Ce:ZnNiO nanocomposites

Fluorescence life time exponential decay curve of polymer capped ZnNiO and Cu:ZnNiO nanocomposites are shown in fig.6.20. These nanocomposites have life time in the range of 16 -16.71 ns and is tabulated in table 6.3.

Compound	τ_1 (ns)	τ_2 (ns)	τ_{ave} (ns)
ZnNiO	1.42	30.76	16
ZnNiO-PVP	1.673	31.749	16.71
Al:ZnNiO	1.661	31.295	16.53
Cu:ZnNiO	1.568	31.749	16.55
Pd:ZnNiO	1.554	31.551	16.56
Dy:ZnNiO	1.773	26.563	14.14
Ce:ZnNiO	1.614	31.119	16.36

Table 6.2: Calculated lifetime of the samples

6.4 Correlation between particle size and bandgap energy

In the parabolic band structure the bandgap energy and absorption coefficient are related through the equation

$$\alpha h\nu = C_1(h\nu - E_g)^{1/2} \quad (6.2)$$

When the material scatters in the diffuse manner K-M absorption coefficient S is constant. Using the re-emission function, obtained the following equation

$$[F(R_{\infty})h\nu]^2 = C_2(h\nu - E_g) \quad (6.3)$$

After obtaining $F(R_{\infty})$ and plotting $[F(R_{\infty})h\nu]^2$ against $h\nu$, the bandgap of the sample can be extracted.

Absorption spectra fitting procedure and Brus equation

In crystalline semiconductors, the absorption coefficient and incident photon energy were related by the equation

$$\alpha(\nu)h\nu = B(h\nu - E_{gap})^m \quad (6.4)$$

Where E_{gap} and B are the optical bandgap and constant respectively. $\alpha(\nu)$ is the absorption coefficient defined by Beer-Lamberts law.

$$\alpha(\nu) = 2.303 \times Abs(\lambda) / d \quad (6.5)$$

d is the thickness of the film. In ASF method, we can write equation (6.3) as a function of λ

$$\alpha(\lambda) = B(hc)^{m-1} \lambda \left(\frac{1}{\lambda} - \frac{1}{\lambda_g} \right)^m \quad (6.6)$$

Using Beer-Lamberts law, it is possible to re-write the above equation as

$$Abs(\lambda) = B_1(\lambda) \left(\frac{1}{\lambda} - \frac{1}{\lambda_g} \right)^m + B_2 \quad (6.7)$$

Where $B_1 = [B(hc)^{m-1} \times d / 2.303]$ and B_2 is a constant. Using this equation I have calculated the optical bandgap by ASF method without thickness. $E^{ASF} = 1238.7 / \lambda_g$

, the value of λ_g can be calculated by extrapolating the linear of a $\left(\frac{Abs(\lambda)}{\lambda} \right)^{1/m}$ Vs

$1/\lambda$ curve at $\left(\frac{Abs(\lambda)}{\lambda} \right)^{1/m} = 0$ is shown in fig. 6.21

Brus equation

A number of models are available to prove the relationship between particle size and bandgap of the materials [26-28]. Here effective mass model can also be used to calculate bandgap of the material [29]. Where the bandgap can be approximated by

$$E^* = E_g^{bulk} + \frac{\hbar^2 \pi^2}{2er^2} \left(\frac{1}{m_e m_0} + \frac{1}{m_h m_0} \right) - \frac{1.8e}{4\pi\epsilon\epsilon_0 r} \quad (6.8)$$

Where r is the radius of the particle, m_e and m_h are the effective masses of electron and hole respectively. ϵ is the relative permittivity and e is the electron charge. E_g^{bulk} is the bulk bandgap. Comparison of all the measured bandgap from different methods is shown in fig. 6.23 and correlation between bandgap and particle size are shown in fig. 6.24, bandgap values are tabulated in table 6.2.

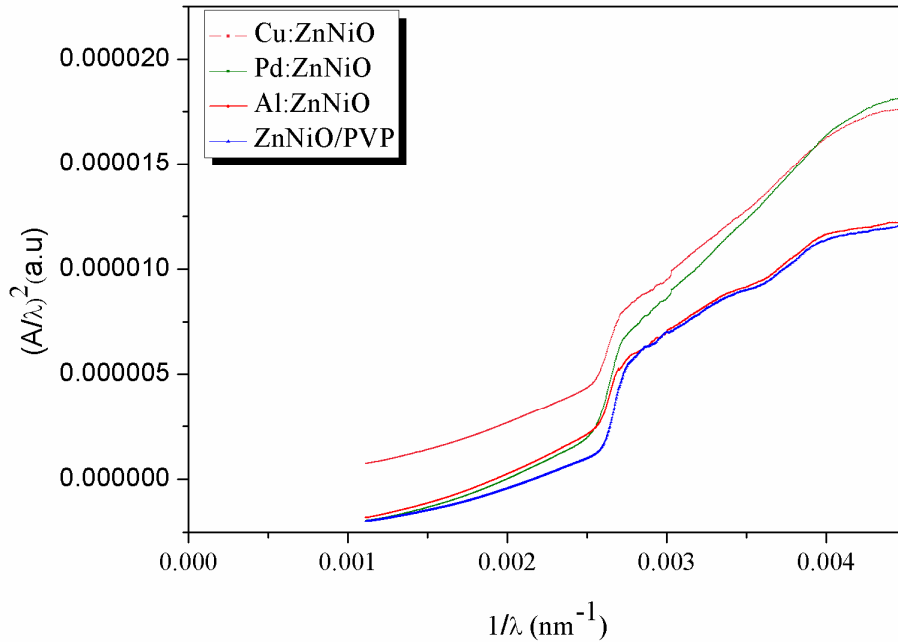


Figure 6.21: Absorption spectrum fitting plots of ZnNiO- PVP, Al:ZnNiO, Pd:ZnNiO and Cu:ZnNiO nanocomposites

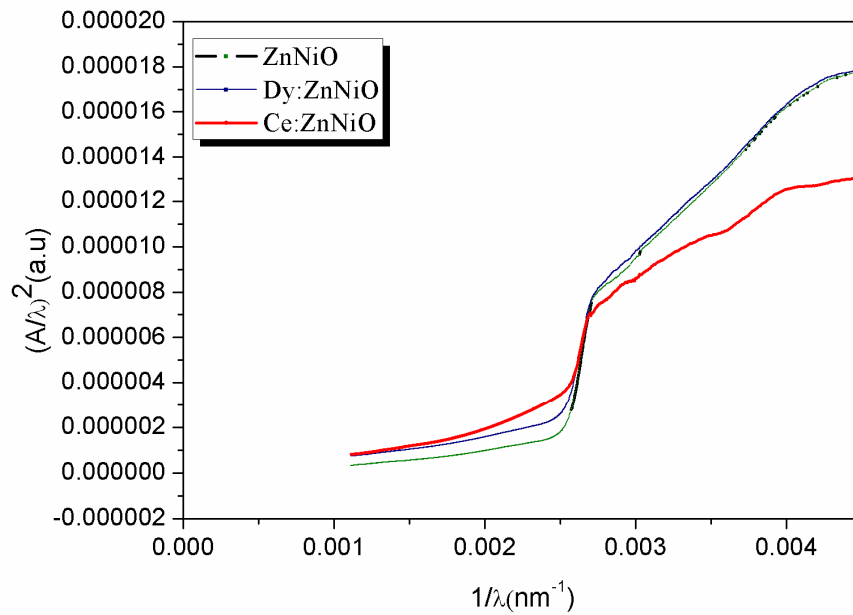


Figure 6.22: Absorption spectrum fitting plots of ZnNiO, Dy:ZnNiO, Ce:ZnNiO nanocomposites

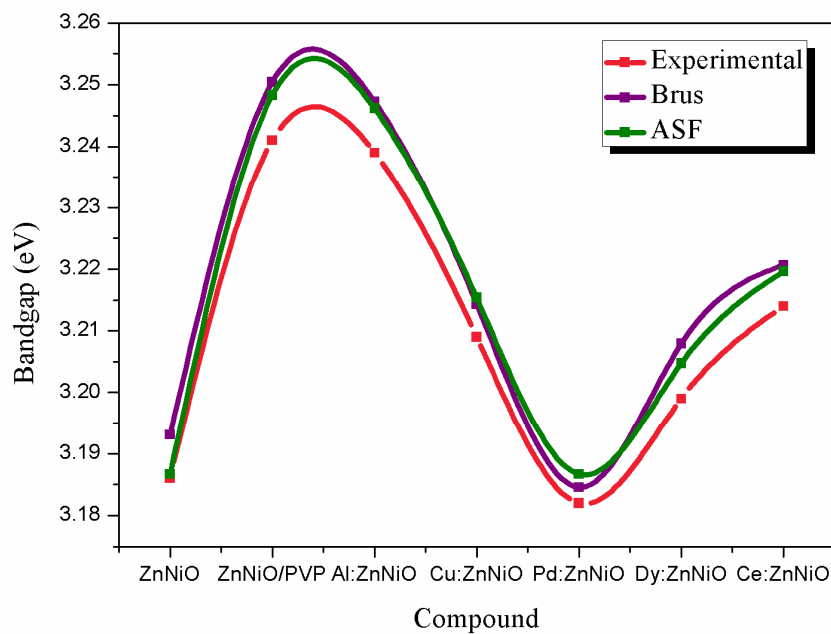


Figure 6.23: Comparison of bandgap determination from experimental, Brus and ASF methods

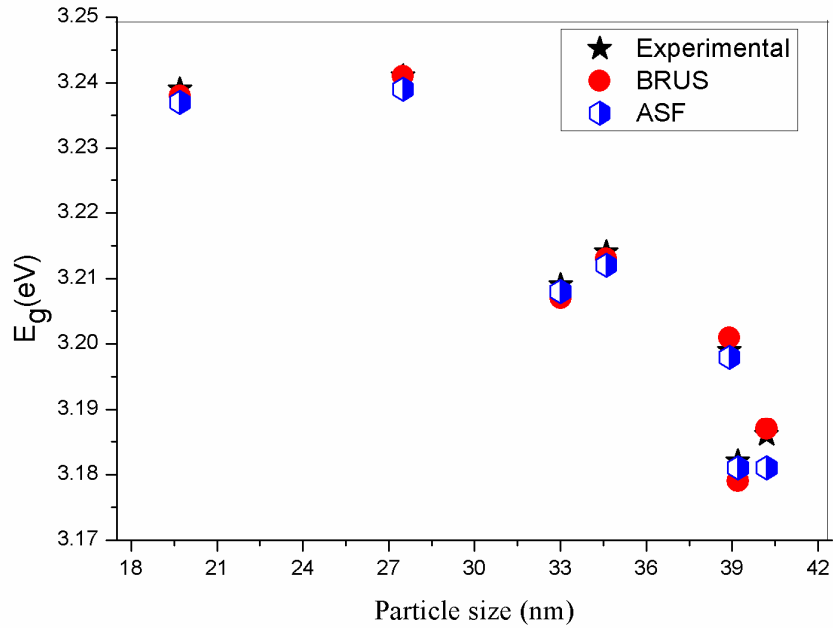


Figure 6.24: Correlation of bandgap with particle size of ZnNiO-PVP, Al:ZnNiO, Pd:ZnNiO, Cu:ZnNiO, Dy:ZnNiO and Ce:ZnNiO nanocomposites

Compound	Bandgap (eV) (± 0.01)		
	K-M plot	Brus	ASF
ZnNiO	3.186	3.187	3.181
ZnNiO/PVP	3.241	3.241	3.239
Al:ZnNiO	3.239	3.238	3.237
Cu:ZnNiO	3.209	3.207	3.208
Pd:ZnNiO	3.214	3.213	3.212
Dy:ZnNiO	3.199	3.201	3.198
Ce:ZnNiO	3.182	3.179	3.181

Table 6.3: Calculated bandgap from K-M plot, Brus equation, and ASF method.

6.5 Conclusion

Surface passivation effects on optical properties of nanocomposites were investigated by using diffuse reflectance spectra and fluorescence spectra. Bandgap calculated from absorption edge of the reflectance spectra shows that bandgap increasing is due to quantum confinement effect. This bandgap was also confirmed

by Kubelka-Munk function. Compared to pure ZnO, red shifted band edge was occurred in the case of all capped samples and this may be due to the electron-phonon coupling, lattice distortion and localized charge carriers. From these spectra, I have also calculated the defect energy named Urbach energy. Room temperature fluorescence spectra show multiple ultraviolet emissions and the near band edge emission extended to violet-blue region due to the overlapping of blue emission of PVP. Due to the surface passivation effect visible emission, mainly green emission is suppressed in capped ZnNiO, Al:ZnNiO, Cu:ZnNiO, Pd:ZnNiO, Dy:ZnNiO and Ce:ZnNiO nanocomposites. Oxygen vacancies are mainly located at the surface of the particle. Using fluorescence decay spectra I have calculated the fluorescence life time. Bandgap calculated from absorption spectra fitting, Brus equation and also from Kubelka-Munk function was almost equal. This property highlights surface passivation effects enhanced all the optical properties in capped nanocomposites compared to uncapped ZnNiO.

References

- [1] B. Djuricic, A. M. C. Ng, X. Y. Chen, *Prog. Quant. Elecron.* 34 (2010), 191.
- [2] L. Guo, L. Guo, S. Yang, C. Yang, P. Yu, J. Wang, W. Ge, G. K. L. Wong, *Appl. Phys. Lett.* 76 (2000) 2901.
- [3] A. B. Djuricic, Y. H. Leung, K. H. Tam, L. Ding, W. K. Ge, H. Y. Chen, S. Gwo, *Appl. Phys. Lett.* 88 (2006) 103107.
- [4] B. Zhang, X. T. Zhang, H. C. Gong, Z.S. Wu, S. M. Zhou, Z. L. Du, *Phys. Lett. A* 372 (2008) 2300.
- [5] Y. W. Heo, C. Abernathy, K. Pruessner, W. Sigmund, D. P. Norton, M. Overberg, F. Ren, M. F. Chisholm. *J. Appl. Phys.* **96**, 3424 (2004)
- [6] H. J. Ko, T. Yao, Y. Chen, S. K. Hong, *J. Appl. Phys.* 99 (2006) 093501.
- [7] S. H. Jeong, B. S. Kim, B. T. Lee, *Appl. Phys. Lett.* 82 (2003) 2625.
- [8] J. P. Ritchers, T. Voss, D. S. Kim, R. Scholz, M. Zacharias *Nanotechnology* 19 (2008) 305202.
- [9] C. H. Ahn, Y. Y. Kim, D. C. Kim, S. K. Mohanta, H. K. Chao, *J. Appl. Phys.* 105 (2009) 013502.
- [10] C. Jin, H. Kim, H. Y. Ryu, H. W. Kim, C. Lee, *J. Phys. Chem C*115 (2011) 8513.
- [11] C. L. Yang, J. N. Wang, W. K. Ge, L. Guo, S. H. Yang, D. Z. Shen, *J. Appl. Phys.* 90 (2001) 9.
- [12] L. Guo, S. Yang, C. Yang, P. Yu, J. Wang, W. Ge, G. K. L. Wong, *J. Appl. Phys.* 76 (2000) 20.
- [13] Y. He, J. A. Wang, W. Zhang, J. Song, C. Pei, X. Chen, *J. Nanosci Nanotechnol.* 11 (2010) 7254.
- [14] J. K. Leo, C. R. Tewell, R. K. Schulze, H. S. Jung, K. S. Hong, *Appl. Phys. Lett.* 86 (2005) 183.
- [15] N. S. Pesika, K. J. Stebe, P. C. Searson, *Adv. Mater.* 15 (2003) 15.
- [16] R. Elilarassi, G. Chandrasekaran, *J. Mater. Sci.: Mater. Electron.* 22 (2011) 751.
- [17] M. Choudhury, S.S. Nath, R.K. Nath, *Journal of Sensor Technology.* 1 (2011) 86.

- [18] S. C. Das, R. J. Green, J. Podder, T. Z. Regier, G. S. Chang, A. Moewes. *Phys. Chem. C* 2013, 117, 12745.
- [19] A. Popa, M. Lisa, V. Stancu, M. Bueda, E. Penito, and T. Botila, *J. Optoelectron. Adv. Mater*, 8 (2006) 43.
- [20] X. L. Wu, J. Y. Fan, T. Qiu, X. Yang, G. G. Siu, P. K. Chu, *Phys. Rev. Lett.*, 94 (2005) 026102.
- [21] F. Yakuphanoglu, S. Ilican, M. Caglar, Y. Caglar, *J. Opto. Electr. and Adv. Mater.* 9 (2010) 2180.
- [22] H. Lee, R. L. Webb, T. J. Johnson, W. Yang, P. C. Sercel, *Appl. Phys. Lett.* 73 (1998) 24.
- [23] J. Song, X. An, J. Zhou, Y. Liu, W. Wang, X. Li, W. Lan, E. Xie, *Appl. Phys. Lett.* 97 (2010) 122103.
- [24] C. W. Cheng, E. J. Sei, B. Liu, C. H. A. Huan, T. C. Sum, H. D. Sun, H. J. Fan, *Appl. Phys. Lett.* 96 (2010) 071107.
- [25] A. V. Dijken, E. A. Meulenkaamp, O. Vanmackelbergh, A. Meijerink, *J. Phys. Chem. B* 104 (2000) 1715.
- [26] A. L. Efors, M. Rosen, *Annu. Rev. Mater. Res.* 30 (2000) 475.
- [27] K. E. Anderson, C. Y. Fong, W. E. Pickett, *J. Non. Cryst. Solids* 229 (2000) 1105.
- [28] M. S. Hyberstsen, *Phy. Rev. Lett.* 72 (1994) 1514.
- [29] L. E. Brus, *J. Phys. Chem.* 90 (1986) 2555.

Chapter 7

Conclusions and Future work

At the beginning of this thesis, I have introduced the need for improving optical, magnetic and adsorption properties of semiconducting nanomaterials especially the ZnNiO nanocomposites. The study has resulted in the work has satisfying most of the targeted goals and there are still more gap for further work. Below the results of research work and their implications are summarized.

7.1 Conclusion

The aim of the study was to contribute to a deeper understanding on the surface modification effects on adsorption, magnetic and optical properties of ZnNiO, Al: ZnNiO, Cu: ZnNiO, Pd: ZnNiO, Dy: ZnNiO and Ce: ZnNiO nanocomposites, necessary for various applications. The importance of mesoporous nanocomposites are discussed in the introduction chapter. In the past decades, many ZnO nanostructures synthesizing from various routes showed that physical properties of all the products were changed from different methods. I have synthesized these nanocomposites using soft template method and investigated their structure, morphology, adsorption, magnetism, antibacterial activity, fluorescence emission and finally fluorescence lifetime.

Crystal structure and morphology of the nanocomposites were investigated by using X-ray diffractometer and scanning electron microscopy respectively. Surface passivation effects on crystal structure of (ZnNiO Al:ZnNiO, Cu:ZnNiO, Pd:ZnNiO, Dy:ZnNiO and Ce:ZnNiO) nanocomposites reveals that passivation by

polyvinyl pyrrolidone does not damage the hexagonal structure of ZnNiO. Grain size calculated from X-ray diffraction studies showed that, size decreases when ZnNiO capped with PVP and adjunction of other metals in ZnNiO lattice. Scanning electron microscopy (SEM) images of all the capped nanocomposites were confirmed the possibility of one dimensional growth of nanoparticles. The polymer, poly vinyl pyrrolidone can passivate the facets of ZnO and thereby adjust the growth velocity. Elemental Dispersive Spectra (EDS) of the nanocomposites confirmed the presence of constituent elements in the appropriate nanocomposites.

Capping effects on BET surface area, pore size, external area and pore volume of the nanocomposites were investigated through gas adsorption technique. These results gave us information that bandgap engineering is possible through nanoporosity. Special characteristics of large surface area and high porosity of mesoporous polymer capped ZnNiO and other five polymer capped nanocomposites have great potential applications in electronics, catalysts and optoelectronic devices. The specific surface areas of the uncapped and capped samples were determined by using a micrometrics ASAP 2020 surface area porosity analyzer. The calculated surface area of the capped samples are very high compared to uncapped samples and the N₂ adsorption isotherm hysteresis loop of the capped samples are matched to type IV H₃ hysteresis loop of mesoporosity. The pore size distribution of the samples were calculated from the data of the desorption branch of the isotherm using Barret-Joyner-Halenda (BJH) method. Microporosity of the samples is calculated from t-plot method. This result reveals that all the capped samples contain abundant mesoporous structured particles.

Magnetic observations show that ferromagnetism obtained in semiconductors does not only depend on the localized moments in magnetic ions. This ferromagnetism may also produce due to the defect generated magnetic moments. Some others proposed room temperature ferromagnetism to be associated with holes in the d shell due to charge transfer from the Zn atom at the surface to the capping molecule. Here I got room temperature ferromagnetism in all the PVP capped samples with high coercivity and magnetization. Uncapped ZnNiO showed paramagnetic behaviour with low retentivity.

Uncapped and capped metaloxide nanocomposites were explored as an antibacterial agent due to their non toxicity. In the research work, these composites were tested against *Pseudomonas aeruginosa* bacteria (Gram negative) using the disc diffusion method, to determine their ability as an antibacterial agent. The zone inhibition formed around each disc confirmed that Pd:ZnNiO and Dy:ZnNiO nanocomposite has the maximum activity among various capped metaloxides and uncapped ZnNiO has maximum activity than capped ZnNiO due to higher oxygen vacancies. After surface passivation this oxygen vacancies are decreased gradually and activity of the composites are decreased.

Surface passivation effects on diffuse reflectance spectra, fluorescence spectra and fluorescence life time and defect band energy formed inside the optical bandgap of the nanocomposites were investigated. This simple modification method through polymer capping provides a chance for improving fluorescence emission with high life time. Surface passivation helps to reach the main goal of the research work. Polyvinyl pyrrolidone capping improved fluorescence ultraviolet emission with suppressed visible emission. Fluorescence lifetime of the capped samples is increased when compared to uncapped ZnNiO nanocomposites. Bandgap calculated from diffuse reflectance spectra showed that bandgap is reduced in case of capped samples compared to pure ZnO and increased compared to uncapped ZnNiO. This increase in bandgap may be due to the quantum confinement effect in small size of the capped samples.

All the properties studied here, showed that these capped nanocomposites (ZnNiO, Al:ZnNiO, Cu:ZnNiO, Pd:ZnNiO, Dy:ZnNiO, and Ce:ZnNiO) are good materials for various applications especially in UV/Blue emitters and in transformer core applications. Due to its mesoporosity and non-toxicity it is focussing on the applications on drug delivery systems. This one dimensional, mesoporous, ferromagnetic, enhanced UV emitting properties of the nanocomposites confirmed surface passivation by polyvinyl pyrrolidone in metaloxide nanocomposites are a good way to increase all the physical properties.

7.2 Future work

As described above, we concluded that synthesizing methods are strongly influence on the properties of the nanomaterials. PVP as the capping agent prevent agglomeration and also it is a structure directing agent. Influence of PVP amount and molecular weight are the main factors affecting nucleation and growth. Our future work is decided to produce nanocomposites with controlled shape and enhanced physical properties while the amount of NaOH and the amount of all the metal nitrates are constant but the amount of PVP, volume of water and molecular weight of PVP are varying. The reaction temperatures are changed to modify the morphology and properties.